SEISMIC VELOCITY, RADIAL ANISOTROPY IN THE CRUST AND UPPER MANTLE OF NORTHEASTERN TIBETAN PLATEAU FROM SURFACE WAVE TOMOGRAPHY

A Dissertation Presented to

the Faculty of the Department of Earth and Atmospheric Sciences

University of Houston

In Partial Fulfillment

of the Requirements for the Degree

Doctor of Philosophy

By

Lun Li

December 2013

SEISMIC VELOCITY, RADIAL ANISOTROPY

IN THE CRUST AND UPPER MANTLE OF NORTHEASTERN

TIBETAN PLATEAU FROM SURFACE WAVE TOMOGRAPHY

Lun Li

APPROVED:

Dr. Aibing Li

Dr. Michael Murphy

Dr. Jolante Van Wijk

Dr. David Abt

Dean, College of Natural Sciences and Mathematics

ACKNOWLEDGEMENTS

My special thanks go to my advisor, Dr. Aibing Li, for her guidance, caring, and support throughout my PhD study and research. Dr. Li patiently introduced me into the fascinating world of seismology and guided me through all the difficulties in my research. Without her continuous support, I would not have been able to complete this dissertation.

My sincerest appreciation goes to Dr. Michael Murphy, Dr. Jolante Van Wijk, and Dr. David Abt for serving on my committee. I benefited from the discussions with them. Dr. Murphy helped me get familiar with the geology of the Tibetan plateau. I learned a lot from Dr. Van Wijk about geodynamic modeling, which broadened my knowledge and research interests. Suggestions from Dr. Abt greatly improved this dissertation. All their value suggestions and comments helped me finish this dissertation.

I also would like to thank Dr. Yang Shen at University of Rhode Island, Eric Sandvol at University of Missouri, Dr. Danian Shi at Institute of Mineral Resources of Chinese Academy of Geological Sciences (CAGS), Dr. Hongyi Li and Dr. Xinfu Li at China University of Geosciences (Beijing) for their great help and valuable suggestions during our research collaborations. In particular, I thank Dr. Hongyi Li and Dr. Xinfu Li for inviting me to give a talk at their department.

My appreciation also goes to Dr. Yonghua Li at Institute of Geophysics of China Earthquake Administration (CEA) and Dr. Yuanyuan Fu at Department for Earthquake Monitoring and Prediction of CEA. Dr. Yonghua Li gave me a lot of

suggestions regarding to the details of my research and Dr. Yuanyuan Fu shared with me many great suggestions in using two-plane-wave method. I also thank their hospitality when I visited their institutes.

I would like to extend my warmest gratitude to colleagues I met in the department of Earth and Atmospheric Sciences (EAS) at University of Houston: Ching-Wen Chen, Duo Yuan, Yao Yao, Xixi Wang, Olufemi Akanbi, and Jeff White. I also appreciate the friendship and help from many students: Luanxiao Zhao, Hemin Yuan, Hui Li, Ahmad Abir Ismail, Xuan Qin, and Xiaofan Hu. I also would like to thank Jincai Zhang, Zhongyi Hu, Zijian Zhang, and Brandon Gao from outside of EAS. All these people helped me in many different ways.

I also would like to thank the faculty members and staff in EAS, who gave me help in the past few years. The lectures given by many faculty members broaden my knowledge. Special thanks to Evgeny Chesnokov, Stuart Hall, Guoquan Wang, Christopher Liner, and John Castagna. Jay Krishnan helped me solve many hardware and software problems. Sylvia Marshall provided me with a lot of help. I heartily thank those great people in the department for their important contributions.

I also would like to thank EAS, Society of Petrophysicists and Well Log Analysts (SPWLA), and Shreveport Geological Society (SGS) for the scholarships. The research in this dissertation is supported by NSF grant EAR-0738879.

Finally, my deepest gratitude goes to my wife, my parents, my parents-in-law, and my brother. Without their understanding, love, and support, it would have been impossible for me to finish this dissertation work.

SEISMIC VELOCITY, RADIAL ANISOTROPY

IN THE CRUST AND UPPER MANTLE OF NORTHEASTERN

TIBETAN PLATEAU FROM SURFACE WAVE TOMOGRAPHY

An Abstract of a Dissertation

Presented to

the Faculty of the Department of Earth and Atmospheric Sciences

University of Houston

In Partial Fulfillment

of the Requirements for the Degree

Doctor of Philosophy

By

Lun Li

December 2013

ABSTRACT

The northeastern (NE) Tibetan Plateau with complex interaction between mountain building and strike-slip faulting is a prime site to study the growth of the plateau and to understand the dynamic processes at its boundaries. This dissertation research investigates the crust and upper mantle structure in the NE Tibetan Plateau using surface wave tomography from teleseismic data recorded at the 36 seismic stations of NorthEast Tibet Seismic (NETS) array.

The first part of this dissertation is to construct a 3-D SV velocity (V_{SV}) model using Rayleigh wave data. The average and 2-D variations of phase velocities were obtained at 14 periods from 20 to 100 s and then used to constrain 1-D and 3-D V_{SV} models. The entire region is characterized by relatively low absolute velocity, indicating a weak upper mantle. One pronounced slow anomaly centered at ~120 km depth is imaged right beneath a restraining bend of the Kunlun fault and is probably caused by anomalously high temperature and partial melting resulted from localized asthenosphere upwelling after the delamination of a thick lithosphere root beneath the bend.

In the second part of the dissertation, a 3-D SH velocity (V_{SH}) model was obtained from the Love wave phase velocities at 13 periods from 20 to 91 s, and then used to construct a 3-D radial anisotropic model combined with the V_{SV} model. The lower crust is characterized with positive anisotropy ($V_{SH}>V_{SV}$). The large positive anisotropy can be explained by horizontal alignment of anisotropic minerals such as mica at the formation of lower crust. The mantle lithosphere above 90 km is largely isotropic while weak positive anisotropy appears beneath 90 km, which probably

marks the lithosphere-asthenosphere boundary. The Kunlun restraining bend and its surrounding region are distinguished by relatively negative radial anisotropy in the entire lithosphere, providing evidence for coherent lithosphere deformation in this area where local compression stress is high. Such coherent lithosphere deformation is not observed in the eastern portion of the Kunlun neither in the Qinling-Qilian orogen, suggesting that the lithosphere shortening in most of the NE Tibet is not as strong as in the interiors of the plateau.

CONTENTS

LIST OF FIGURES

Chapter 1. Introduction

1.1. The Tibetan Plateau

The Tibetan Plateau is the largest active orogenic belt on the earth and has been a prime site to investigate continental deformation, kinematics and dynamics, the processes of mountain building, and the interaction between tectonics and climate change. The Tibetan Plateau is composed of a set of continental blocks (or terranes) of different origin, including the Lhasa Terrane, Qiangtang Terrane, and Songpan-Ganzi Terrane from south to north, respectively (Figure 1.1) [*Dewey et al*., 1988]. These terranes were accreted successively to the Eurasian Plate during the Paleozoic and Mesozoic eras and are currently separated by a series of suture zones [*Allegre et al.*, 1984; *Dewey et al*., 1988; *Yin and Harrison*, 2000], such as the Indus-Zangbo Suture (IZS), Bangong-Nujiang Suture (JNS), and Jinsha Suture (JS) (Figure 1.1 and Figure 1.2a). The plateau is bounded by a series of mountain ranges, the Karakorum mountain range to the west, the Himalayan mountain range to the south, and the Kunlun and the Qilian mountain range to the north. In addition, the plateau is bounded by several continental blocks that undergo little present-day deformation. They include the Tarim block to the northwest, the Gobi-Alashan Platform and Sino-Korean craton (Ordos) to the north and northeast, and the Yangtze craton (Sichuan Basin) to the east (Figure 1.1). These continental blocks are generally bounded by major thrust or strike-slip faults, and play a significant role in describing the evolution of the Tibetan Plateau [e.g., *Peltzer and Tapponnier*, 1988; *Harrison et al.*, 1992; *Clark and Royden*, 2000].

The Cenozoic tectonic evolution and growth of the Tibetan Plateau are mainly controlled by the convergence of the Indian Plate with Eurasia [*Argand*, 1924]. The continent-continent collision of the Indian and Eurasian Plates that began ~50 Ma ago [*Molnar et al.*, 1973; *Molnar and Tapponnier*, 1975; *Patriat and Achache*, 1984; *Molnar and Stock*, 2009] has resulted in ~2000 km shortening and large scale uplift of the Tibetan Plateau [*Dewey, 1989*] and in some degree has contributed to deformation of its adjacent regions such as eastern China [*Bendick and Flesch*, 2007; *Peltzer and Tapponnier*, 1988; *Tapponnier and Molnar*, 1977]. Over the past decades, a wide range of geologic and geophysical studies have been conducted within the Tibetan Plateau with the primary objectives of understanding the continental collision process, the incorporation of crustal and mantle material from the Indian Plate into the Eurasian Plate. However, understanding the processes that have formed the plateau also requires the knowledge of the geology and dynamic processes acting along other boundaries of the plateau.

Several competing models have been proposed to explain the growth and uplift of the Tibetan Plateau. The most popular competing models include (1) the under-thrusting model, (2) the stepwise-rise model, (3) the crustal flow model, and (4) the lithosphere delamination model. The under-thrusting model is the earliest model proposed by *Argand* [1924] to explain the uplift of the Tibetan Plateau. Investigations using global tomography [*Zhou and murphy*, 2005] and receiver functions [*Tilmann et al*., 2003] suggest that the Indian lithosphere underthrusts the entire Tibetan Plateau (Figure 1.2). The under-thrusting model was further modified by the stepwise-rise model (i.e., rigid block model/intracontinental subduction model) [*Tapponier et al*.,

2001], which suggests that the Eurasian lithospheric block subducts under Tibet sequentially along major strike-slip faults from north to south (Figure 1.3) [*Kosarev et al*., 1999; *Kind et al*., 2002; *Yin and Harrison*, 2000]. In this scenario, the strike-slip faults are considered as lithospheric faults and previous investigations demonstrated that this model [e.g., *Kosarev et al*., 1999; *Kind et al*., 2002; *Yin and Harrison*, 2000] has been able to account for the large-scale features of the deformation of the Tibetan Plateau (e.g., crustal thickening, eastward extrusion), especially for the southern part of the plateau, but have failed to explain the formation and growth of mountain ranges in the east and north of the plateau which are undergoing no or little present surface deformation. Therefore, the crustal flow model was proposed to associate crustal thickening and deformation, and eastward displacement of crustal material with viscous flow in those regions with little present surface deformation (Figure 1.4) [*England and Houseman*, 1989; *Houseman and England*, 1993; *England and Molnar*, 1997; *Royden*, 1996; *Royden et al.*, 1997; *Clark and Royden*, 2000; *Clark et al.*, 2005]. Much of geophysical evidence from seismic tomography, magnetotellurics (MT), receiver function and shear wave splitting studies [e.g., *Brown et al*., 1996; *Chen et al*., 1996; *Kind et al.*, 1996; *Wei et al.*, 2001; *Royden*, 1996; *Royden et al*., 1997; *Clark and Royden*, 2000; *Sherrington et al.*, 2004] was in support that the viscous flow exists in the middle to lower crust in central, southern, and northern Tibet. Alternatively, previous studies suggested lithosphere root in the Himalaya and the southern Tibetan Plateau peeled off and sank into the asthenosphere (Figure 1.5) [*Molnar et al.*, 1993; *Jiménez-Munt and Platt*, 2006; *Jiménez-Munt et al.*, 2008]. Here I refer to it as the delamination model. In addition,

the rapid rise of Qilian mountain range [e.g., *Métivier et al.*, 1998] and Liupan mountain range around 5.3 Ma is suggested as a consequence of this lithosphere removal [*Molnar*, 2005, *Zhang et al.*, 2013]. However, it is still unclear whether the lithosphere root is removed in the northeastern (NE) Tibetan Plateau and whether this removal is in a localized scale or in a regional scale.

The best place to address the interaction between the Tibetan Plateau and adjacent terranes, and to test the competing models is the northeastern (NE) Tibetan Plateau, which is an area defined by the Haiyuan fault system in the north, the Ordos block in the east, the Kunlun fault system in the south, and the Altyn Tagh fault system in the west (Figure 1.1). The NE Tibetan Plateau is still rising with a horizontal shortening rate of 13 mm/year in NE-SW direction [*e.g., Van der Woerd et al.*, 1998]. Thus, this actively growing part of the plateau may provide evidence for mechanisms that probably once operated in southern and central Tibet. Receiver-function studies support the interpretation that the NE Tibetan Plateau formed by the stepwise-rise model, which emphasizes that most deformation of the continent is localized on major block bounding faults, such as the Kunlun strike-slip fault. However, a recent seismic refraction study suggests that actively deforming middle NE Tibetan crust is dominated by discrete sub-horizontal simple-shear zones that decouple the deformation in the crust from that in the mantle. Alternatively, *Zhang et al.* [2011] showed a low velocity asthenospheric channel beneath the Qilian-Qinling Orogen that lies between the Ordos and Sichuan blocks from Rayleigh wave tomography, implying the presence of east directed asthenospheric flow.

Despite decades of study on these competing models, questions remain regarding which model best explains the uplift of the NE Tibetan Plateau. For example, what cause the rise of the NE Tibetan Plateau? Is it the mid-crustal flow, the coherent thickening of the Tibet lithosphere, or the subduction of the Eurasian blocks? Whether or not the lithosphere root is removed in the NE Tibetan Plateau and whether upwelling asthenosphere flow exists? Could the Kunlun strike-slip fault be a lithospheric fault and facilitate eastward extrusion of the Tibetan Plateau? Given the complex lithosphere deformation patterns in the NE Tibetan Plateau, high-resolution shear wave velocity and radial anisotropy models in the crust and upper mantle would help to distinguish these competing models and provide useful constraints on understanding lithosphere dynamics in the NE Tibetan Plateau.

1.2. Surface Wave Tomography

A surface wave is a type of wave propagating along a great-circle path at the surface of the Earth. Surface waves at different periods are sensitive to shear-wave structure at different depths; therefore, they can provide critical depth constraints on the velocity variation. Additionally, compared to body wave tomography, suface wave tomography benefits from high vertical resolution and can be used to derive absolute shear wave velocity values. In this dissertation, I applied the two-plane-wave (TPW) method to obtain surface wave phase (Rayleigh wave and Love wave) velocity and then solve for shear wave velocity (Chapter 2) and radial anisotropy (Chapter 3) models in the NE Tibetan Plateau .

Traditional surface-wave-phase-velocity measurements using single-station method and two-station method require accurate source information or assume great-circle ray paths [e.g., *Montagner,* 1985]. This would limit the number of ray path and hence lower the lateral resolution. Additionally, the assumption of great-circle ray path may fail to accout for the focusing or defocusing of energy, multipathing, and scattering due to lateral heterogeneities [e.g., *Friederich et al.,* 1994]. If the incoming surface wave is assumed as a plane wave, non-planar energy would induce the inaccuracies in phase velocity determinations, especially for the periods of less than 50 s [*Wielandt,* 1993]. Two-plane wave method can overcome these inaccuracies by taking account for non-planar energy in the incoming wavefield caused by scattering or multipathing outside of the study region and provide a powerful approach to measure the phase velocity map crossing a seismic array. The incoming wavefield is represented by two plane waves with unknown amplitudes, phases, and propagation directions, which are solved together with phase velocities in the inversion (Figure 1.6). The two-plane-wave inversion method was described in detail by *Forsyth and Li* [2005].

Over the past decade, high lateral resolution Rayleigh wave phase velocities and shear wave models in the upper mantel have been determined in many places using the two-plane-wave inversion technique [e.g., *Li et al.,* 2003; *Weeraratne et al.,* 2003; *Forsyth and Li*, 2005; *Li and Detrick*, 2006; *Fu et al.,* 2010; *Chen and Li*, 2012; *Zhang et al*., 2011]. This method was designed for better resolving Rayleigh wave phase velocity within a seismic network [*Forsyth and Li*, 2005]. Model resolution from this method has been further improved to a scale of ~100 km by adopting 2-D,

Born approximation sensitivity kernels [*Yang and Forsyth*, 2006]. However, this TPW method has not been applied to Love waves. In this dissertation, I applied the TPW method to Love wave. In the Rayleigh wave inversion, only the vertical components are used and the amplitudes of the two plane waves can be added directly. For Love waves, their particle motions for the two plane waves are not aligned in the same direction; therefore, they have to be decomposed to two orthogonal components first. Then simple addition can be performed to the same component of the two plane waves. The rest of the inversion is similar as for Rayleigh waves. More discussions about surface wave data and method are given in chapter 2 and chapter 3.

1.3. Seismic Anisotropy

Seismic anisotropy has been detected in the crust and upper mantle in many regions. It reflects deformation in the lithosphere and mantle flows in the asthenosphere and provides constraints on dynamic processes of the Earth. Seismic anisotropy has been suggested to be due to either crystallographic or lattice preferred orientation (CPO, LPO) [e.g., *Montagner*, 1998], or shape preferred orientation (SPO) of material with distinct isotropic elastic properties [e.g., *Silver and Chan*, 1991].

There are two main types of seismic anisotropy, azimuthal anisotropy and radial anisotropy. Azimuthal anisotropy can be detected by shear-wave splitting method and surface wave tomography. Shear wave splitting measurements from SKS or other core refracted shear waves can have high lateral resolution but little constraints on the depths of anisotropic sources. Surface waves at different periods are sensitive to the Earth at different depths, and azimuthal anisotropy variation with periods indicates

the change of anisotropy structure with depth [*Nishimura and Forsyth*, 1989; *Li and Detrick,* 2003].

Radial anisotropy is associated with a transversely isotropic medium with a vertical symmetry axis, in which wave speed depends on its polarization and direction of propagation. Radial anisotropy has been observed in 1-D [*Dziewoński and Anderson*, 1981] and 3-D global scale [e.g., *Ekstrom and Dziewonski*, 1998]. The transversely isotropic medium can be illustrated by five independent elastic parameters represented as *A*, *C*, *N*, *L* and *F*, which are a function of velocity represented as [e.g., *Takeuchi and Saito*, 1972; *Dziewoński and Anderson*, 1981]

$A = \rho V_{PH}^2,\ C = \rho V_{PV}^2,\ N = \rho V_{SH}^2,\ \textit{and}\ \ L = \rho V_{SV}^2,$

with

$$\xi = \left(\frac{V_{SH}}{V_{SV}}\right)^2 = \frac{N}{L}, \qquad \phi = \left(\frac{V_{PV}}{V_{PH}}\right)^2 = \frac{N}{L}, \text{ and } \eta = \frac{F}{A-2L},$$

in which the ξ and ϕ represent shear and the compressional wave anisotropy, respectively. The ellipticity, η, determines the shape of the transition between V_{SH} and V_{SV} as a function of dip from horizon [*Anderson*, 1965].

In this dissertation, I solved shear wave velocity and radial anisotropic parameters from discrepancy between Rayleigh wave and Love wave dispersions. Rayleigh wave is sensitive to V_{SV}, while Love wave is sensitive to V_{SH}. The Rayleigh-Love discrepancy means that an isotropic shear velocity model fails to fit the Rayleigh wave and Love wave dispersive curves simultaneously, and requires the existence of radial anisotropy. In this study, radial anisotropy is defined as the percentage difference between V_{SH} and V_{SV} in the medium: $\gamma = (V_{SH}-V_{SV})/V_S$. Vs is the isotropic or effective shear wave velocity and is computed from V_{SH} and V_{SV} via a

Voigt average, $V_S = \sqrt{(2V_{SV}^2 + V_{SH}^2)/3}$ [*Babuška and Cara*, 1991]. The new shear wave velocity model is better than that from Rayleigh wave data alone because the latter might be biased by anisotropy. For example, low velocity layer in the shear wave model from Rayleigh wave constraints could be a result of Vsh>Vsv, indicating horizontal flow or alignment of materials. In contrast, Vsv>Vsh that indicates vertical flow or alignment of material can be traded off with high shear wave velocity in Rayleigh wave tomography. The 3-D isotropic shear wave and radial anisotropic models provide new constraints on the structure and deformation of the crust and upper mantle, and help to distinguish competing models.

Several important questions can be addressed from the 3-D anisotropic model. For example, (1) the channel flow model is supported if low velocity and Vsh>Vsv are observed in the middle to lower crust. This will imply the decoupling of deformation between the upper crust and lithospheric mantle; (2) The removal of the Asian lithosphere due to thickening or subduction might be evident if low velocity and Vsv>Vsh are present in the shallow upper mantle; (3) Strong horizontal shear and low velocity are expected near the Kunlun strike-slip fault, which will be reflected as low velocity and Vsh>Vsv. The vertical distribution of these properties at the fault helps to determine if the Kunlun fault cuts the entire lithosphere.

1.4. References

Allegre, C. O., Courtillot, V., Tapponnier, P., Hirn, A., Mattauer, M., Coulon, C., ... & Xu, R. (1984), Structure and evolution of the Himalaya–Tibet orogenic belt, *Nature* 307, 17-22.

Anderson, D. L. (1965), Recent evidence concerning the structure and composition of the earth's mantle. *Physics and Chemistry of the Earth*, *6*, 1-131.

Argand, E., (1924), La tectonique de l'Asie: International Geological Congress, 13th, Proceedings, v. 7, p. 171–372

Babuška, V., & Cara, M. (1991), *Seismic anisotropy in the Earth* (Vol. 10). Springer.

Bendick, R., & Flesch, L. (2007), Reconciling lithospheric deformation and lower crustal flow beneath central Tibet. *Geology*, *35*(10), 895-898.

Brown, L. D., W. Zhao, K. D. Nelson, M. Hauck, D. Alsdorf, A. Ross, M. Cogan, M. Clark, Xianwen Liu, and J. Che(1996), Bright Spots, Structure and Magmatism in Southern Tibet from INDEPTH Seismic Reflection Profiling, *Science*, 274, 1688-1690.

Chen, C. and A. Li (2012), Shear wave structure in the Grenville Province beneath the lower Great Lakes region from Rayleigh wave tomography, *J. Geophys. Res.*, 117, doi:10.1029/2011JB008536

Chen, L., Booker, J.R., Jones, A.G., Wu, N., Unsworth, M.J., Wei, W., and Tan, H. (1996), Electrically conductive crust in southern Tibet from INDEPTH magnetotelluric surveying. *Science* 274, 1694–1696.

Clark, M., and Royden, L. (2000), Topographic ooze: building the eastern margin of Tibet by lower crustal flow. *Geology*, 28, 703–706.

Clark, M., Bush, J., and Royden, L. (2005), Dynamic topography produced by lower crustal flow against rheological strength heterogeneities bordering the Tibetan Plateau, *Geophys. J. Int.*, 162, 575–590.

Dewey, J. F., Helman, M. L., Knott, S. D., Turco, E., & Hutton, D. H. W. (1989), Kinematics of the western Mediterranean. *Geological Society, London, Special Publications*, *45*(1), 265-283.

Dewey, J. F., Shackleton, R. M., Chengfa, C., and Yiyin, S. (1988), The tectonic evolution of the Tibetan Plateau. *Philosophical Transactions of the Royal Society of London. Series A, Mathematical and Physical Sciences*, *327*(1594), 379-413.

Dziewonski, A. M., & Anderson, D. L. (1981), Preliminary reference Earth model. *Physics of the earth and planetary interiors*, *25*(4), 297-356.

Ekström, G., & Dziewonski, A. M. (1998), The unique anisotropy of the Pacific upper mantle. *Nature*, *394* (6689), 168-172.

England, P. C., and G. A. Houseman (1989), Extension during continental convergence, with application to the Tibetan Plateau, *J. Geophys. Res.*, 94, 17,561 –17,579.

England, P. C., and P. Molnar (1997), Active deformation of Asia: From kinematics to dynamics, *Science*, 278, 647 – 650.

Forsyth, D. W., and A. Li (2005), Array-analysis of two-dimensional variations in surface wave phase velocity and azimuthal anisotropy in the presence of multipathing interference., in Seismic Earth: Array Analysis of Broadband Seismograms, *Geophys Monogr. Ser.*, vol. 187, edited by A. Levander and G. Nolet, pp. 81–97, AGU,

Friederich, W., E. Wielandt, and S. Stange (1994), Non-plane geometries of seismic surface wavefields and their implications for regional surface-wave tomography, *Geophys. J. Int.*, 119, 931– 948.

Fu, Y. V., A. Li, and Y. J. Chen (2010), Crustal and upper mantle structure of southeast Tibet from Rayleigh wave tomography, *J. Geophys. Res.*, 115, B12323, doi:10.1029/2009JB007160.

Harrison, T. M., Copeland, P., Kidd, W. S. F., & Yin, A. (1992), Raising tibet. *Science*, *255*(5052), 1663-1670.

Houseman, G. and England, P. (1993), Crustal thickening versus lateral expulsion in the Indian–Asian continental collision, *J. Geophys. Res.*, 98(B7), 12 233–12 249.

Jiménez-Munt, I., & Platt, J. P. (2006), Influence of mantle dynamics on the topographic evolution of the Tibetan Plateau: Results from numerical modeling. *Tectonics*, *25*(6).

Jiménez-Munt, I., Fernàndez, M., Vergés, J., & Platt, J. P. (2008), Lithosphere structure underneath the Tibetan Plateau inferred from elevation, gravity and geoid anomalies. *Earth and Planetary Science Letters*, *267*(1), 276-289.

Kind, R., et al. (1996), Evidence from earthquake data for a partially molten crustal layer in southern Tibet, *Science*, 274, 1692-1694.

Kind, R., Yuan, X., Saul, J., Nelson, D., Sobolev, S. V., Mechie, J., ... & Jiang, M. (2002), Seismic images of crust and upper mantle beneath Tibet: Evidence for Eurasian plate subduction. *Science*, *298*(5596), 1219-1221.

Kosarev, G., Kind, R., Sobolev, S. V., Yuan, X., Hanka, W., & Oreshin, S. (1999), Seismic evidence for a detached Indian lithospheric mantle beneath Tibet. *Science, 283*(5406), 1306-1309.

Li, A. and R.S. Detrick (2006), Seismic structure of Iceland from Rayleigh wave inversions and geodynamic implications, *Earth Planet. Sci. Lett.*, Vol 241, 901-912.

Li, A., Forsyth, D.W., Fischer, K.M. (2003), Shear velocity structure and azimuthal anisotropy beneath eastern North America from Rayleigh wave inversion. *J. Geophys. Res.*, 108 (B8), 2362. doi:10.1029/2002JB002259.

Métivier, F., Gaudemer, Y., Tapponnier, P., & Meyer, B. (1998), Northeastward growth of the Tibet plateau deduced from balanced reconstruction of two depositional areas: The Qaidam and Hexi Corridor basins, China. *Tectonics*, *17*(6), 823-842.

Molnar, P. (2005), Mio-Pliocene growth of the Tibetan Plateau and evolution of East Asian climate. *Palaeontologia Electronica*, *8*(1), 1-23.

Molnar, P., and J. M. Stock (2009), Slowing of India's convergence with Eurasia since 20 Ma and its implications for Tibetan mantle dynamics, *Tectonics*, 28, TC3001, doi:10.1029/2008TC002271.

Molnar, P., and Tapponnier, P. (1975), Cenozoic tectonics of Asia: effects of a continental collision. *Science*, 189, 419–426.

Molnar, P., England, P., & Martinod, J. (1993), Mantle dynamics, uplift of the Tibetan Plateau, and the Indian monsoon. *Reviews of Geophysics*, *31*(4), 357-396.

Molnar, P., Fitch, T. J. & Wu, F. T. (1973), Fault plane solutions of shallow earthquakes and contemporary tectonics in Asia. *Earth Planet. Sci. Lett.*, 19, 101–112.

Montagner, J. P. (1985), Seismic anisotropy of the Pacific Ocean inferred from long-period surface waves dispersion. *Physics of the earth and planetary interiors*, 38 (1), 28-50.

Montagner, J. P. (1998), Where can seismic anisotropy be detected in the Earth's mantle? In boundary layers…. In *Geodynamics of Lithosphere & Earth's Mantle* (pp. 223-256). Birkhäuser Basel.

Nishimura, C. E., & Forsyth, D. W. (1989), The anisotropic structure of the upper mantle in the Pacific. *Geophysical Journal International*, *96*(2), 203-229.

Patriat, P., and J. Achache (1984), India-Eurasia collision chronology has implications for crustal shortening and driving mechanism of plates, *Nature*, 311, 615 – 621.

Peltzer, G., & Tapponnier, P. (1988), Formation and evolution of strike-slip faults, rifts, and basins during the India-Asia collision: An experimental approach. *Journal of Geophysical Research: Solid Earth (1978–2012)*, *93*(B12), 15085-15117.

Royden, L.H. (1996), Coupling and decoupling of crust and mantle in convergent orogens: implications for strain partitioning in the crust, *J. Geophys. Res.*, 101, 17 679–17 705.

Royden, L.H., Burchfiel, B.C., King, R.W., Wang, E., Chen, Z.L., Shen, F. & Liu, Y.P. (1997), Surface deformation and lower crustal flow in eastern Tibet, *Science*, 276, 788–790.

Sherrington, H. F., Zandt, G., & Frederiksen, A. (2004), Crustal fabric in the Tibetan Plateau based on waveform inversions for seismic anisotropy parameters. *Journal of Geophysical Research*, *109*(B2), B02312.

Silver, P. G., & Chan, W. W. (1991), Shear wave splitting and subcontinental mantle deformation. *Journal of Geophysical Research: Solid Earth (1978–2012)*,*96*(B10), 16429-16454.

Takeuchi, H., & Saito, M. (1972), Seismic surface waves. *Methods in computational physics*, *11*, 217-295.

Tapponnier, P., & Molnar, P. (1977), Active faulting and tectonics in China. *Journal of Geophysical Research*, *82*(20), 2905-2930.

Tapponnier, P., Xu, Z., Roger, F., Meyer, B., Arnaud, N., Wittlinger, G., et al. (2001), Oblique stepwise rise and growth of the Tibet Plateau. *Science*, 294, 1671–1677.

Tilmann, F., Ni, J., & INDEPTH III, S. T. (2003), Seismic imaging of the downwelling Indian lithosphere beneath central Tibet. *Science*, *300*(5624), 1424-1427.

Van Der Woerd, J., Ryerson, F. J., Tapponnier, P., Gaudemer, Y., Finkel, R., Mériaux, A. S., ... & Qunlu, H. (1998), Holocene left-slip rate determined by cosmogenic surface dating on the Xidatan segment of the Kunlun fault (Qinghai, China). *Geology*, *26*(8), 695-698.

Weeraratne, D. S., Forsyth, D. W., Fischer, K. M., & Nyblade, A. A. (2003), Evidence for an upper mantle plume beneath the Tanzanian craton from Rayleigh wave tomography. *Journal of Geophysical Research*, *108*(B9), 2427.

Wei, W. B., et al. (2001), Detection of widespread fluids in the Tibetan crust by magnetotelluric studies, *Science*, 292, 716–719, doi:10.1126/science.1010580.

Wielandt, E., 1993, Propagation and structural interpretation of non-plane waves, *Geophys. J. Int.*, 113, 45–53.

Yang, Y., and Forsyth, D. (2006), Regional tomographic inversion of the amplitude and phase of Rayleigh waves with 2-D sensitivity kernels. *Geophys. J. Int.*, 166, 1148-1160.

Yin, A., & Harrison, T. M. (2000), Geologic evolution of the Himalayan-Tibetan orogen. *Annual Review of Earth and Planetary Sciences*, *28*(1), 211-280.

Zhang, H., Teng, J., Tian, X., Zhang, Z., Gao, R., & Liu, J. (2013), Lithospheric thickness and upper-mantle deformation beneath the NE Tibetan Plateau inferred from S receiver functions and SKS splitting measurements. *Geophysical Journal International*, *191*(3), 1285-1294.

Zhang, Q., E. Sandvol, J. Ni, Y. Yang, and Y. J. Chen (2011), Rayleigh wave tomography of the northeastern margin of the Tibetan Plateau, *Earth Planet. Sci. Lett.*, 304, 103–112, doi:10.1016/j.epsl.2011.01.021.Zhou, H. W., & Murphy, M. A. (2005). Tomographic evidence for wholesale under-thrusting of India beneath the entire Tibetan plateau. *Journal of Asian Earth Sciences*, *25*(3), 445-457.

Zhou, Y., Murphy, M. A., Hamade, A., (2006), Structural development of the Peregrina-Huizachal anticlinorium, Mexico. *Journal of Structural Geology*, v. 28, p. 494-507.

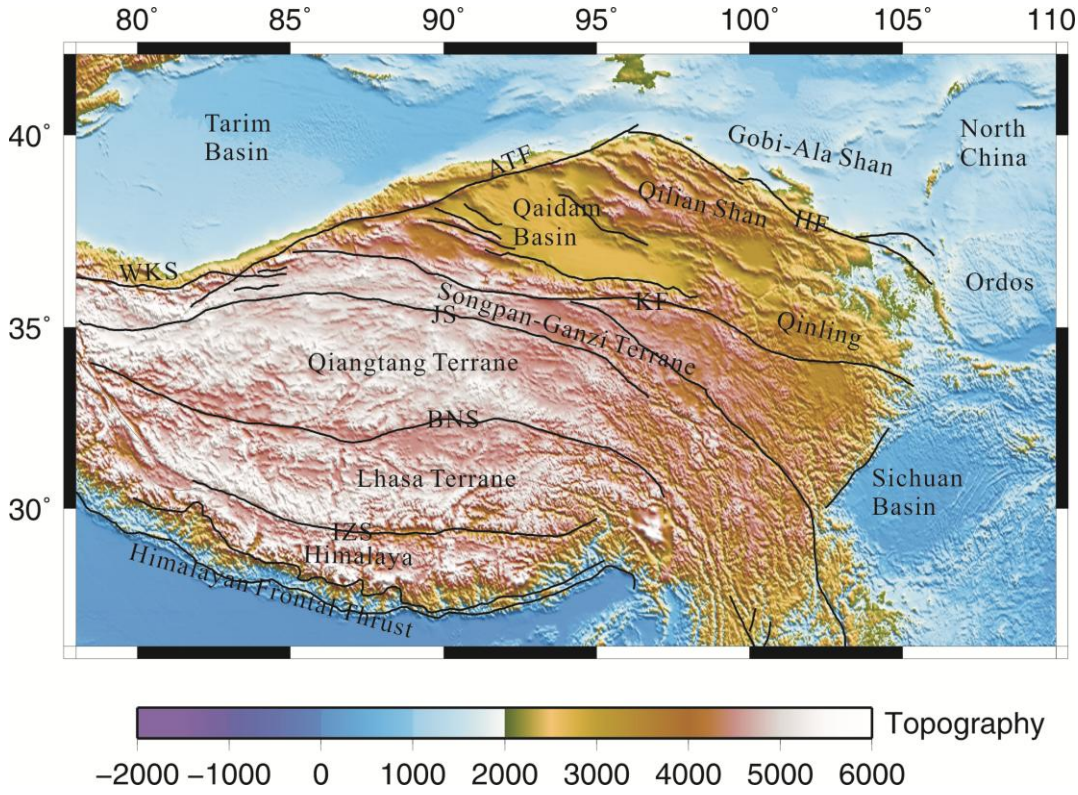

Figure 1.1 Topography map of the Tibetan Plateau and surrounding regions. Black lines represent the faults. ATF, Altyn tagh fault. KF, Kunlun fault; HF, Haiyuan fault; KLM, Kunlun Mountains; WKS, West Kunlun Shan; IZS, Indus-Zangbo Suture; BNS, Bangong-Nujiang Suture; JS, Jinsha Suture.

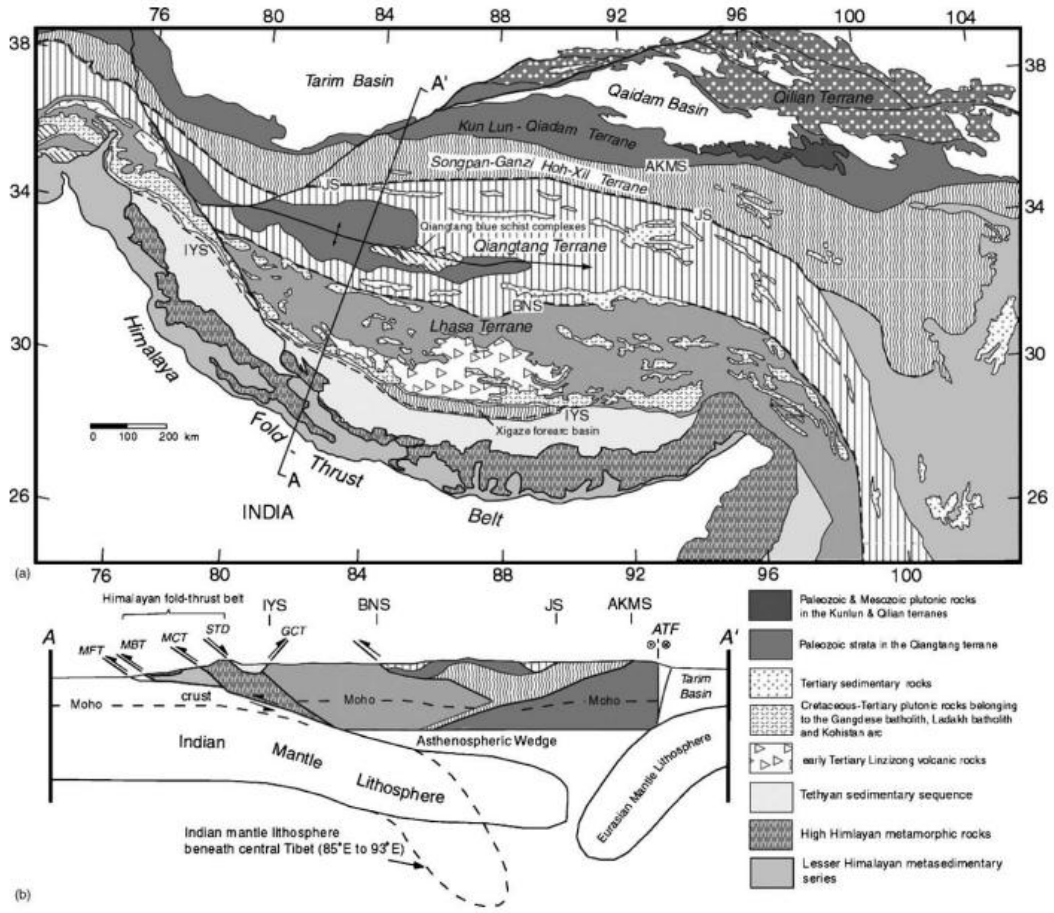

Figure 1.2 Schematic cross-section of the under-thrusting model. (a) Tectonic map of the Tibet-Himalaya collision zone modified from Yin and Harrison (2000). (b) Schematic cross-section (A-A′) across Tibet-Himalayan orogen [*Zhou and Murphy*, 2005]. Indian mantle lithosphere beneath central Tibet is interpreted to have been underthrust at a steeper angle than in the western and eastern portions. AKMS, Ayimaqin-Kunlun Mutztagh suture; BNS, Bangong-Nujiang suture; IYS, Indus-Yalu suture; JS, Jinsha suture; MFT, Main Frontal thrust; MBT, Main Boundary thrust; MCT, Main Central thrust; STD, South Tibet detachment; GCT, Great Counter thrust; ATF, Altyn Tagh fault; LM, lithospheric mantle.

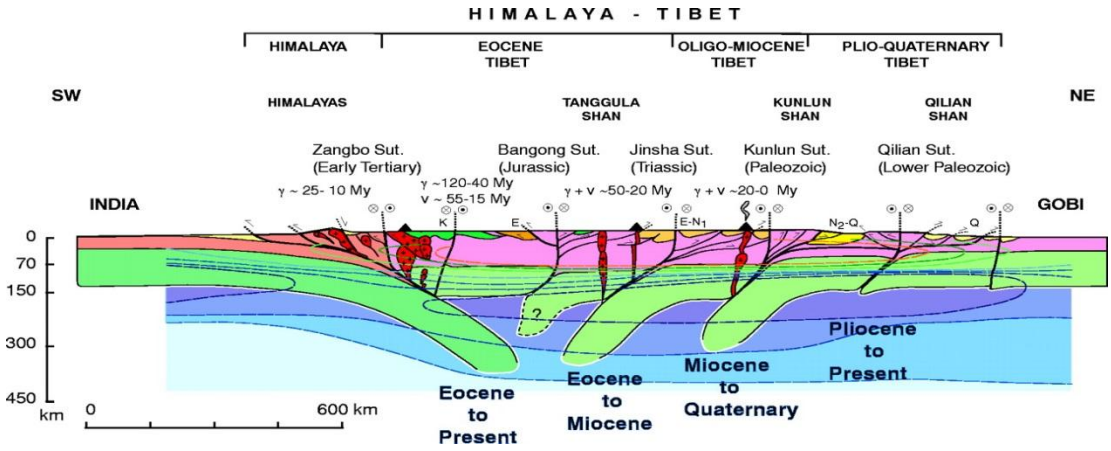

Figure 1.3 Schematic cross-section of the stepwise rise model [*Tapponier et al*., 2001]

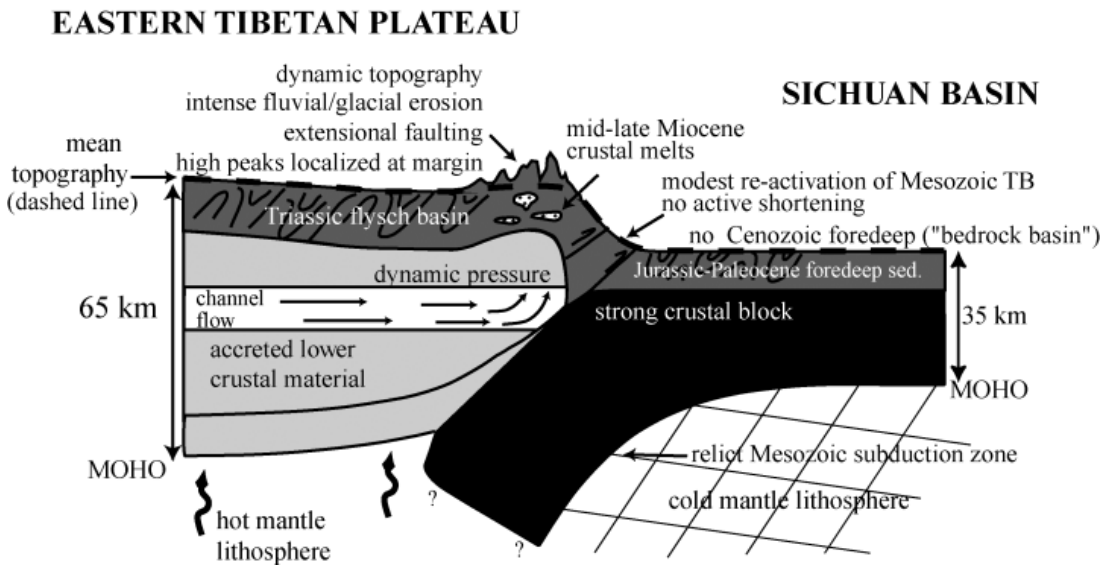

Figure 1.4 Schematic cross-sectional interpretation of the crustal flow model in the eastern plateau margin [*Clark et al.*, 2005].

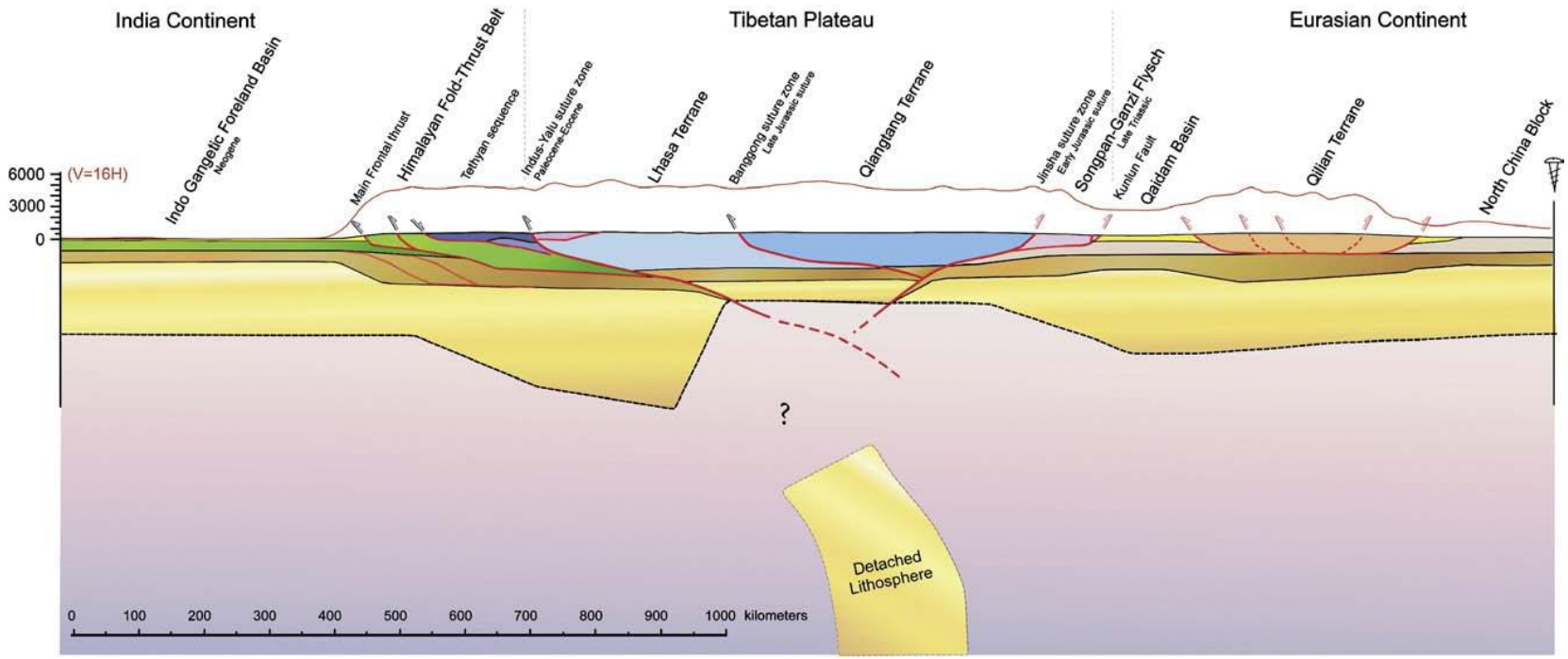

Figure 1.5 Schematic cross-section of the delamination model [*Jiménez-Munt et al.*, 2008].

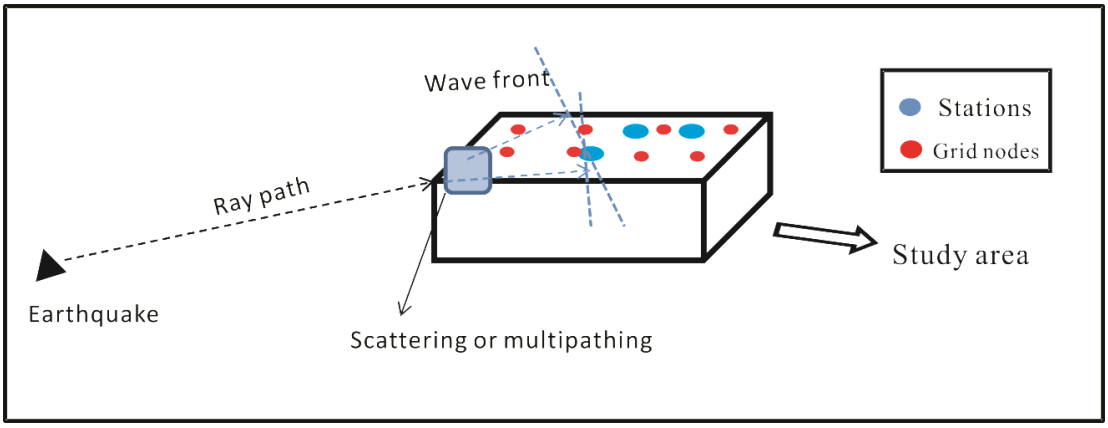

Figure 1.6 Cartoon for the Two-plane-wave (TPW) method. The TPW method represents the incoming wave field as the interference of two plane waves to overcome the effects of non-planar energy caused by scattering and multipathing.

Chapter 2. Shear Wave Structure in the Northeastern Tibetan Plateau from Rayleigh Wave Tomography

Abstract

The northeastern Tibetan Plateau is undergoing active horizontal shortening due to the India-Asia collision and is an ideal place for studying the growth of the plateau. To reveal deep structure that is responsible for producting the geologic features at the surface, I have constructed a 3-D shear wave velocity model from Rayleigh waves recorded by 36 stations in the Northeast Tibetan Plateau Seismic experiment. First, the two-plane-wave tomography method was applied to compute the average and 2-D variations of phase velocities in a period range of 20 to 100 s. Then 1-D and 3-D shear wave velocity models were developed from the obtained Rayleigh wave dispersions. The entire region is characterized by a weak upper mantle with a relatively thin lithosphere of ~80-100 km thick. This observation helps to explain the active deformation at the Kunlun Mountains and the Qinling Orogen in NE Tibet. Relative low velocity anomalies appear along and to the south of the Kunlun fault in contrast to high velocity anomalies in the north and northeast. One pronounced slow anomaly centered at ~120 km depth is imaged right beneath the restraining bend of the Kunlun fault, which might be a northern extension of the large-scale slow anomaly to the south of the fault. We interpret it as a local feature due to its large magnitude and coincidence with the restraining bend. It is probably related to anomalously high temperature and associated partial melting resulted from localized asthenosphere upwelling after the delamination of a thick lithosphere root. The

formation of the thick lithosphere root would require coherent shortening in the crust and mantle lithosphere caused by local compression due to the bend of the strike-slip fault, indicating that the Kunlun fault is probably on lithosphere scale and has played an important role in accommodating the eastward extrusion of the Tibetan Plateau.

Keywords: Tomography; Rayleigh wave; Shear wave velocity; Delamination; Tibet

2.1. Introduction

The Tibetan Plateau is the product of the ongoing Indo-Asian collision that began ~50 Ma ago [*Molnar et al.*, 1973; *Molnar and Tapponnier*, 1975; *Patriat and Achache*, 1984; *Molnar and Stock*, 2009; Zhu et al., 2005] and provides an excellent natural laboratory for studying the formation and development of continental plateaus (Figure 2.1). Convergence between the Indian and Eurasian plates has resulted in ~2000 km shortening and large-scale uplift since the initiation of the collision [*Molnar and Tapponnier*, 1975; Dewey et al., 1989]. Over the past two decades, considerable efforts have been made to understand the mechanisms of the growth and shortening of the Tibetan Plateau. However, where and how such large convergence was accommodated remains uncertain. Subduction of the Indian plate has been suggested to account for less than one-third of the convergence, while a series of strike-slip fault systems have accommodated one-half of the convergence through the plateau's eastward extrusion [*Harrison et al.*, 1992; *Le Pichon et al.*, 1992]. With a length of ~1,500 km trending in a nearly E-W direction, the Kunlun fault has long been identified as an active strike-slip fault system bordering the northern Tibetan Plateau. Over the last 40,000 years, slip of the Kunlun fault has led to a cumulative

offset of more than 400 meters [*Lin et al.*, 2002; *Van der Woerd et al.*, 2002] at a Quaternary slip rate of ~12 mm/yr [*Yin et al.*, 2008; *Wang et al.*, 2001; *Zhang et al.*, 2004; *Tapponnier et al.*, 2001]. It is therefore important to understand the dynamics of the Kunlun fault and explore its role in shaping the growth of the Tibetan Plateau.

Two end-member models have been proposed to explain the deformation of the Tibetan Plateau. One is the rigid block model [*Tapponnier et al.*, 2001], in which the major strike-slip faults in Tibet are considered as lithospheric-scale faults, accounting for both crustal thickening and eastward extrusion. This model provides a good interpretation for the formation of the Tibetan Plateau in general, especially for the southern part of the plateau, but has difficulties in explaining the formation and growth of mountain ranges in the east and north of Tibet. The other model is the viscous-flow model [*England and Houseman*, 1989; *Houseman and England*, 1993; *England and Molnar*, 1997; *Royden*, 1996; *Royden et al.*, 1997; *Clark and Royden*, 2000, 2005], which associates crustal thickening and deformation with viscous flow in the middle and lower crust. Most geophysical evidence using seismic tomography, magnetotellurics (MT), receiver function and shear wave splitting [e.g., *Brown et al*., 1996; *Chen et al*., 1996; *Kind et al.*, 1996; *Wei et al.*, 2001; *Royden*, 1996; *Royden et al*., 1997; *Clark and Royden*, 2000; *Sherrington et al.*, 2004] supports the existence of viscous flow in central, southern, and southeastern Tibet.

Whether the viscous-flow model is applicable in northern and northeastern Tibet is unclear due to a small number of high-resolution geophysical studies in this region and their contradicting implications. A recent seismic refraction study in NE Tibet [*Wang et al*., 2011] suggests that the middle crust is dominated by discrete sub-

horizontal shear zones that decouple the deformation in the crust from that in the mantle. However, fault-parallel fast directions from shear-wave splitting near the Kunlun fault suggest a coherent deformation in the crust and mantle lithosphere [*Li et al.*, 2011]. In addition, *Zhang Q. et al.* [2011] imaged a low velocity layer at the depths of 125-200 km beneath the Qilian-Qinling Orogen that lies between the Ordos and Sichuan blocks from Rayleigh wave tomography, implying the presence of east directed asthenosphere flow.

The NorthEast Tibetan Plateau Seismic experiment (NETS) [*Shen et al.*, 2008] aims to better understand the growth of the plateau. The area of the experiment contains highly-deformed orogenic belts, the Songpan-Ganzi Terrane (SGT) and the Qilian-Qinling Orogen (QQO), and the strong, less deformed Gobi-Ala Shan Platform (GAP). These tectonic provinces are separated by the Haiyuan fault (HF) in the north and the Kunlun fault (KF) in the south (Figure 2.1). This area has an average elevation of 3500 to 4000 m and undergoes active NE-SW shortening at a rate of ~13 mm/yr [*Chen et al.*, 2000]. In this study, we have applied Rayleigh wave tomography in the NE Tibetan Plateau using seismic data recorded at the NETS stations [*Shen et al.*, 2008] and obtained high-resolution phase and shear velocity models. These velocity models reveal seismic structure in the lower crust and upper mantle and shed light on the deformation process operating in the lithosphere beneath the NE Tibetan Plateau.

2.2. Data Analysis

We analyzed Rayleigh wave data recorded by the NETS array, which operated from July 2008 to July 2010. Thirty-six broadband stations in the NETS array were deployed in the NE Tibetan Plateau across the SGT, the QQO and the GAP from south to north (Figure 2.1). Seven stations continuously recorded data during the 2-year experiment and other stations recorded data from several months to 1 year. Twenty-seven CMG3ESP sensors and nine CMG3TD sensors were used in the experiment. We utilized the CMG3ESP response as a reference and converted seismograms recorded by CMG3TD sensors to the reference response before extracting Rayleigh waves.

Teleseismic events with magnitude ≥ 5.8, focal depth ≤ 100 km, and epicental distance between 25^{o} and 120^{o} were selected. This selection resulted in over 200 potential events for Rayleigh wave analysis. Vertical component seismograms from these events at 36 stations were filtered at 14 center frequencies (10, 11, 13, 15, 17, 20, 22, 25, 29, 33, 36, 40, 45 and 50 mHz) with a series of 10 mHz wide, zero-phase, 4^{th} order Butterworth filters. A narrow time window was applied to the fundamental mode Rayleigh waves to separate them from other phases (Figure 2.2). To ensure data quality, we visually inspected individual waveform for its signal/noise ratio and consistence with that at nearby stations. Seventy-six events with high quality Rayleigh waves were retained after the inspection. These events (Figure 2.3) have good azimuthal coverage from NE to SE because many earthquakes originated from the subduction zones in the west Pacific. An example of ray path coverage is given in Figure 2.4 for the period of 33 s. Despite variable ray path density in the study area,

crossing ray paths are dense within the station network as well as in its vicinity especially to the east. The variation of ray path density is similar at different periods, although the total number of ray path becomes smaller at very short and long periods.

Fourier analysis was applied to determine amplitude and phase of Rayleigh wave trains in different frequency bands after correcting instrument responses, filtering and windowing the records. Geometrical spreading and attenuation compensation were conducted as described by *Li et al*. [2003]. The attenuation coefficients used herein are from *Mitchell* [1995] for tectonically active regions. The amplitude and phase information from Fourier analysis are used for calculating the 1-D and 2-D phase velocities.

2.3. Method

A two-step inversion procedure was carried out to obtain shear wave velocity structure. The first step was to determine phase velocities from the amplitude and phase of Rayleigh waves at different periods. The second step was to develop shear wave velocity structure at different depths from the obtained phase velocities.

2.3.1. Phase Velocity Inversion

We adopted the two-plane-wave (TPW) inversion method using Gaussian sensitivity functions [*Forsyth et al*., 1998; *Forsyth and Li*, 2005] to obtain 1-D average phase velocities at different periods. 2-D, Born approximation sensitivity kernels were calculated using the average phase velocities at each frequency and were utilized to determine 2-D phase velocities. Heterogeneity between source and station would induce multipath propagation of Rayleigh waves and affect the amplitude and

phase of Rayleigh waves [*Friederich et al*., 1994]. The TPW method, which treats the incoming wavefield as the interference of two plane waves, can overcome the effects of non-planar energy caused by scattering and multipathing and effectively solve phase velocities within a seismic array [*Li et al*., 2003; *Forsyth and Li*, 2005; *Yang and Forsyth*, 2006].

For a given frequency ω, the incoming wave filed is considered as the interference of two plane waves represented by the following expressions in polar coordinates (r,ψ) centered on the reference station and oriented in the great-circle path [*Forsyth and Li*, 2005].

$$ {}_i^k U = {}_i A_1 \exp(-i\,{}_i^k \phi_1) + {}_i A_2 \exp(-i\,{}_i^k \phi_2) \qquad (2.1) $$

Where ${}_i^k \phi_1 = {}_i^0 \phi_1 + \overline{{}_i^k S}\omega\left\{ {}_i^k r \cos\left({}_i^k \psi - {}_i \vartheta_1 \right) - {}_i^k x \right\} + \omega({}_i^k \tau - {}_i^0 \tau)$

and

$${}_i^k \phi_2 = {}_i^0 \phi_2 + \overline{{}_i^k S}\omega\left\{ {}_i^k r \cos\left({}_i^k \psi - {}_i \vartheta_2 \right) - {}_i^k x \right\} + \omega({}_i^k \tau - {}_i^0 \tau);$$

${}_i^k U$ is total displacement; ${}_i A_1$ and ${}_i A_2$ are the amplitude of the two plane waves, respectively; ${}_i^0 \phi_1$ and ${}_i^0 \phi_2$ are the phases of the two waves at the reference station; ${}_i^k \tau$ and ${}_i^0 \tau$ are the travel times along the ray path from the edge of the study area to the *k*-th and reference station; ${}_i \vartheta_1$ and ${}_i \vartheta_2$ are the angular deviations from the ray path of the two waves, $\overline{{}_i^k S}$ is the average slowness for each ray path. Details on how ${}_i^k \tau$ and $\overline{{}_i^k S}$ are calculated can be found in *Forsyth and Li* [2005].

The study area was parameterized with 270 grid nodes with a spacing of ~55 km. The trade-off between model variance and model resolution is controlled by the

characteristic length in the Gaussian weighting function. Following [*Li et al*., 2003], we used a characteristic length of 80 km for all frequencies to smooth the phase velocity models because of similar station spacing in these two studies. A smaller characteristic length will produce more smaller-scale variations in phase velocity models but will increase the variance on model parameters. We assigned a priori error of 0.25 km/s at the inner nodes and 2.5 km/s at the edge nodes (the most outside two rows and columns), which help to absorb anomalous phase and amplitude data that cannot be represented by the two plane waves.

The parameters of the two plane waves (i.e., amplitudes, initial phases, and propagation directions) are first estimated using a simulated annealing method [*Press et al*., 1992] and subsequently solved simultaneously with phase velocities in a generalized linear inversion [*Tarantola and Valette*, 1982]. Gaussian smoothing functions are used in solving the average phase velocity in the entire area and three sub-regions. Since replacing the Gaussian smoothing functions with 2-D, Born sensitivity kernels improves model resolution of phase velocities in the TPW method [*Yang and Forsyth*, 2006; *Li*, 2011], 2-D, Born sensitivity kernels are calculated using the determined average phase velocities and used in the inversions for 2-D phase velocity models.

2.3.2. Shear Wave Velocity Inversion

The second step is to determine shear wave structures from the obtained phase velocities with a generalized linear inversion. The data for the inversion are the phase velocities at the 14 periods from 20 to 100 s. The model parameters are crustal thickness and shear wave velocities in 16 layers from the surface to the top of the

transition zone (410 km). We used the method of *Saito* [1988] to calculate the derivatives of phase velocity regarding model parameters [*Li and Burke*, 2006]. At a given period, Rayleigh wave phase velocity is primarily sensitive to S wave velocity at a broad depth range with a peak sensitivity at 1/3 of the wavelength (Figure 2.5a). Its sensitivity to P wave velocity is confined at much shallower depths, for example largely above 50 km at a period of 100 s (Figure 2.5b). P wave velocity in the model is associated with the shear wave velocity with a fixed Vp/Vs ratio of $\sqrt{3}$.

Letting $\mathbf{m_0}$ be a starting model, synthetic data are $\mathbf{d_0}$ = g($\mathbf{m_0}$). The solution to the general, nonlinear, least squares inversion is given by

$$\Delta m = (G^T C_{nn}^{-1} G + C_{mm}^{-1})^{-1}[G^T C_{nn}^{-1} \Delta d - C_{mm}^{-1}(m - m_0)] \qquad (2.2)$$

where $\mathbf{m}$ is the current model, $\Delta\mathbf{m}$ is the change to the current model, $\Delta\mathbf{d}$ is the difference between the predicted and observed data, $\mathbf{G}$ is the Fréchet derivative of the operator g, $\mathbf{C}_{nn}$ is the a *priori* data covariance matrix, and $\mathbf{C}_{mm}$ is the a *priori* model covariance matrix. Off-diagonal terms are introduced into $\mathbf{C}_{mm}$ to smooth the solution. $\mathbf{C}_{nn}$ is assumed to have only diagonal terms, which are standard errors from the inversions for phase velocities. The inversion also apply penalty for deviation from the initial model $\mathbf{m}_0$. Model parameters that are not well constrained by the data will be close to the starting values.

We first performed the inversion to determine 1-D shear velocity. The starting model is based on the AK135 model [*Kennett et al*., 1995]. We modified the crustal structure in the AK135 model to fit that in NE Tibet. The modified model consists of 3 layers in the crust with a total crustal thickness of 54 km for 1-D shear wave velocity inversion. A *priori* standard errors of 0.1 km/s to shear wave velocities and 3

km to crustal thickness were assigned to allow small perturbations to the initial model. Additionally, we applied a correlation coefficient of 0.4 between adjacent layers to smooth the model.

The 3-D shear velocity model is obtained by applying 1-D inversion at each grid node. Crustal thickness is an important model parameter in the inversion and has a tradeoff with shear wave velocities in the lower crust and shallow upper mantle. To have a reasonable crustal thickness in the starting model for each grid node, we constructed a starting crustal thickness map based on previous receiver function studies [*Du et al*., 2011; *Pan and Niu*, 2011] and refraction studies [*Galve et al*., 2002; *Liu el al.*, 2006; *Zhang Z. et al*., 2011] (Figure 2.6). The crustal thickness varies signifcantly in the study area from 44 km in the east and north to 64 km in the southwest.

2.4. Resolution Tests for Phase Velocity Variation

We carried out resolution test to understand resolvability of phase velocities and their spatial resolution at different periods in the study area. A checkerboard velocity model with a cell size of $1.5^{o} \times 1.5^{o}$ was constructed and it contained alternating positive and negative perturbations of ±3% with an average velocity of 4 km/s (Figure 2.7a). Synthetic incoming wave field for each event is assumed as the sum of two plane waves with known initial amplitude, phase and propagation direction. The choice of the two plane waves is arbitrary. One plane wave propagates at 4° off the great-circle path with an initial amplitude of 0.7 and the other travels at 10° with an amplitude of 0.3, which are typical observed directions and normalized amplitudes

for the primary and secondary plane waves, respectively. The initial phase for both plane waves is set as zero. Then synthetic amplitude and phase of Rayleigh waves were computed from the checkerboard model using the same stations, events, and raypaths from the real data. Random noises of 10% of the maximum phase and amplitude values were added to the synthetic data. These synthetic data with noise were used to calculate 2-D phase velocity using the same inversion scheme as was applied to the real data. As shown in Figure 2.7, the pattern of the velocity anomalies within and close to the station array (inside the 2% error contour) can be well recovered at 25, 50 and 91 s (Figure 2.7b, 2.7c, 2.7d). However, fading and smearing occur around the edge of the model where large errors were given at the edge nodes and crossing raypaths are not dense (Figure 2.7b, 2.7c and 2.7d). Based on the resolution test and model variance from the inversions, our discussion below mainly focuses on robustly determined features.

2.5. Results

2.5.1. 1-D Rayleigh Wave Phase Velocity

Average phase velocities for the entire study region were obtained at the periods of 20, 22, 25, 28, 30, 33, 40, 45, 50, 59, 67, 77, 91, and 100 s and vary from 3.21 km/s at 20 s to 3.84 km/s at 100 s (Figure 2.8a). In this inversion, phase velocity at all grid nodes is assumed to be the same and only one model parameter for phase velocity is solved along with the two-plane wave parameters. The standard error for each phase velocity is taken from a posteriori model covariance matrix calculated in the inversion. These phase velocities are significantly lower than those predicted

from the global model AK135 (Figure 2.8a), indicating a much thicker crust and slower uppermost mantle. While compared to the average phase velocities in southeastern (SE) Tibet [*Fu et al*., 2010], these values are higher in the period range of 20-45 s and lower at longer periods (Figure 2.8a). This observation reflects that the crust in NE Tibet is probably thinner than that in the SE Tibet while the upper mantle is much slower in NE Tibet.

The study area can be divided into three sub-tectonic-provinces, the SGT, the QQO, and the GAP, that are separated by the Kunlun and Haiyuan faults (Figure 2.1). The inversion for the average phase velocity in each province is conducted by assuming same phase velocity at all the nodes within one province (Figure 2.8a). Phase velocities generally decrease from the GAP in the north to the SGT in the south. The GAP is characterized with the highest velocities ranging from 3.35 km/s at 20 s to 4.20 km/s at 91 s while the SGT has the lowest velocities from 3.15 km/s at 20 s to 3.81 km/s at 91 s. The QQO in the middle of the study area has phase velocities that are comparable to the average phase velocities for the entire study region (Figure 2.8a). The large difference in phase velocities among the three sub-regions reveals strong lateral variations in the crust and upper mantle in the NE Tibetan Plateau.

2.5.2. 2-D Rayleigh Wave Phase Velocity

2-D phase velocities were calculated at the periods from 20 s to 100 s using the 1-D average phase velocities as starting values. The maps of phase velocity anomaly at the periods of 20, 30, 33, 45, 59, 77, 91 and 100 s are shown in Figure 2.9a-h. The standard error of phase velocity was estimated from model covariance matrix and its distribution across the study area is shown in Figure 2.9i. The standard errors at

different periods have similar pattern with small errors near the center of the study region and increasing errors towards the edge. The phase velocity maps are clipped by the 3% contour of 2σ at 33 s. The 2-D phase velocities change gradually among nearby periods due to overlapped frequency bands and depth sensitivity at nearby frequencies. A low velocity anomaly (up to -6%) is imaged along and to the south of the Kunlun fault at 20-33 s (Figure 2.9a-c), reflecting a slow or thicker crust. Velocities at short periods increase gradually northward, likely implying that crustal thickness decreases from the SGT to the GAP. This implication is consistent with the variation of crustal thickness obtained from the previous studies (Figure 2.6b) [*Galve et al.*, 2002; *Liu el al.*, 2006; *Zhang Z. et al.*, 2011; *Du et al.*, 2011; *Pan and Niu*, 2011]. The slow anomaly of phase velocity is also consistently imaged at 40-100 s, which are primarily sensitive to the depths of 50-150 km, indicating a slow or thin lithosphere beneath the Kunlun fault. This is a well resolved feature; the magnitude of the anomaly is still more than 2% at the longest period and is well above the 1% 2σ value at this location.

2.5.3. 1-D Shear Wave Velocity (V_{SV})

In order to derive geological information of NE Tibet, we performed a generalized linear inversion to produce shear wave velocity model from phase velocities. The resolution of shear wave velocity model can be evaluated from the resolution matrix calculated from the inversion. As shown in Figure 2.10, the peak values at the rows of resolution matrix for the 1-D reference model varies from 0.68 at 25 km to 0.3 at 110 km, indicating that resolution for shear wave velocity generally decreases with increasing depth. Although shear wave velocity in each layer cannot

be independently resolved, the values in the resolution matrix suggest that the average velocity of 40 km in the crust and of 60 km in the shallow upper mantle can be well determined when the sum of the adjacent peak values reaches to 1. Despite of reduced sharpness, the peaking values can still be clearly recognized at 150 km, indicating reasonable resolution at this depth. We therefore focus our description and discussion on velocity models above 150 km depth.

Compared to the AK135 model, shear wave velocity in the average 1-D model of the study area is significantly slower in the lower crust and upper mantle with velocity of 3.59 km/s at 35 km and 4.05 km/s at 140 km (Figure 2.8b). Similar low velocity anomalies are observed by *Zhang Q. et al*. [2011] in a region slightly southeast to our study area. However, the shear wave velocity values from *Zhang Q. et al.* [2011] are ~0.3 km/s higher than those from this study at corresponding depths. This difference between the two studies is reasonable for the change of tectonic provinces from plateau and mountain ranges in the west to strong basin and platform in the east.

1-D shear wave velocity models for the three sub-regions were determined from their corresponding average Rayleigh wave dispersions (Figure 2.8b). Based on crustal thickness from the previous receiver function studies [*Pan and Niu*, 2011; *Du et al.*, 2011] and the refraction seismic studies [*Galve et al.*, 2002; *Liu el al*., 2006; *Zhang Z. et al*., 2011], we fixed the average crustal thickness in the inversions at 50 km for the SGT, 54 km for the QQO, and 58 km for the GAP. Shear wave velocities in the GAP are in agreement with the AK135 model. Shear wave velocities in the QQO are comparable to the average shear wave velocity of the entire study area,

while shear wave velocities in the SGT are much lower in the lower crust and shallow upper mantle from 35 to ~140 km than the average of the whole area. These 1-D velocity models clearly illustrate strong lateral variation of shear wave structure in NE Tibet, which can be better viewed from the 3-D model.

2.5.4. 3-D Shear Wave Velocity (V_{SV})

A 3-D shear wave velocity model was developed by combining 1-D shear wave models at all grid nodes. The absolute shear wave velocity maps at 6 layers from the lower crust to 150 km are shown in Figure 2.11 and a cross-section of absolute shear wave velocity and velocity perturbation are shown in Figure 2.12. The profile A-A' is roughly perpendicular to the Kunlun fault and the Haiyuan fault, crossing the SGT, the QQO, and the GAP.

Similar to the anomaly pattern in phase velocity maps, pronounced low shear wave velocities appear at the Kunlun fault in the lower crust and extends to at least 150 km depth (Figure 2.11 and 2.12c). The low velocity anomaly shifts a little westward along the Kunlun fault with increasing depth. The center of the anomaly is up to -3% and located right beneath the bend of the eastern Kunlun fault (Figure 2.12c). This anomaly is relative to the already low velocity in the 1-D average model and its absolute shear velocity is about 4 km/s, which is 0.5 km/s slower than the global average. The slow anomaly at the bend of the eastern Kunlun fault was also imaged in a recent P wave tomography model [*Zhang et al.*, 2012]. Our absolute shear velocities, although very low, are consistent with those from large scale Rayleigh wave tomography in NE Tibet [*Chen et al*., 2010]. The high velocity anomalies in the lithosphere are observed in the relatively low elevation areas in the

Qilian-Qinling Orogen (Figure 2.11), close to the Qaidam Basin. The relative high velocity lithosphere is presumably strong and resistant to large deformation as occurred in the surrounding region.

2.6. Discussion

One main observation from our study is a generally slow upper mantle with a low velocity layer at the depths of 80 km to 140 km beneath NE Tibet (Figure 2.8b and 2.12b). Similar low velocity anomalies are observed in northern Tibet in regional Rayleigh wave tomography [*Chen et al.*, 2010; *Zhang Q. et al*., 2011]. A sharp velocity drop starts at ~80 km depth beneath the Songpan-Ganzi Terrane and at ~100 km beneath the Qilian-Qinling Orogen (Figure 2.8b and 2.12b), indicating a shallow lithosphere-asthenosphere boundary (LAB). A similar velocity drop is also observed in a large-scale shear wave velocity model, but at the depth of ~110 km in the same region [*An and Shi*, 2006]. Our observation of LAB is 30-50 km shallower than that in *An and Shi* [2006], who estimated the lithosphere thickness beneath the northeastern Tibetan Plateau and the Qinling Orogen at ~110-150 km. The differences among these studies are due to different data, methods, and different criteria of defining the LAB in different studies. For instance, the LAB in this study is based on seismic velocity reduction while the LAB from *An and Shi* [2006] is based on temperature variation with depth. An overall thin and weak lithosphere in this area could explain the high elevation in the Kunlun Mountain and Qilian-Qiling Orogen to the first order and the relatively high heat flow values in the NE Tibetan Plateau observed from a large-scale heat flow map [*Hu et al*., 2000].

Our model shows relative low velocity anomalies along and to the south of the Kunlun and high velocity anomalies in northeast (Figure 2.11). To the first order, this observation is consistent with large-scale tomography models in Tibet [*McNamar et al*., 1997; *Liang and Song*, 2006; *Pei et al*., 2007; *Huang and Zhao*, 2006; *Li et al.*, 2006; *Yang et al.*, 2010, *Li and van der Hilst*, 2010; *Obrebski et al.*, 2012] that generally imaged low velocity anomalies beneath the Songpan-Ganzi Terrane with the Kunlun fault as the northern boundary, indicating a hot and deformable lithosphere.

The most interesting feature in the 3-D model of NE Tibet is a local low velocity anomaly in the shallow upper mantle beneath the restraining bend of the Kunlun fault (Figure 2.11 and Figure 2.12c), where high topography and thick crust are observed (Figure 2.1, 2.6, and 2.11). Is this anomaly a local feature or a simple extension of the anomaly beneath the Songpan-Ganzi Terrane as imaged in large-scale models [*Yang et al.*, 2010, *Li and van der Hilst*, 2010; *Obrebski et al.*, 2012]? We conducted additional resolution tests to address this question. In the first test, we used an input model with the Kunlun as the boundary separating -3% phase velocity anomaly to the south from +3% anomaly to its north. The pattern of phase velocity anomalies can be well recovered at all periods (Figure 2.D1), demonstrating that a broad and uniform slow anomaly to the south of the Kunlun cannot be mapped as a local slow anomaly under the Kunlun bend. Then we added -3% and -5% anomaly at the bend of the Kunlun to the first model (Figure 2.D2 and 2.D3, respectively). If the local slow anomaly at the Kunlun bend is a simple extension of the large-scale anomaly (with the same magnitude anomaly at the bend of the Kunlun, Figure 2.D2), the experiment

shows that the recovered anomaly is stronger at the Kunlun bend at some periods (e.g., 33 and 91 s) and appears as a local anomaly, but not at all periods (for instance at 59 s). If the anomaly at the Kunlun bend is stronger than the broad slow anomaly to the south due to local contribution (Figure 2.D3), such anomaly distribution can be well recovered at all periods, which are consistent with the observations. So although we cannot completely rule out the possibility that the imaged local slow anomaly at the Kunlun bend is part of the large-scale slow anomaly in Tibet, the observations suggest a local variation or contribution.

The cause of such a local low velocity anomaly at the bend of the Kunlun may hold a key question to understanding the dynamics of the Kunlun fault and its role in forming the NE Tibet plateau. One possible explanation for the slow anomaly is Songpan-Ganzi flysch, a Triassic-Permian shale deposited in a remnant ocean basin and subducted in the Triassic [*Kapp et al., 2000*]. However, the subduction of the Songpan-Ganzi flysch is suggested at a low angle, which is different from the sub-vertical anomaly geometry in the shear wave velocity model (Figure 2.12). In addition, the observed slow anomaly is right beneath the Kunlun fault, not in the Songpan-Ganzi Terrane where the flysch is identified (Figure 2.1). We therefore conclude that the Songpan-Ganzi flysch is unlikely the cause of the observed low velocity anomaly beneath the Kunlun fault.

This low-velocity anomaly could be caused by high temperature and associated partial melt. A 100 °C increase of temperature in the shallow mantle would yield a 1.1% decrease of shear wave velocity [*Nataf and Richard*, 1996]. Then, a -3% velocity anomaly would correspond to a ~300 °C high temperature excess. Such

anomalous high temperature would induce partial melting in the uppermost mantle. The absolute shear wave velocity at the center of the anomaly at 120 km depth is about 4.0 km/s, which is comparable to that beneath Iceland, an area with hotspot and mid ocean ridge [*Li and Detrick*, 2006], and requires the presence of partial melt. This is not a surprising result as widespread partial melting in the Tibetan Plateau has been suggested in a variety of studies [e.g., *Arnaud et al*., 1992; *Yang et al*., 2010; *McNamara et al*. 1994, 1997; *Owen and Zandt*, 1997; *Guo et al.*, 2006].

The question is why the temperature beneath this segment of the Kunlun fault is elevated. Given that the Kunlun is a major strike-slip fault in Tibet, shear heating might account for part of the suggested high temperature. In fact, shear heating has been proposed beneath the Red River Fault [*Leloup et al.*, 1993, 2001; *Scharer et al*., 1990] and the Altyn-Tagh fault [*Van der Woerd et al*., 1998; *Wittlinger et al.*, 1998] in Tibet. However, it is concluded that shear heating could not usually increase temperature more than 200 °C along the Kunlun fault with a slip rate of 10-12 mm/yr [*Fleitout and Froidevaux*, 1980; *Leloup et al.*, 1999]. Moreover, the eastern Kunlun fault has a lower slip rate (~2 mm/yr) [*Kirby et al.*, 2007] and has been suggested to be a crustal level fault from seismic reflection tomography [*Wang et al.*, 2011]. Therefore the low velocity anomaly centered at ~120 km depth requires other contributions to account for the high thermal anomaly.

Another heat source for the low velocity anomaly beneath the Kunlun fault is from asthenosphere upwelling caused by removal of a thick lithosphere root. The low velocity anomaly is located right at the restraining bend of the Kunlun fault, which was documented geomorphologically by *Harkins et al.* [2010] (Figure 2.1). Here the

slight change of the strike direction could result in local compression and thickening of the lithosphere. The large slip rate of 10-12 mm/yr on both east and west ends of the eastern Kunlun bend [*Van der Woerd et al.,* 2002] suggests local compression could be significant at the Kunlun restraining bend. The total shortening would approximately be in a range of 65-120 km assuming that the Kunlun fault initiated at 15-8 Ma [*Fu and Awata,* 2007; *Jolivet et al.,* 2003; *Kirby et al.,* 2007]. Pronounced shortening is indicated by large duplex structures imaged in a refraction seismic profile across this area [*Wang et al.,* 2011]. Thick crust in this area (Figure 2.6) [*Galve et al.,* 2002; *Liu el al.,* 2006; *Zhang Z. et al.,* 2011; *Du et al.,* 2011; *Pan and Niu,* 2011] is also evident for local compression at the eastern Kunlun restraining bend. However, a low velocity anomaly and a relatively thin lithosphere are imaged beneath the thick crust rather than a fast anomaly and thick lithosphere as expected in this locally compressional setting. This apparent paradox can be easily understood as a result of the delamination of a thick lithosphere root.

The process and consequence of lithosphere delamination have been investigated by several researchers using numerical models [*Elkins-Tanton,* 2005; *Elkins-Tanton,* 2007; *Houseman and Molnar,* 1997]. A thick lithosphere root caused by local compression at the restraining bend was colder and denser than the surrounding asthenosphere, which produced gravity instability and resulted in root delamination. As the dense lithosphere sinks, the asthenosphere is sucked into the resulting lithospheric dome and may melt adiabatically [*Elkins-Tanton,* 2005; *Elkins-Tanton,* 2007]. Additionally, the removed and sinking lithosphere material would trigger further melting due to dehydration as it reaches higher temperatures and pressures

[*Elkins-Tanton*, 2005; *Elkins-Tanton*, 2007]. The presence of ~1% partial melt in the upper mantle would give ~2-4% Vs variations [*Takei*, 2000], consistent with our observations. The fact that no active volcanism occurs above the slow anomaly is probably due to a relatively low melt production, and the thick crust and a local compressional environment that are not conducive to melt migration to the surface. Further quantitative geodynamic modeling is required to better understand such process at the restraining bend of the Kunlun fault with more realistic geological and geophysical constraints, which is beyond the scope of this paper.

Whether the Kunlun fault is on a crustal or lithospheric scale is important for understanding its response to the collision between the Indian and Eurasian plates. The results from receiver function [*Vergne et al*., 2002] and the fault-parallel fast directions from anisotropy [*Li et al*., 2011; *Zhang Q. et al*., 2011] have suggested that the Kunlun fault likely penetrates to the lithospheric mantle, consistent with suggestions from many previous studies [*Tapponnier et al*., 2001; *Chung et al.*, 2005; *Herquel et al.*, 1999, *Herquel and Tapponnier*, 2005; *Kind et al.*, 2002]. However, a seismic refraction study [*Wang et al*., 2011] across the eastern Kunlun imaged sub-horizontal reflectors in the middle crust and argued for the decoupling deformation between the crust and the mantle. We observed a local slow anomaly in the shallow upper mantle beneath a thick crust at the bend of the Kunlun fault and interpreted the slow anomaly as asthenosphere upwelling caused by the removal of a locally thickened lithosphere. In this scenario, the compression at the bend of the fault strike caused coherent deformation in the crust and mantle lithosphere to produce a thick lithosphere root, implying that the Kunlun is a lithosphere-scale fault. In addition, no

low velocity layer is imaged in the lower crust of the Kunlun in NE Tibet. The Kunlun fault could have penetrated in the mantle lithosphere on a broad scale and accommodated large parts of the plateau's eastward extrusion resulted from the ongoing collision between India and Eurasia.

2.7. Conclusions

We have computed average and 2-D phase velocities and then determined 1-D and 3-D shear wave structure from Rayleigh wave data recorded at the NETS array. The average shear wave models in the Songpan-Ganzi Terrane and the Qilian-Qinling Orogen are characterized by a slow upper mantle with a sharp velocity reduction at ~80-100 km, implying a shallow lithosphere-asthenosphere boundary. The generally thin and slow mantle lithosphere is probably mechanically weak and easily deforms. This observation helps to understand active deformation and vigorous plateau building processes in NE Tibet. The low velocity layer from 80 to 140 km indicates a hot and weak asthenosphere, which might be caused by a regional-scale lithospheric removal in NE Tibet or heated up from the hot asthenosphere in central Tibet.

A significant low velocity anomaly up to -3% is observed beneath the restraining bend of the eastern Kunlun fault centered at ~120 km depth. We interpret this anomaly as a local feature although it cannot be completely excluded that it is the northern extension of the large-scale anomaly to the south of the Kunlun. The low velocity anomaly is probably caused by high temperature and associated partial melting from asthenosphere upwelling resulted from localized detachment of a thick lithosphere root. Viscous strain heating due to slip along the Kunlun fault may also

account for part of the high thermal anomaly in the crust but cannot be the main cause of the anomaly. The removed thick lithosphere root would have required coherent deformation in the crust and mantle. In addition, no low velocity layer is imaged in the lower crust beneath the eastern Kunlun. The Kunlun fault in NE Tibet is therefore probably a lithosphere-scale fault and accommodates large amount of the plateau's eastward extrusion.

2.8. Appendix

Appendix 2.A: Comparison of predicted and observed Rayleigh wave amplitudes and phase at 50 s.

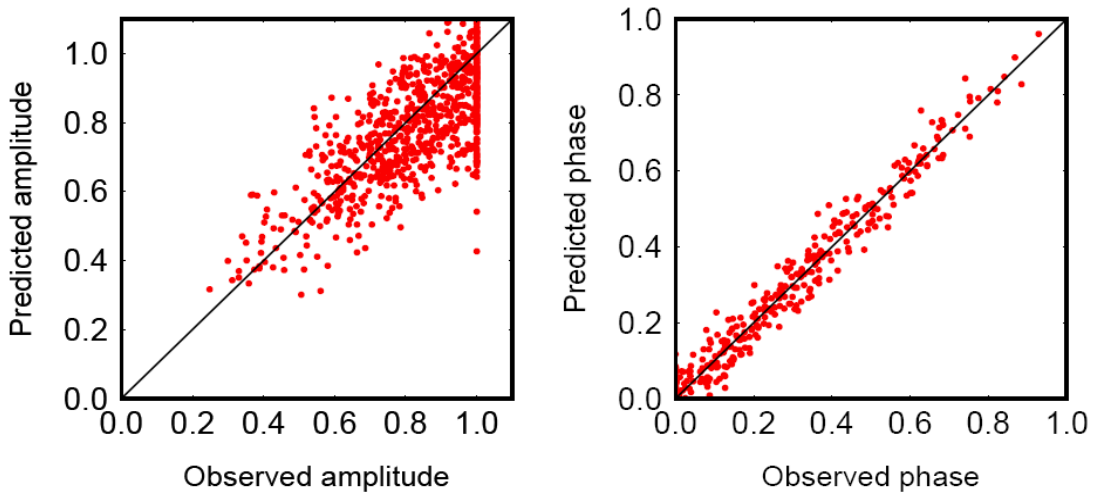

Figure 2.A. Comparison of predicted and observed Rayleigh wave amplitudes and phase at 50 s.

Appendix 2.B: The complexity of incoming Rayleigh wave wavefield

The complexity of incoming wavefields is reflected in Figure 2.Ba, showing the amplitude ratio between the smaller and the larger plane wave at 25 s. Sixteen of 76 events have the amplitude ratio larger than 0.5, indicating significant multipathing or

scattering along the raypath (Figure 2.Ba). In addition, most primary plane waves, the one with the larger amplitude, lie within 5° from the great-circle path (Figure 2.Bb), while the propagation directions of secondary waves are much more scattered (Figure 2.Bc).

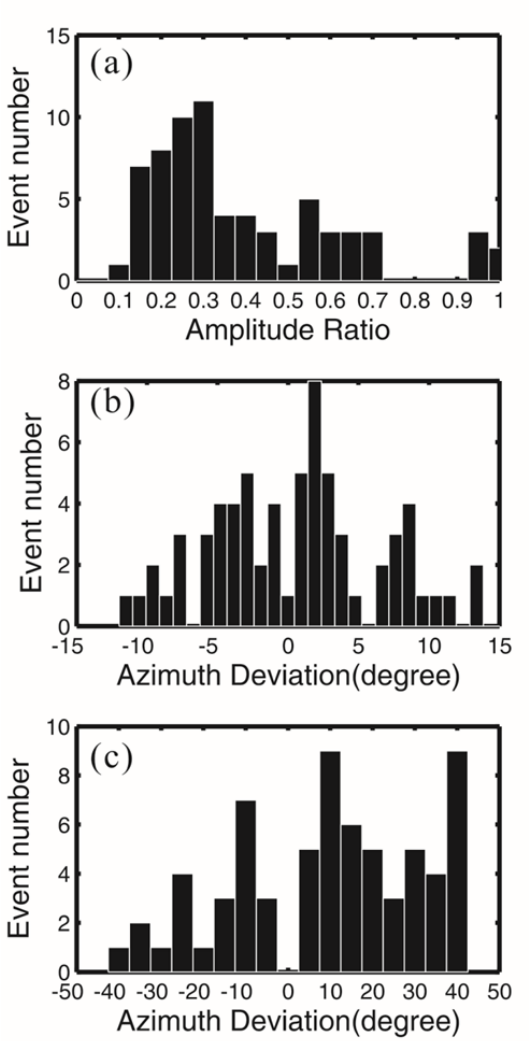

Figure 2.B (a) Amplitude ratios of the smaller of the two plane waves to the larger. (b) Deviation of the propagation directions of the primary plane waves from the great-circle directions of the events at 25 s. (c) Same as Figure 2.Bb but for the secondary plane waves.

Appendix 2.C: 2-D Born Sensitivity Kernels

Ray theory breaks down when the length scale of lateral structure is smaller than the seismic wavelength because of the finite frequency of seismic waves. 3-D surface wave sensitivity kernels were developed by *Zhou et al.* [2004] to account for the finite-frequency effects. Based on a forward-scattering approximation, the 3-D Born kernels can be reduced to form the 2-D sensitivity kernels expressing the sensitivities to the local phase velocity perturbation, $\delta c / c$. They are defined as

$$\delta d = \iint_{\Omega} K_d^c(\hat{\mathbf{r}}, \omega)(\delta c / c) d\Omega$$

where the integration is over the unit sphere, $\hat{\mathbf{r}}$ is the vertical unit vector, and ω is the angular frequency [*Zhou et al.*, 2004]. δd can be the phase delay, $\delta\phi$, or the relative amplitude variation, $\delta \ln A$, with corresponding phase kernel $K_{\phi}^c(\hat{\mathbf{r}}, \omega)$ or amplitude kernel $K_A^c(\hat{\mathbf{r}}, \omega)$.

Yang and Forsyth [2006] modified the 2-D sensitivity kernels from *Zhou et al.* [2004] for an incident plane-wave on the Earth's surface, and applied them in the TPW method for regional Rayleigh wave tomography. According to *Yang and Forsyth* [2006], the 2-D sensitivity kernels for a plane wave are described as

$$k_{\phi}^c(\hat{\mathbf{r}}, \omega) = Im\left(\frac{k^2 R'' e^{-i[kx'' - k\Delta x + \pi/4]}}{R\sqrt{2\pi k x''}} \right), \qquad k_A^c(\hat{\mathbf{r}}, \omega) = -\mathrm{Re}\left(\frac{k^2 R'' e^{-i[kx'' - k\Delta x + \pi/4]}}{R\sqrt{2\pi k x''}} \right)$$

where k is the wave number of surface waves, x'' is the distance from a scatter to a receiver and Δx is the differential propagating distance between the direct incoming wave arriving at the receiver and arriving at the scatter; R and R'' are receiver polarization vectors for direct incoming waves and scattered waves, respectively

(Figure 2.C1). We applied this 2-D sensitivity kernel to account for finite-frequency effects improving resolution on 2-D phase velocity (Figure 2.C2).

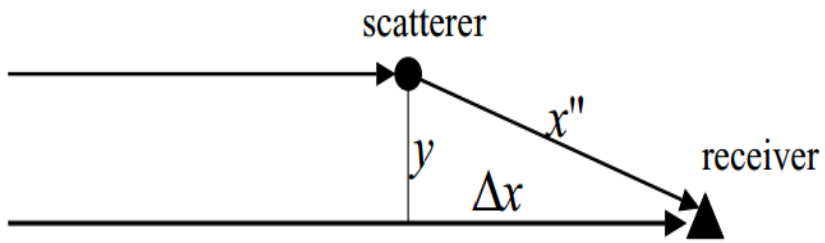

Figure 2.C1. The schematic figure of single scattering for a plane surface wave propagating from left to right [*Yang and Forsyth*, 2006]. x'' is the scatter-receiver distance; y is the perpendicular distance from the scatterer to the direct incoming ray recorded by the receiver; Δx is the differential propagating distance between the direct incoming wave arrived at the receiver and that arrived at the scatterer.

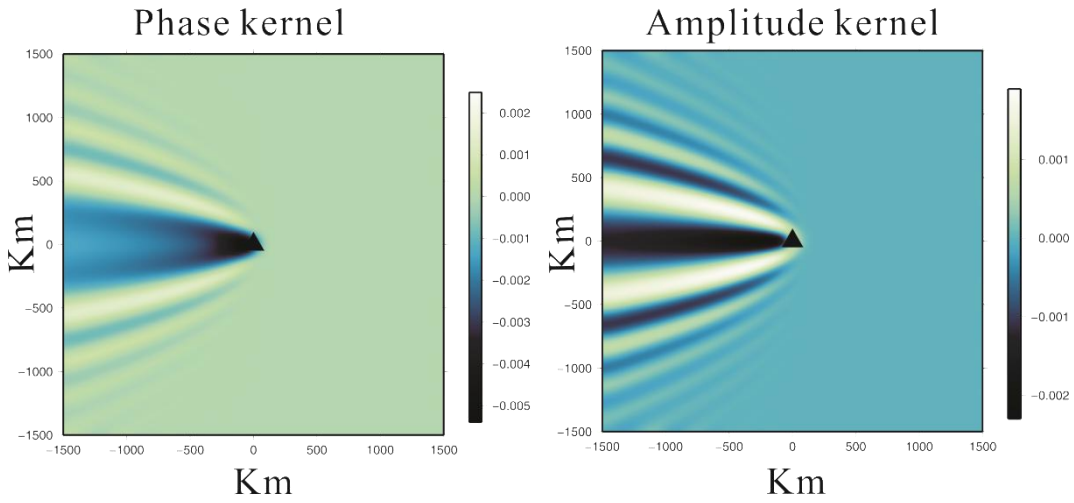

Figure 2.C2. Maps of 2-D sensitivity kernels at surface for a 50 s plane Rayleigh wave. The kernels are smoothed with a Gaussian smoothing length of 80 km. Black triangles denote receivers.

Appendix 2.D Resolution Tests for the Low Velocity Anomaly Beneath the Restraining Bend of the Kunlun Fault

We conducted additional resolution tests on three models to address whether the low velocity anomaly is a local feature or a simple extension of the large-scale slow anomaly in Tibet. The results of these tests are shown in Figure 2.D1, 2.D2, and 2.D3. The tests show that this anomaly might connect to the large scale anomaly but it need to be additionally stronger in order to be consistently observed at all periods. Without the additional strength, a localized slow anomaly is not always present at the restraining bend of the Kunlun fault.

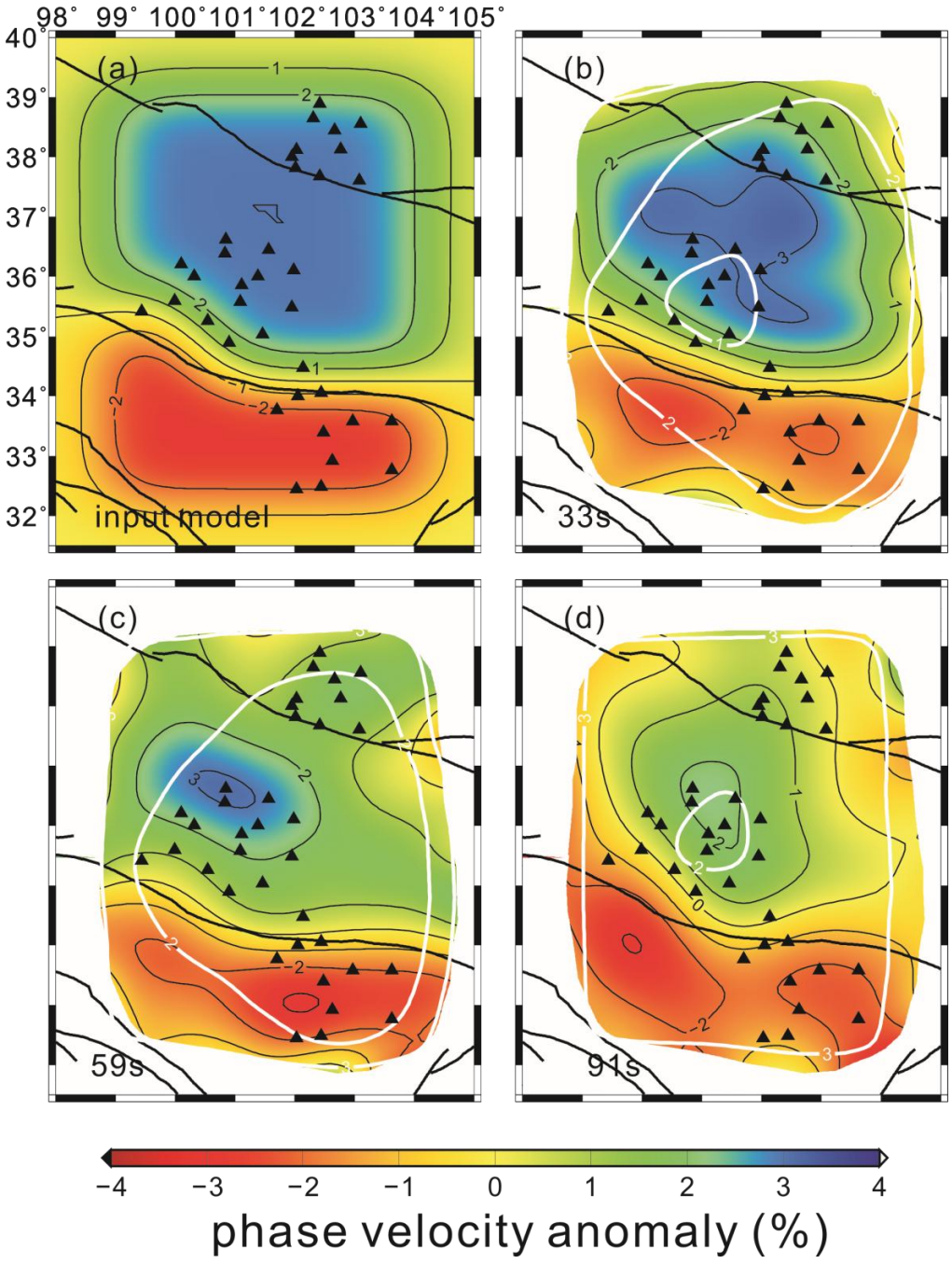

Figure 2.D1. Input and recovered phase velocity models (a) The input model with anomalies separated by the Kunlun fault. (b-d) Recovered models at periods of 33, 59 and 91 s. White lines denote contours of 2σ on phase velocity perturbation at corresponding periods. Thin black lines are contours of phase velocity anomaly.

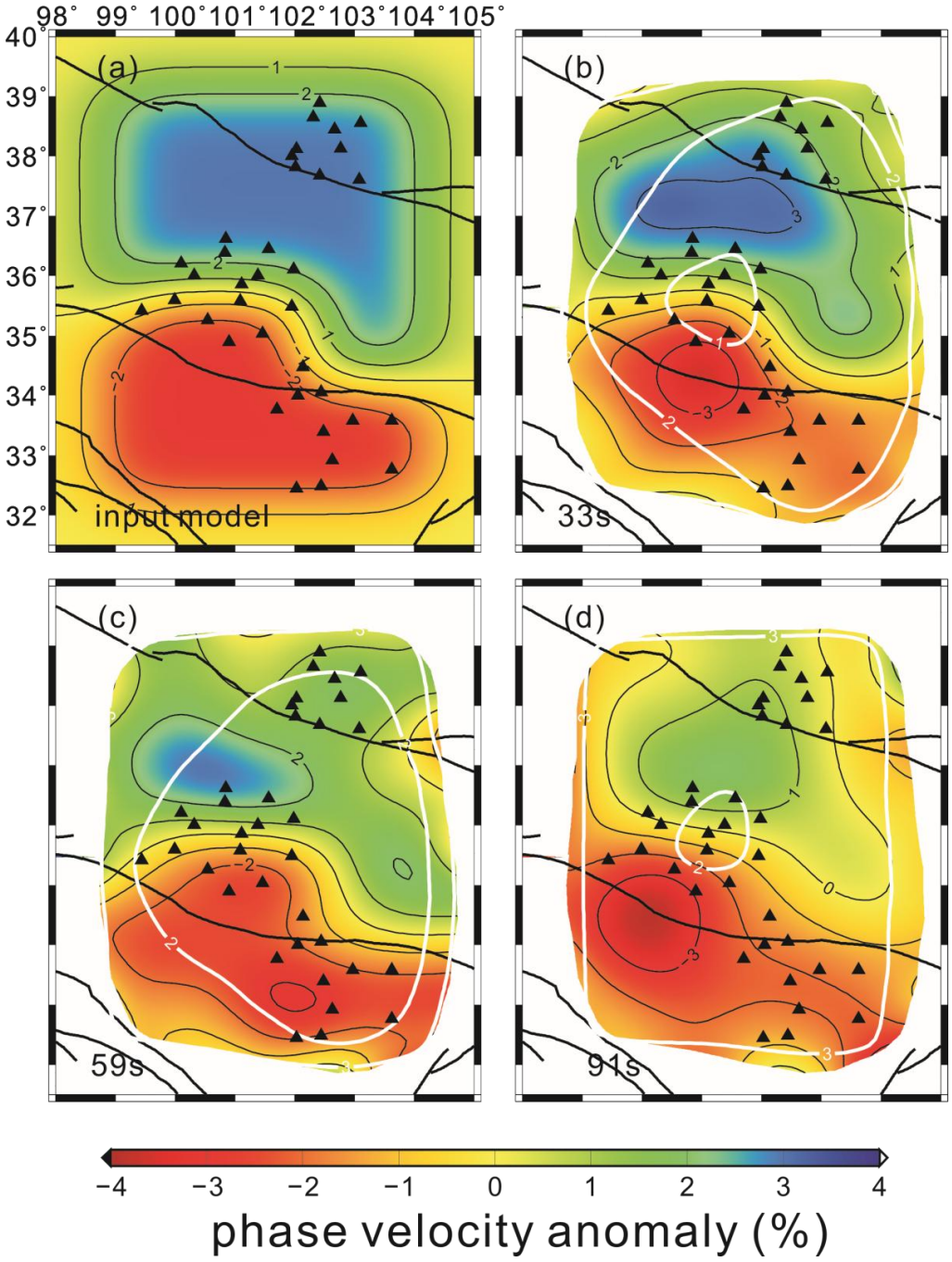

Figure 2.D2. Input and recovered phase velocity models. (a) The input model with the slow anomaly extending across the Kunlun at the restraining bend. (b-d) Recovered models at periods of 33, 59 and 91 s.

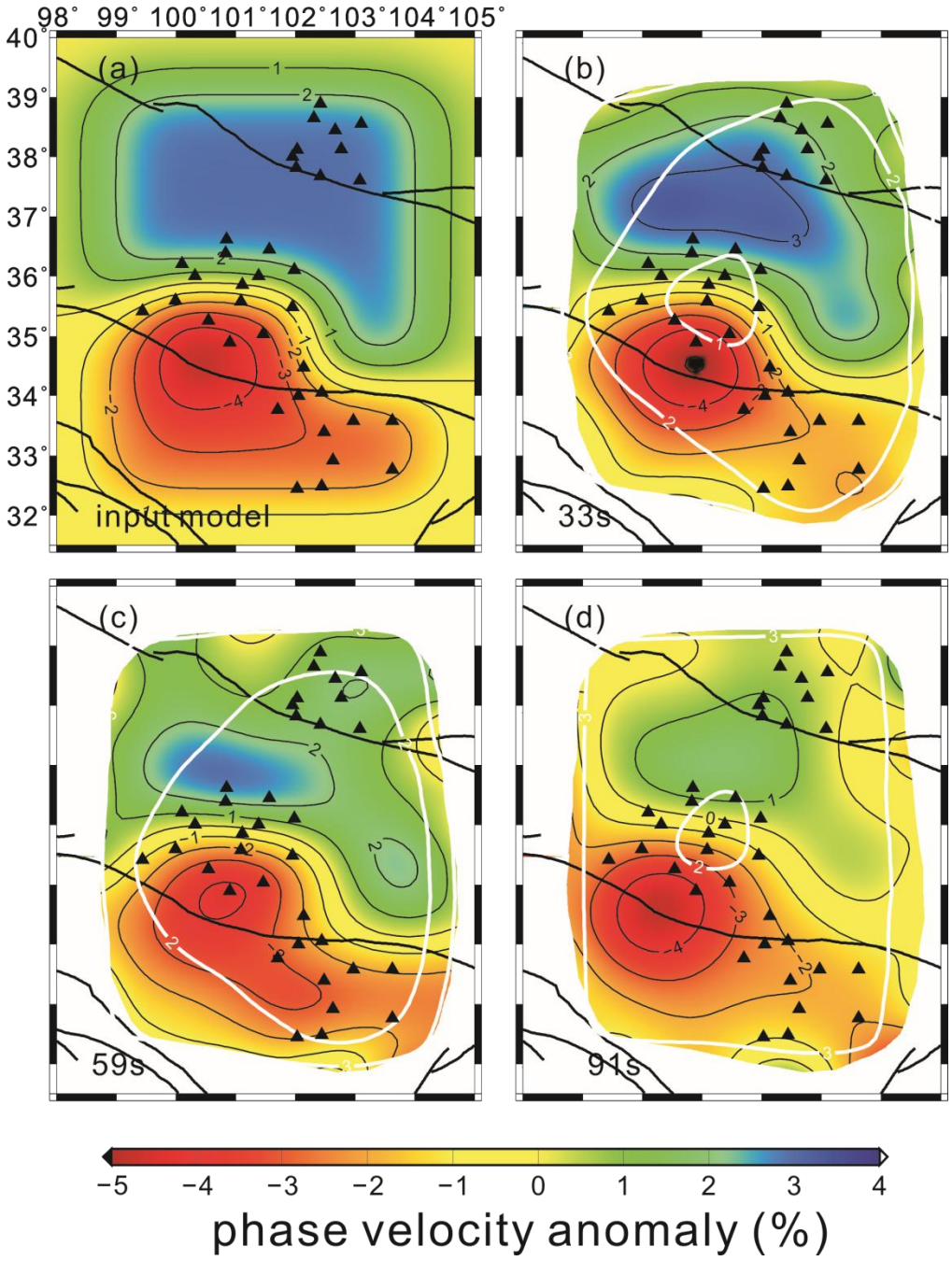

Figure 2.D3. Input and recovered phase velocity models. (a) The input model with -5% anomaly at the bend of the Kunlun fault. (b-d) Recovered models at periods of 33, 59 and 91 s.

2.9. Acknowledgements

We thank David Abt and Yonghua Li for helpful comments on the early versions of this manuscript. Suggestions from Mike Murphy help to improve the discussion section. Seismic data used in this study were obtained from the Incorporated Research Institution for Seismology Data Management Center. We thank the participants in Northeast Tibet Seismic (NETS) network for collecting the data. Figure 2.1, 2.3, 2.5, 2.6, 2.8 and 2.9 in this paper were made with the Generic Mapping Tools [*Wessel and Smith*, 1998]. We appreciate constructive suggestions and comments from anonymous reviewers and Editor Robert Nowack. This study is supported by NSF grant EAR-0738879, the funding of Ministry of Science and Technology of China (2006DFA21350), and Chinese Geological Survey (1212010511809).

2.10. References

An, M. J. and Shi, Y.L. (2006), Lithospheric thickness of the Chinese continent. *Phys. Earth* Planet. In., 159, 257–266. doi:10.1016/j.pepi.2006.08.002.

Arnaud, N. O., P. Vidal, P. Tapponnier, P. Matte, and W. M. Deng (1992), The High K2O volcanism of northwestern Tibet-Geochemistry and tectonic implications, Earth Planet. Sci. Lett., 111, 351–367, doi:10.1016/0012-821X (92)90189-3.

Bai, D., et al. (2010), Crustal deformation of the eastern Tibetan Plateau revealed by magnetotelluric imaging, Nat. Geosci., 3, 358-362, doi:10.1038/ngeo830.

Brown, L. D., W. Zhao, K. D. Nelson, M. Hauck, D. Alsdorf, A. Ross, M. Cogan, M. Clark, Xianwen Liu, and J. Che, (1996). Bright Spots, Structure and Magmatism

in Southern Tibet from INDEPTH Seismic Reflection Profiling, *Science*, 274, 1688-1690.

Chen, L., Booker, J.R., Jones, A.G., Wu, N., Unsworth, M.J., Wei, W., and Tan, H. (1996). Electrically conductive crust in southern Tibet from INDEPTH magnetotelluric surveying. *Science* 274, 1694–1696.

Chen, Y., J. Badal and J. Hu (2010), Love and Rayleigh Wave Tomography of the Qinghai-Tibet Plateau and Surrounding Areas, *Pure Appl. Geophys*. 167 (), 1171–1203. DOI 10.1007/s00024-009-0040-1.

Chen, Z., B. C. Burchfiel, Y. Liu, R. W. King, L. H. Royden, W. Tang. E. Wang, J. Zhao, and X. Zhang (2000), GPS measurements from eastern Tibet and their implications for India/Eurasia intracontinental deformation, *J. Geophys. Res.*, 105, 16,215–16, 22.

Chung, S., M. Chu, Y. Zhang, Y. Xie, C. Lo, T. Lee, C. Lan, X. Li, Q. Zhang, and Y. Wang (2005), Tibetan tectonic evolution inferred from spatial and temporal variations in post-collisional magmatism, *Earth Sci. Rev.*, 68, 173¨C196, doi:10.1016/j.earscirev.2004.05.001.

Clark, M., and Royden, L. (2000), Topographic ooze: building the eastern margin of Tibet by lower crustal flow. *Geology*, 28, 703–706.

Clark, M., Bush, J., and Royden, L. (2005), Dynamic topography produced by lower crustal flow against rheological strength heterogeneities bordering the Tibetan Plateau , *Geophys. J. Int.*, 162, 575–590.

Dewey, J. F., Helman, M. L., Knott, S. D., Turco, E., & Hutton, D. H. W. (1989), Kinematics of the western Mediterranean. Geological Society, London, Special *Publications*, *45*(1), 265-283.

Du Y., Sandvol E., Shi D., Yue H., Li A., Li X., Li H., and Shen Y. (2011), S-wave Receiver function study in Northeast Tibet and adjacent boundaries: *American Geophysical Union*, Fall Meeting 2011, abstract #S31E-2282.

Elkins-Tanton, L. T. (2007), Continental magmatism, volatile recycling, and a heterogeneous mantle caused by lithospheric gravitational instabilities, *J. Geophys. Res.*, 112, B03405, doi:10.1029/2005JB004072.

Elkins-Tanton, L.T. (2005), Continental magmatism caused by lithospheric delamination, in Foulger, G.R., Natland, J.H., Presnall, D.C., and Anderson, D.L., eds., Plates, plumes, and paradigms: *Geological Society of America Special Paper* 388, p. 449–461, doi: 10.1130/2005.2388(27).

England, P. C., and G. A. Houseman (1989), Extension during continental convergence, with application to the Tibetan Plateau , *J. Geophys. Res.*, 94, 17,561 –17,579.

England, P. C., and P. Molnar (1997), Active deformation of Asia: From kinematics to dynamics, *Science*, 278, 647 – 650.

Fleitout, L., and C. Froidevaux (1980), Thermal and mechanical evolution of shear zones, *J. Struct. Geol.*, 2, 159– 164.

Forsyth, D. W., and A. Li (2005), Array-analysis of two-dimensional variations in surface wave phase velocity and azimuthal anisotropy in the presence of multipathing interference., in Seismic Earth: Array Analysis of Broadband

Seismograms, *Geophys Monogr. Ser.*, vol. 187, edited by A. Levander and G. Nolet, pp. 81–97, AGU,

Forsyth, D.W., Webb, S., Dorman, L., and Shen, Y. (1998), Phase velocities of Rayleigh waves in the MELT experiment on the East Pacific Rise. *Science* 280, 1235–1238.

Friederich, W., E. Wielandt, and S. Stange (1994), Non-plane geometries of seismic surface wavefields and their implications for regional surface-wave tomography, *Geophys. J. Int.*, 119, 931– 948.

Fu, B. H., and Y. Awata (2007), Displacement and timing of left-lateral faulting in the Kunlun Fault Zone, northern Tibet, inferred from geologic and geomorphic features. *Journal of Asian Earth Sciences* 29, 253–265.

Fu, Y. V., A. Li, and Y. J. Chen (2010), Crustal and upper mantle structure of southeast Tibet from Rayleigh wave tomography, *J. Geophys. Res.*, 115, B12323, doi:10.1029/2009JB007160.

Galvé, A., A. Hirn, M. Jiang, J. Gallart, B. de Voogd, J. Lépine, J. Diaz, Y. Wang, and H. Qian (2002), Modes of raising northeastern Tibet probed by explosion seismology, *Earth Planet. Sci. Lett.*, 203, 35–43, doi:10.1016/S0012-821X(02)00863-4.

Guo, Z., Wilson, M., Liu, J., Mao, Q. (2006), Post-collisional, potassic and ultrapotassic magmatism of the northern Tibetan Plateau : constraints on characteristics of the mantle source, geodynamic setting and uplift mechanisms. *J. Petrol*. 47, 1177–1220.

Harkins, N., Kirby, E., Shi, X., Wang, E., Burbank, D., and Chun, F., (2010). Millennial slip rates along the eastern Kunlun fault: Implications for the dynamics of intracontinental deformation in Asia: *Lithosphere*, v. 2, no. 4, p. 247–266, doi: 10.1130/L85.1.

Harrison, T.M., Copeland, P., Kidd, W.S.F., Yin, A. (1992), Raising Tibet. *Science* 255, 1663- 1670.

Herquel, G., and P. Tapponnier (2005), Seismic anisotropy in western Tibet, *Geophys. Res. Lett.*, 32, L17306, doi:10.1029/2005GL023561.

Herquel, G., P. Tapponnier, G. Wittlinger, Jiang Mei, and Shi Danian (1999), Teleseismic shear wave splitting and lithospheric anisotropy beneath and across the Altyn Tagh fault, *Geophys. Res. Lett.*, 26, 3225-3228.

Houseman, G. A. and Molnar, P. (1997). Gravitational (Rayleigh–Taylor) instability of a layer with non-linear viscosity and convective thinning of continental lithosphere. Geophysical Journal International 128, 125–150.

Houseman, G. and England, P. (1993), Crustal thickening versus lateral expulsion in the Indian–Asian continental collision, *J. Geophys. Res.*, 98(B7), 12233–12249.

Hu, S., L. He, and J. Wang (2000), Heat flow in the continental area of China: A new data set, *Earth Planet. Sci. Lett.*, 179, 407– 419.

Huang, J., and D. Zhao (2006), High-resolution mantle tomography of China and surrounding regions, *J. Geophys. Res.*, 111, B09305,

Jolivet, M., Brunel, M., Seward, D., Xu, Z., Yang, J., Malavieille, J., Roger, F., Lereloup, A., Arnaud, N., Wu, C. (2003). Neogene extension and volcanism in the

Kunlun Fault Zone, northern Tibet: new constraints on the age of the Kunlun Fault. *Tectonics,* 22. doi:10.1029/2002TC001428.

Kapp, P., A. Yin, C. E. Manning, M. Murphy, T. M. Harrison, M. Spurlin, L. Ding, X.-G. Deng, and C.-M. Wu (2000), Blueschist-bearing metamorphic core complexes in the Qiangtang block reveal deep crustal structure of northern Tibet, *Geology,* 28, 19 – 22.

Kennett B.L.N., E.R. Engdahl and R. Buland (1995), Constraints on seismic velocities in the earth from travel times, *Geophys. J. Int*, 122(1), 108-124, doi:10.1111/j.1365-246X.1995.tb03540.x.

Kind, R., et al. (1996), Evidence from earthquake data for a partially molten crustal layer in southern Tibet, *Science*, 274, 1692-1694.

Kind, R., et al. (2002), Seismic images of crust and upper mantle beneath Tibet: Evidence for Eurasian plate subduction, *Science*, 298, 1219–1221.

Kirby, E., N. Harkins, E. Wang, X. Shi, C. Fan, and D. Burbank (2007), Slip rate gradients along the eastern Kunlun fault, *Tectonics*, 26, TC2010, doi:10.1029/2006TC002033.

Le Pichon, X., Fournier, M., & Jolivet, L. (1992), Kinematics, topography, shortening, and extrusion in the India-Eurasia collision. *Tectonics*, *11*(6), 1085-1098.

Leloup, P. H., T. M. Harrison, F. J. Ryerson, W. Chen, Q. Li, P. Tapponnier, and R. Lacassin (1993), Structural, petrological and thermal evolution of a Tertiary ductile strike-slip shear zone, Diancang Shan, Yunnan, *J. Geophys. Res.*, 98, 6715– 6743.

Leloup, P., N. Arnaud, R. Lacassin, J. R. Kienast, T. M. Harrison, T. Phan Trong, A. Replumaz, and P. Tapponnier (2001), New constraints on the structure, thermochronology and timing of the Ailao Shan-Red River shear zone, *J. Geophys. Res.*, 106, 6683– 6732.

Leloup, P.H., Ricard, Y., Battaglia, J., Lacassin, R. (1999), Shear heating in continental strike-slip shear zones: Model and field examples. Geophys. J. Int., 136, pp. 19-40.

Li, A. (2011), Shear wave model of southern Africa from regional Rayleigh wave tomography with 2-D sensitivity kernels. *Geophys. J. Int.*, 185, 832-844.

Li, A. and R.S. Detrick (2006), Seismic structure of Iceland from Rayleigh wave inversions and geodynamic implications, *Earth Planet. Sci. Lett.*, Vol 241, 901-912.

Li, A., and K. Burke (2006), Upper mantle structure of southern Africa from Rayleigh wave tomography, *J. Geophys. Res.*, 111, B10303, doi:10.1029/2006JB004321.

Li, A., Forsyth, D.W., Fischer, K.M. (2003), Shear velocity structure and azimuthal anisotropy beneath eastern North America from Rayleigh wave inversion. *J. Geophys. Res.*, 108 (B8), 2362. doi:10.1029/2002JB002259.

Li, C., and Van der Hilst, R.D. (2010), Structure of the upper mantle and transition zone beneath South East Asia from travel time tomography, *J. Geophys. Res.*, vol. 115, B07308, doi:10.1029/2009JB006882.

Li, Y., Q. Wu, F. Zhang, Q. Feng, and R. Zhang (2011), Seismic anisotropy of the northeastern Tibetan Plateau from shear wave splitting analysis, *Earth Planet. Sci. Lett.*, 304, 147–157, doi:10.1016/j.epsl.2011.01.026.

Liang, C., and X. Song (2006), A low velocity belt beneath northern and eastern Tibetan Plateau from Pn tomography, *Geophys. Res. Lett.*, 33, L22306, doi:10.1029/2006GL027926.

Lin, A., B. Fu, J. Guo, Q. Zeng, G. Dang, W. He, and Y. Zhao (2002), Coseismic strike-slip and rupture length produced by the 2001 Ms 8.1 central Kunlun earthquake, *Science* 296, 2015–2017.

Liu, M., W. Mooney, S. Li, N. Okaya, and S. Detweiler (2006), Crustal structure of the northeastern margin of the Tibetan Plateau from the Songpan-Ganzi terrane to the Ordos Basin, *Tectonophysics*, 420, 253–266, doi:10.1016/j.tecto.2006.01.025.

McNamara DE, Owens TJ, Silver PG, Wu FT. (1994), Shear wave anisotropy beneath the Tibetan Plateau . *J. Geophys. Res.*, 99: 13655-65

McNamara DE, Walter WR, Owens TJ, Ammon CJ. (1997), Upper mantle velocity structure beneath the Tibetan Plateau from Pn travel time tomography, *J. Geophys. Res.,* 102: 493-505

Mitchell, B. J. (1995), Anelastic structure and evolution of the continental crust and upper mantle from seismic surface wave attenuation, *Rev. Geophys.*, 33(4), 441–462, doi:10.1029/95RG02074.

Molnar, P., and J. M. Stock (2009), Slowing of India's convergence with Eurasia since 20 Ma and its implications for Tibetan mantle dynamics, *Tectonics*, 28, TC3001, doi:10.1029/2008TC002271.

Molnar, P., and Tapponnier, P. (1975), Cenozoic tectonics of Asia: effects of a continental collision. *Science*, 189, 419–426.

Molnar, P., Fitch, T. J. & Wu, F. T (1973), Fault plane solutions of shallow earthquakes and contemporary tectonics in Asia. *Earth Planet. Sci. Lett.*, 19, 101–112.

Nataf, H., and Y. Richard (1996), 3SMAC: an a priori tomographic model of the upper mantle based on geophysical modeling, *Phys. Earth Planet. Int.*, 95(1-2), 101- 122, doi:10.1016/0031-9201(95)03105-7.

Obrebski, M., R. M. Allen, F. Zhang, J. Pan, Q. Wu, and S.-H. Hung (2012), Shear wave tomography of China using joint inversion of body and surface wave constraints, *J. Geophys. Res.*, 117, B01311, doi:10.1029/2011JB008349

Owens, T.J., Zandt G. (1997), Implications of crustal property variations for models of Tibetan Plateau evolution. *Nature* 387: 37-43.

Pan, S., and F. Niu (2011), Large contrasts in crustal structure and composition between the Ordos plateau and the NE Tibetan Plateau from receiver function analysis, *Earth Planet. Sci. Lett.*, 303, 291-298, doi:10.1016/j.epsl.2011.01.007.

Patriat, P., and J. Achache (1984), India-Eurasia collision chronology has implications for crustal shortening and driving mechanism of plates, *Nature*, 311, 615 – 621.

Pei, S.P., Zhao, J.M., Sun, Y.S., Xu, Z.H.,Wang, S.Y., Liu, H.B., Rowe, C.A., Toksoz, M.N., Gao, X. (2007), Upper mantle seismic velocities and anisotropy in China determined through Pn and Sn tomography, *J. Geophys. Res.*, 112, B05312. doi:10.1029/2006JB004409.

Press, W. H., S. A. Teukolsky, W. T. Vetterling, and B. P. Flannery, Numerical Recipes in FORTRAN: The Art of Scientific Computing, 2nd ed., 963 pp., Cambridge Univ. Press, New York, 1992.

Royden, L.H. (1996), Coupling and decoupling of crust and mantle in convergent orogens: implications for strain partitioning in the crust, *J. Geophys. Res.*, 101, 17 679–17 705.

Royden, L.H., Burchfiel, B.C., King, R.W., Wang, E., Chen, Z.L., Shen, F. & Liu, Y.P. (1997), Surface deformation and lower crustal flow in eastern Tibet, *Science*, 276, 788–790.

Saito, M. (1988). DISPER80: A subroutine package for the calculation of seismic normal-mode solutions. In D. Doornbos, Seismological Algorithms: Computational Methods and Computer Programs (pp. 293-319). New York: Elsevier.

Schäer, U., Z. Lian-Sheng, and P. Tapponnier (1990), Duration of strike-slip movement in large shear zones: The Red River belt, China, *Earth Planet. Sci. Lett.*, 126, 379–397.

Shen, Y., D. Shi, X. Li, E. Sandvol, A. Li, Z. Zhang , H. Li, X. Liang, X. Xu, H. Dong (2008), Initial report on the northeastern Tibetan Plateau seismic experiment and the study of the aftershocks of the May 12, 2008 Wenchuan earthquake, AGU Fall Meeting, abstract #U23B-0066.

Sherrington, H. F., G. Zandt, and A. Frederiksen (2004), Crustal fabric in the Tibetan Plateau based on waveform inversions for seismic anisotropy parameters, *J. Geophys. Res.*, 109, B02312, doi:10.1029/2002JB002345.

Takei, Y. (2000), Acoustic properties of partially molten media studied on a simple binary system with a controllable dihedral angle, J. Geophys. Res., 105(B7), 16,665–16,682, doi:10.1029/2000JB900124.

Tapponnier, P., Xu, Z., Roger, F., Meyer, B., Arnaud, N., Wittlinger, G., et al. (2001), Oblique stepwise rise and growth of the Tibet Plateau. *Science*, 294, 1671–1677.

Tarantola, A., and Valette, B. (1982), Generalized nonlinear inverse problem solved using the least squares criterion. *Rev. Geophys. Space Phys.*, 20 (2), 219-232.

Van der Woerd J, Ryerson FJ, Tapponnier P, Gaudemer Y, Finkel R, et al. (1998), Holo-cene left-slip rate determined by cosmo-genic surface dating on the Xidatan segment of the Kunlun fault (Qinghai, China). *Geology* 26: 695-98

Van der Woerd, J., A. S. Meriaux, Y. Klinger, F. J. Ryerson, Y. Gaudemer, and P. Tapponnier (2002), The 14 November 2001, Mw 7.8 Kokoxili earthquake in northern Tibet (Qinghai Province, China), *Seism. Res. Lett.* 73, no. 2, 125–135.

Vergne, J., G. Wittlinger, Q. Hui, P. Tapponnier, G. Poupinet, J. Mei, G. Herquel, and A. Paul (2002), Seismic evidence for stepwise thickening of the crust across the NE Tibetan Plateau, *Earth Planet. Sci. Lett*., 203, 25–33, doi:10.1016/S0012-821X(02)00853-1.

Wang, C., Gao, R., Yin, A., et al. (2011), A mid-crustal strain-transfer model for continental deformation: A new perspective from high-resolution deep seismic-reflection profiling across NE Tibet. *Earth Planet. Sci. Lett.*, 306, 279-288.

Wang, Q., Zhang, P.Z., Freymueller, J.T., Bilham, R., Larson, K.M., Lai, X., You, X.Z., Niu, Z.J., Wu, J.C., Li, Y.X., Liu, J.N., Yang, Z.Q., Chen, Q.Z. (2001).

Present-day crustal deformation in China constrained by global positioning system measurements. *Science*, 294 (5542), 574–577

Wei, W. B., et al. (2001), Detection of widespread fluids in the Tibetan crust by magnetotelluric studies, *Science*, 292, 716–719, doi:10.1126/science.1010580.

Wessel, P., and W. H. F. Smith (1998), New, improved version of generic mapping tools released, *Eos Trans*. AGU, 79(47), 579, doi:10.1029/98EO00426.

Wittlinger G, Tapponnier P, Poupinet G, Jiang M, Shi D, et al. 1998. Tomographic evi-dence for localized lithospheric shear along the Altyn Tagh fault. *Science* 282: 74-76

Yang, Y., and Forsyth, D. (2006), Regional tomographic inversion of the amplitude and phase of Rayleigh waves with 2-D sensitivity kernels. *Geophys. J. Int.*, 166, 1148-1160.

Yang, Y., et al. (2010), Rayleigh wave phase velocity maps of Tibet and the surrounding regions from ambient seismic noise tomography, *Geochem. Geophys. Geosyst.*, 11, Q08010, doi:10.1029/2010GC003119.

Yin, A., Dang, Y., Wang, L., Jiang, W., Chen, X., Gehrels, G.E., and McRivette, M.W., (2008), Cenozoic tectonic evolution of Qaidam basin and its surrounding regions (Part 1): The southern Qilian Shan-Nan Shan thrust belt and northern Qaidam basin: *Geological Society of America Bulletin*, v. 120, p. 813–846, doi:10.1130/B26180.1.

Yin, A., Harrison TN (2000), Geologic evolution of the Himalayan-Tibetan orogen. *Annu. Rev. Earth. Planet. Sci.* 28: 211-280.

Zhang, H., D. Zhao, J. Zhao, and Q. Xu (2012), Convergence of the Indian and Eurasian plates under eastern Tibet revealed by seismic tomography, *Geochem. Geophys. Geosyst.*, 13, Q06W14, doi:10.1029/2012GC004031.

Zhang, H., Teng, J., Tian, X., Zhang, Z., Gao, R., Liu, J., (2012), Lithospheric thickness and upper-mantle deformation beneath the NE Tibetan Plateau inferred from S receiver functions and SKS splitting measurements. Geophysical Journal International 191, 1285–1294. http://dx.doi.org/10.1111/j.1365-246X.2012.05667.x

Zhang, P.Z., Shen, Z., Wang, M., Gan, W.J., Burgmann, R., Molnar, P. (2004), Continuous deformation of the Tibetan Plateau from global positioning system data, *Geology* 32 (9), 809–812.

Zhang, Q., E. Sandvol, J. Ni, Y. Yang, and Y. J. Chen (2011), Rayleigh wave tomography of the northeastern margin of the Tibetan Plateau , *Earth Planet. Sci. Lett.*, 304, 103–112, doi:10.1016/j.epsl.2011.01.021.

Zhang, Z., S. Klemperer, Z. Bai, Y. Chen, and J. Teng (2011), Crustal structure of the Paleozoic Kunlun orogeny from an active-source seismic profile between Moba and Guide in east Tibet, China, *Gondwana Res.*, 19, 994–1007, doi:10.1016/j.gr.2010.09.008.

Zhou, Y., Dahlen, F. A., & Nolet, G. (2004). Three-dimensional sensitivity kernels for surface wave observables. *Geophysical Journal International*, *158*(1), 142-168.

Zhu, B., Kidd, W. S., Rowley, D. B., Currie, B. S., & Shafique, N. (2005). Age of initiation of the India-Asia collision in the east-central Himalaya. *The Journal of Geology*, *113*(3), 265-285.

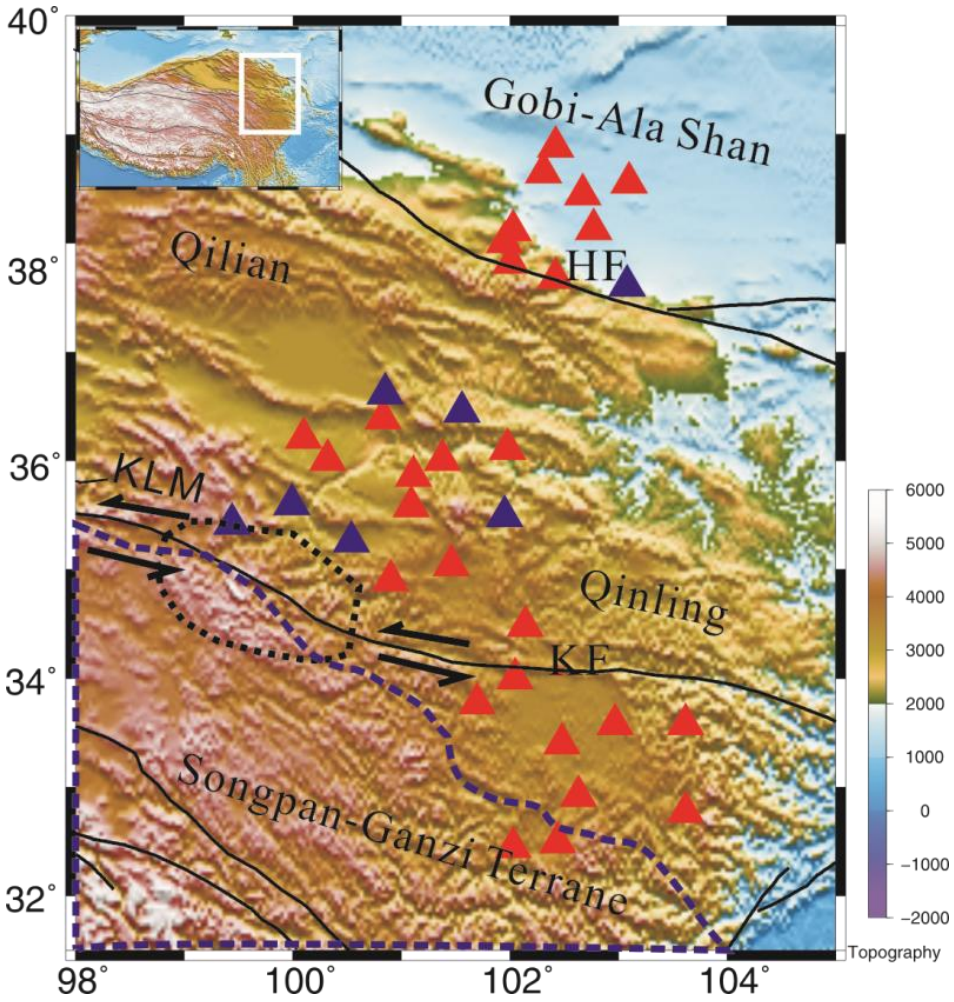

Figure 2.1. Map of seismic stations superimposed on topography in northeastern Tibet. The white box in the inset figure indicates the study area on a large scale. Red triangles and blue triangles represent the NETS stations with CMG3ESP sensors and CMG3TD sensors, respectively. The enclosed black dash line marks the restraining bend at the eastern Kunlun fault. The enclosed blue dash line approximately represents the distribution of Songpan-Ganzi flysch [*Yin and Harrison*, 2000]. KF, Kunlun fault; HF, Haiyuan fault; KLM, Kunlun Mountains.

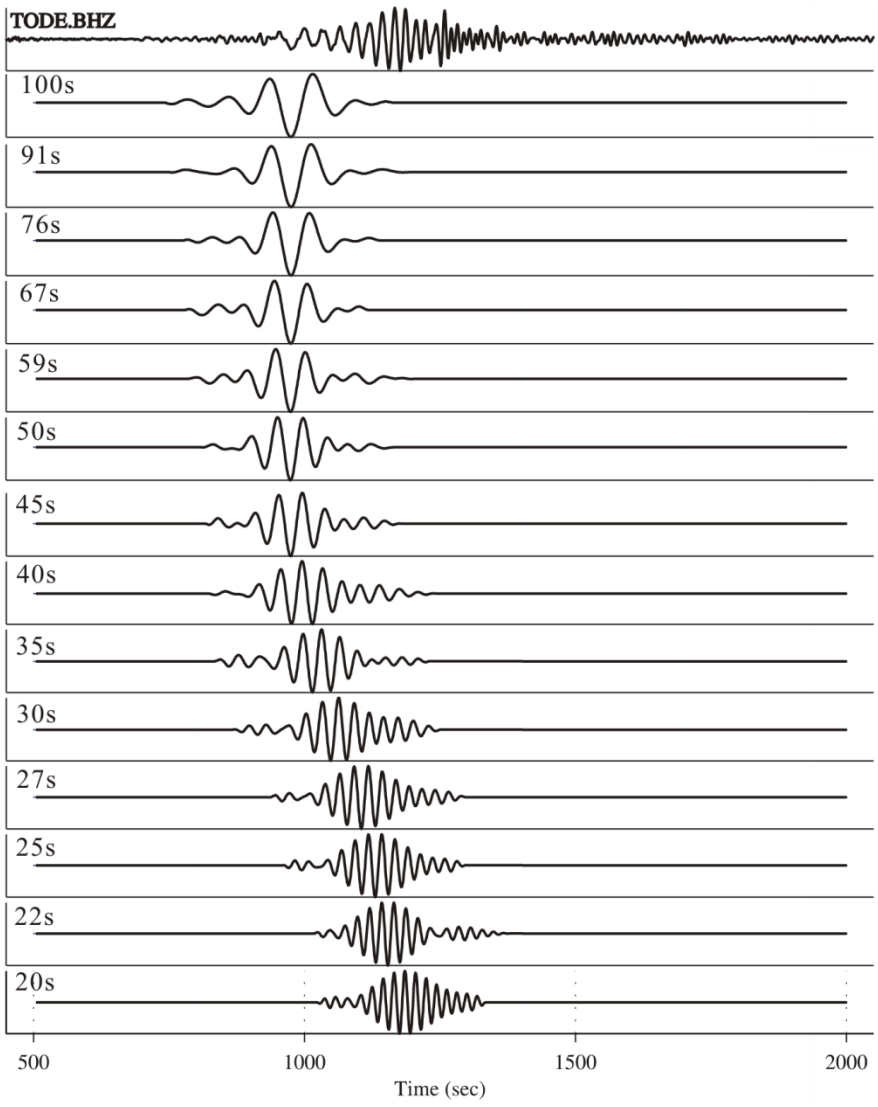

Figure 2.2. Waveforms of Rayleigh waves at station TODE from an earthquake that occurred in Japan. The waveform on the top is a broadband Rayleigh wave train, and other waveforms are filtered with a 10 mHz width filter centered at frequencies from 7 to 50 mHz. The amplitudes of Rayleigh wave at the highest frequency are almost 30 times larger than those at the lowest frequency. The waveforms are scaled to fit the frame.

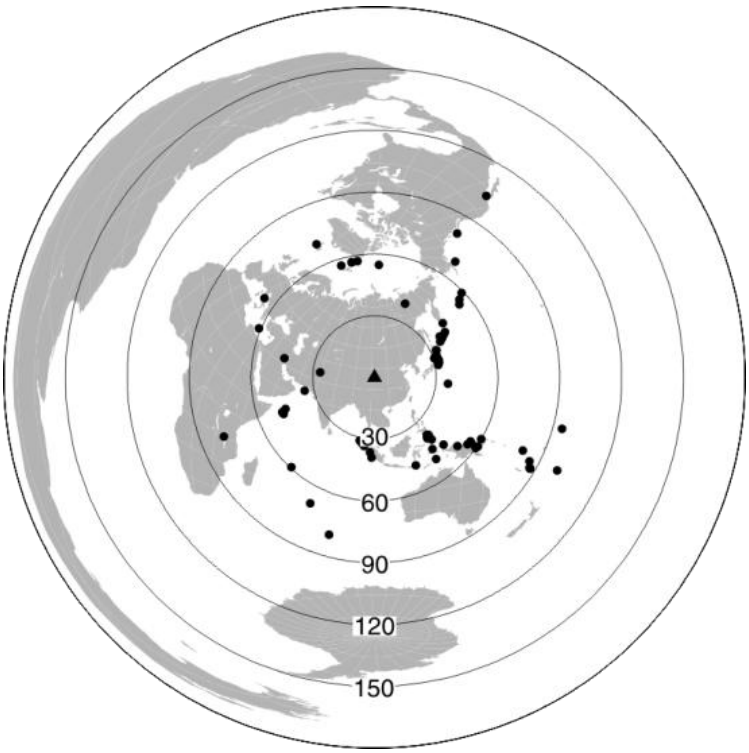

Figure 2.3. Distribution of teleseismic events (solid circles) used for Rayleigh wave tomography. Triangle denotes the center of the NETS array. Epicentral distance from the center of the seismic array is marked by large concentric circles with numbers.

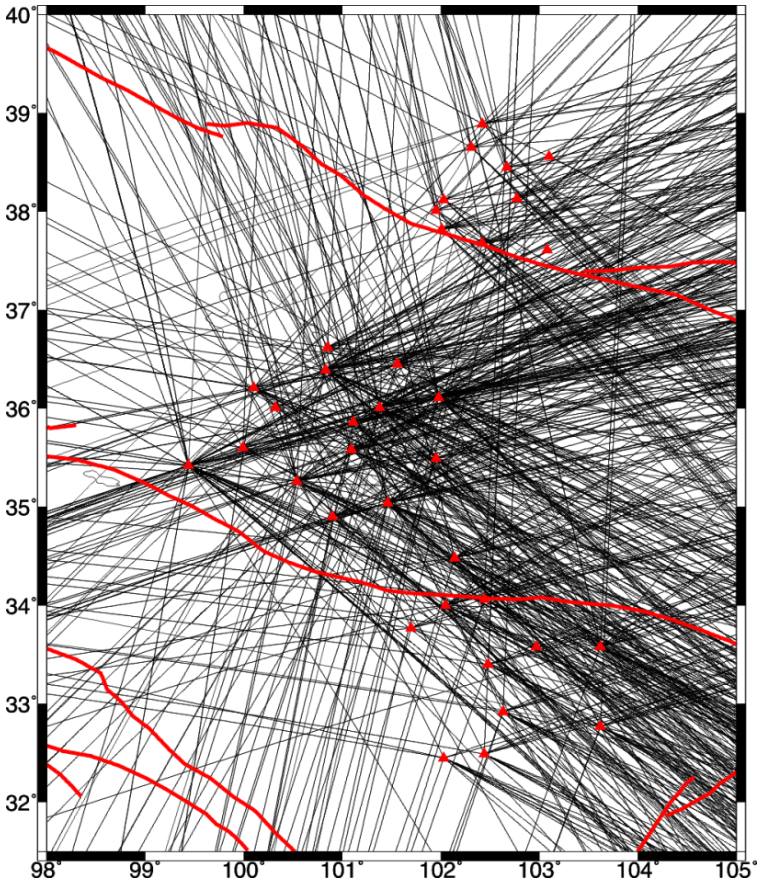

Figure 2.4. Great-circle ray paths at a period of 33 s. Red triangles represent seismic stations. The red lines represent faults.

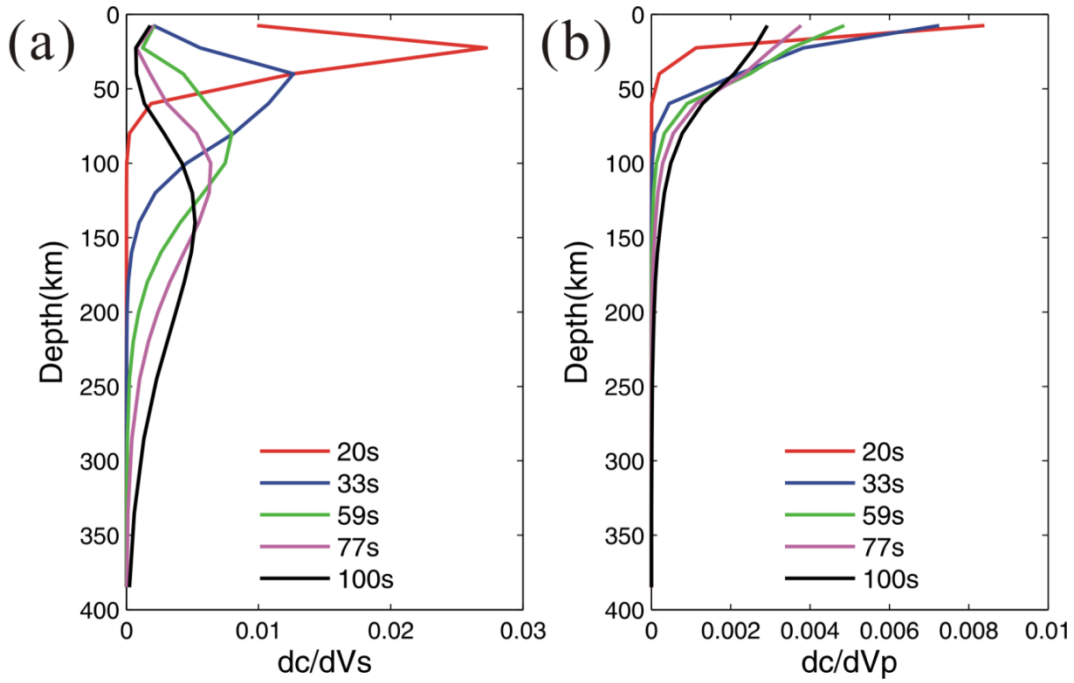

Figure 2.5. Rayleigh wave sensitivity kernels for S wave (a) and P wave (b) at periods of 20, 33, 59, 77 and 100 s based on the shear velocity model AK135 [*Kennett et al.*, 1995].

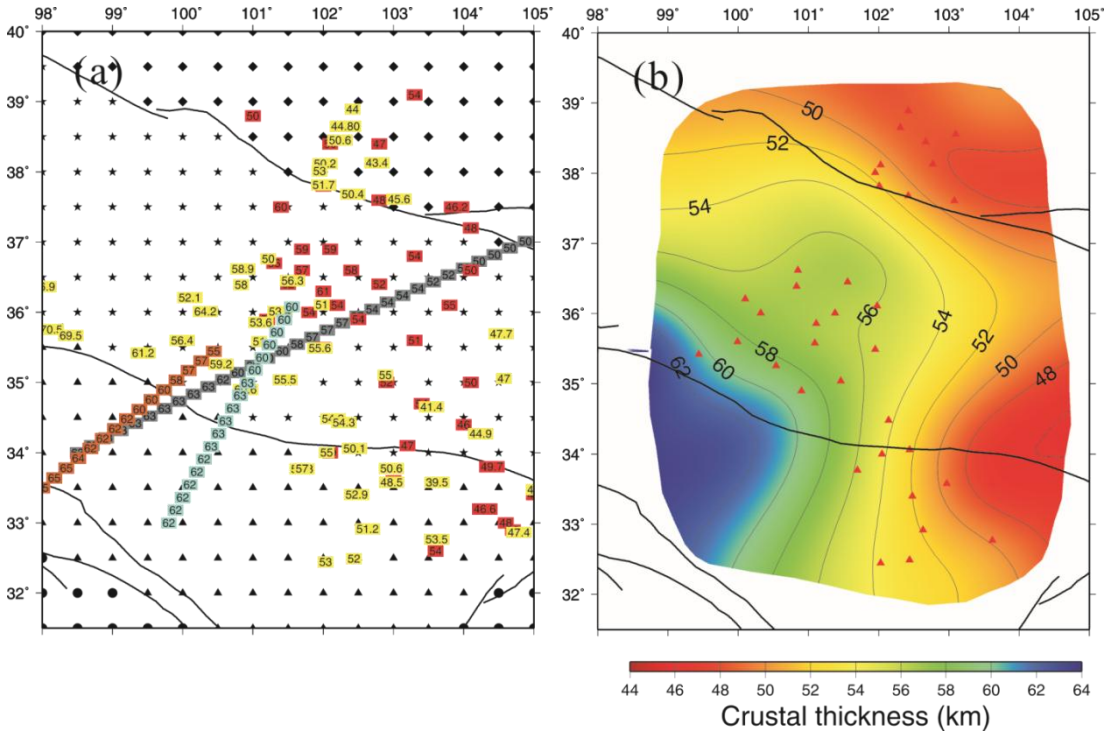

Figure 2.6. (a) Crustal thickness obtained from active source seismic profiles and receiver functions. The active source seismic profiles include the Gonghe-Yushu profile (GY) [*Galvé et al.*, 2002] marked by brown color, the Darlag-Lanzhou-Jianbian profile (DLJ) [*Liu et al.*, 2006] marked by dark gray color, and the Moba-Guide profile (MG) [*Zhang Z. et al.*, 2011] marked by light blue color. The values represent crustal thickness at corresponding locations. The yellow and red color and their corresponding values represent the crustal thickness obtained from receiver functions [*Du et al.*, 2011, *Pan and Niu*, 2011], respectively. (b) Crustal thickness map in our study area by interpolating crustal thickness values in (a).

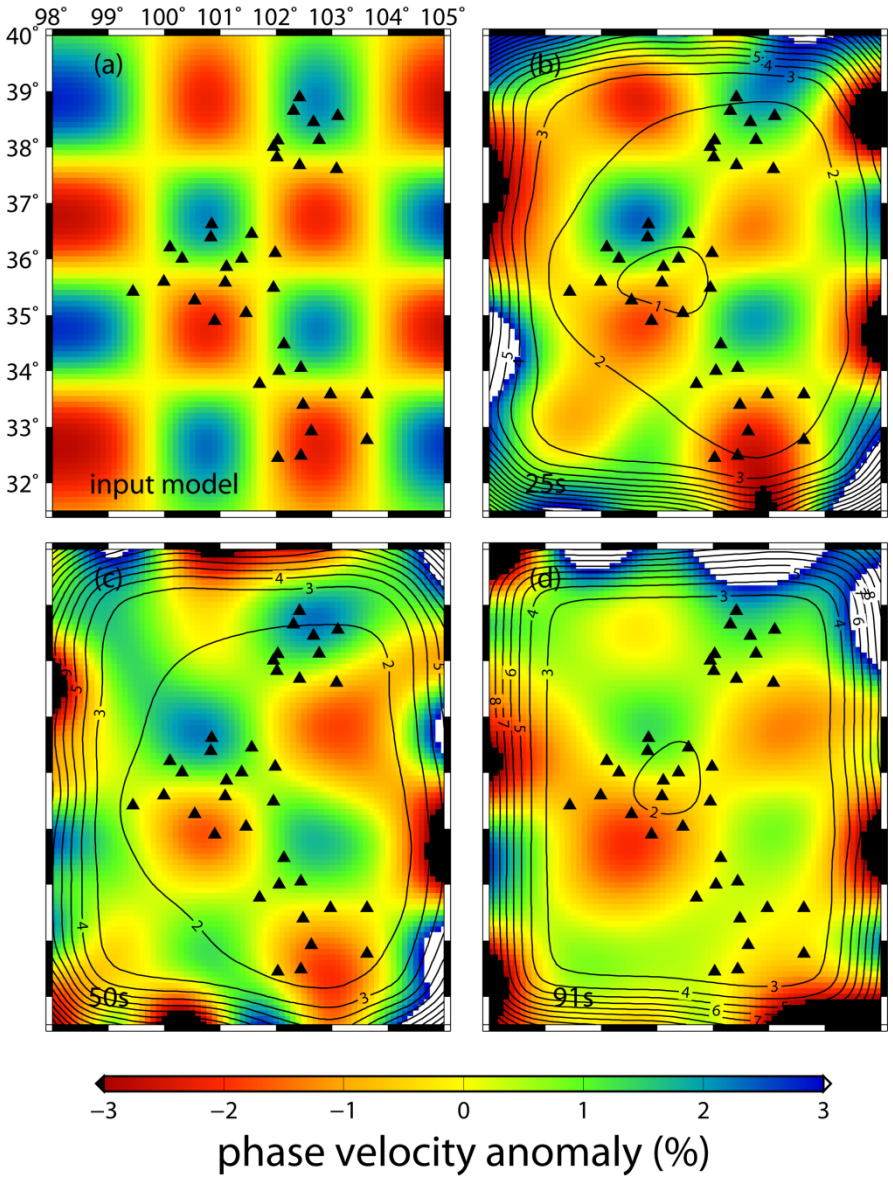

Figure 2.7. Input and recovered checkerboard models for resolution tests on Rayleigh wave phase velocities. (a) The input model with anomaly size of $1.5^{o} \times 1.5^{o}$. (b-d) Recovered models at periods of 25, 50 and 91 s. The black line denotes contour of 2σ on phase velocity perturbation at corresponding periods. Triangles denote the stations.

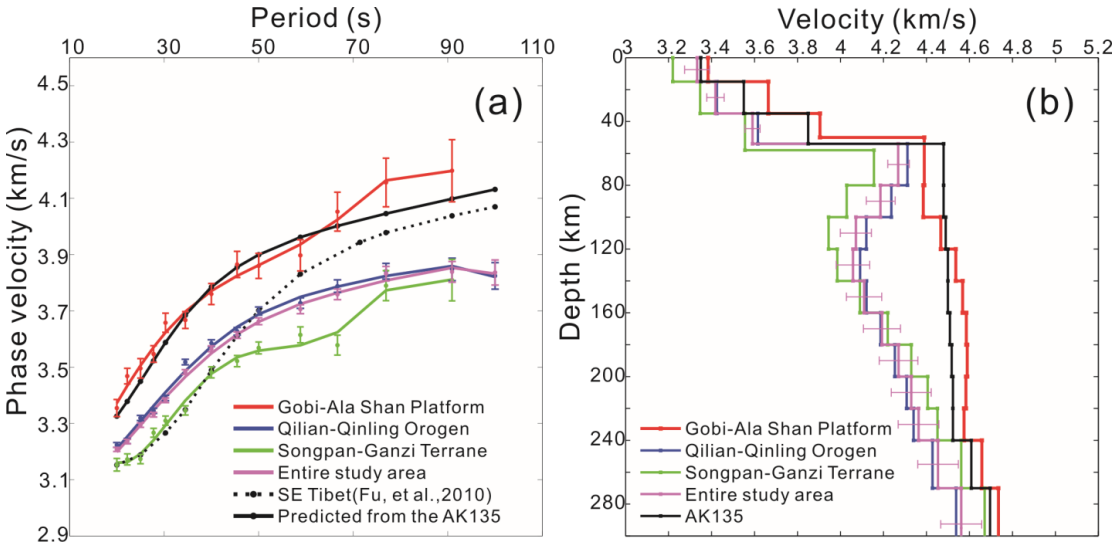

Figure 2.8. (a) Average phase velocities in northeastern Tibet (purple), southeastern Tibet [*Fu, et al.*, 2010] (dashed line), and the three sub-regions (the Gobi-Ala Shan Platform in red, the Qilian-Qinling Orogen in blue, and the Songpan-Ganzi Terrane in green) of the study area. Black line is for the predicted phase velocities from the model AK135. Lines represent the fitting curve of the data points. (b) 1-D shear wave velocities obtained by inverting the phase velocities in (a) and the AK135 model. One standard errors of shear wave velocity under the entire region are plotted at the mid-depth of each layer.

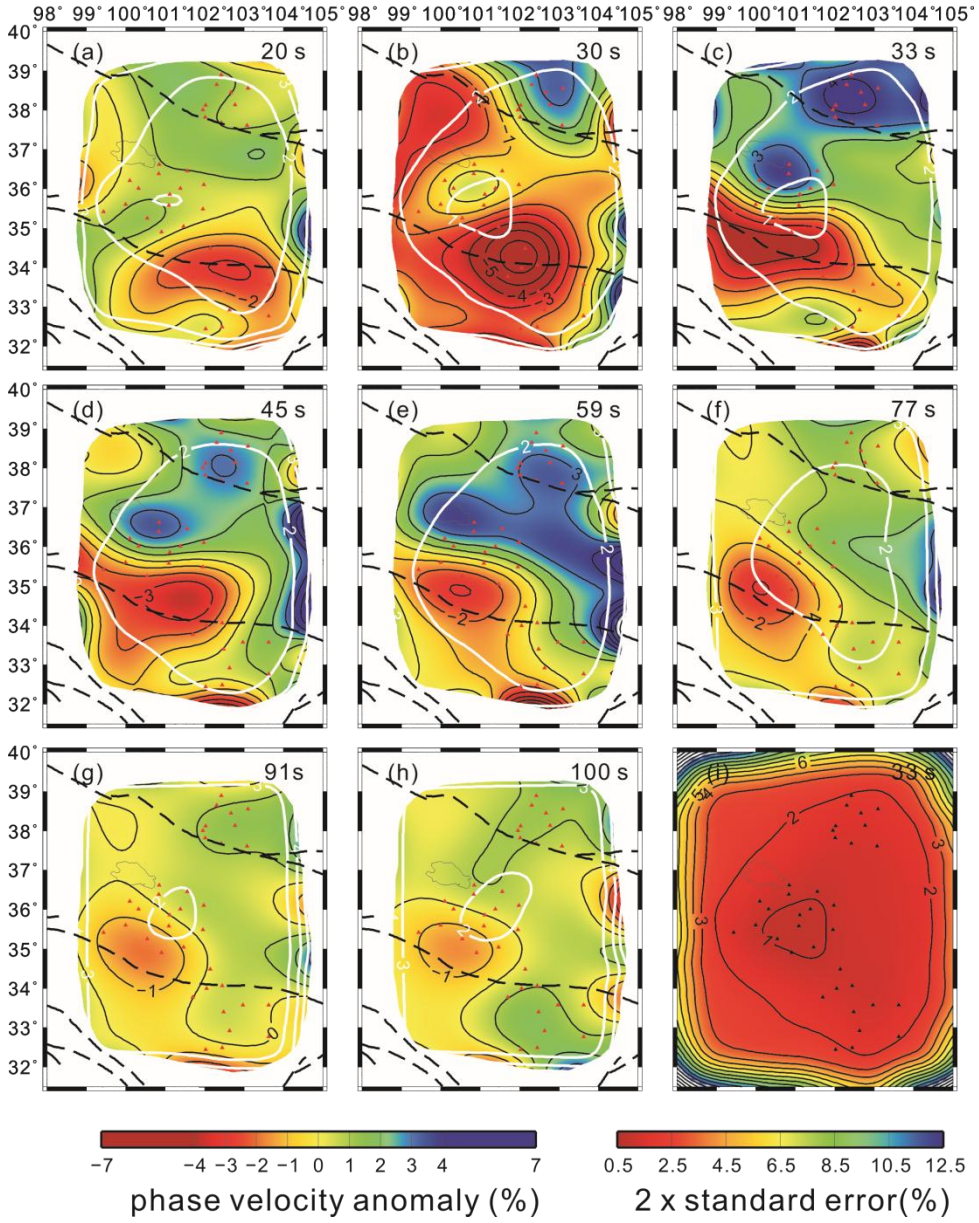

Figure 2.9. Maps of phase velocity perturbations and their standard errors. (a)-(h) Lateral variations of phase velocities at 8 periods between 20 and 100 s. The perturbations are calculated with respect to the average values (purple) in Figure 2.8a. The white lines are the contour of 2σ of phase velocity perturbation at the corresponding periods. (i) Distribution of 2σ of phase velocity perturbation at 33 s. The maps are clipped using the 3% contour in (i).

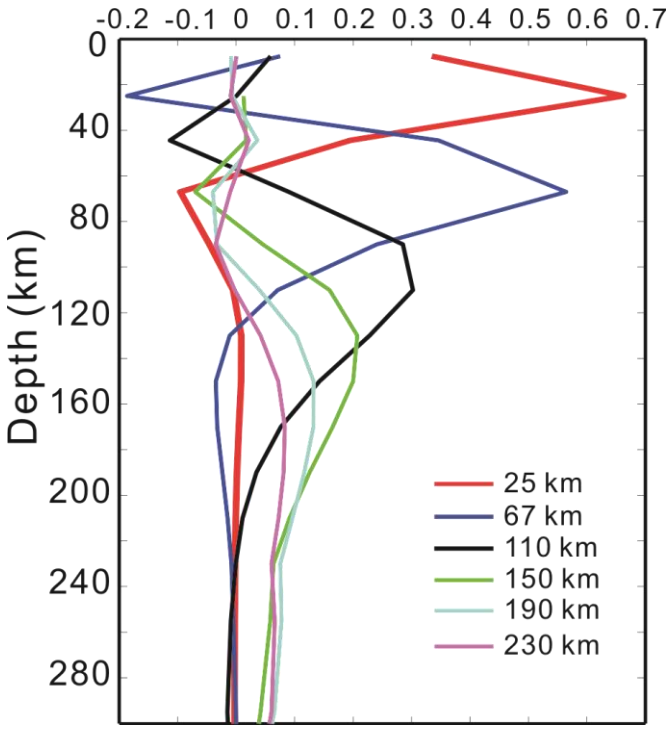

Figure 2.10. Rows of the model resolution matrix for layers at mid-depths of 25, 67, 110, 150, 190, 230 km. The resolution matrix is calculated from the inversion for the reference model.

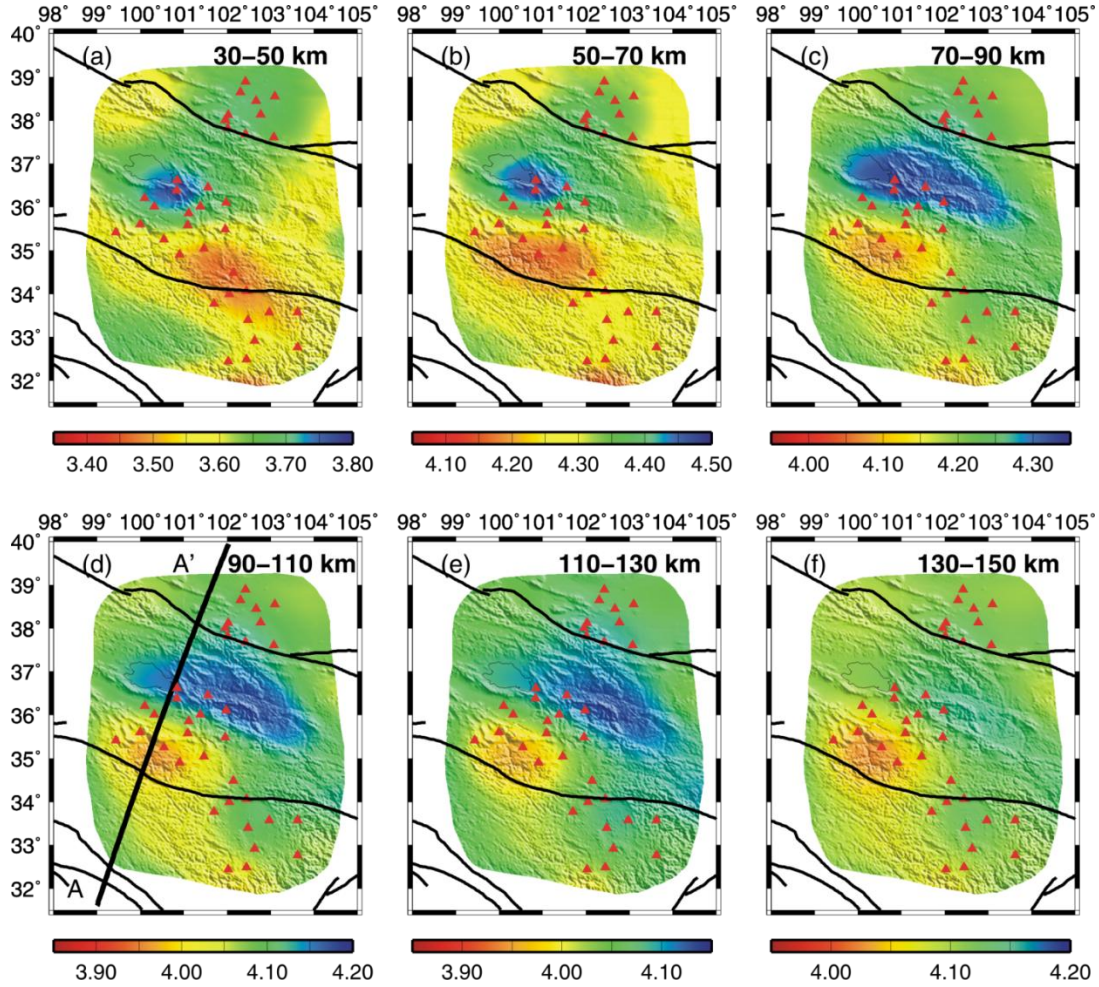

Figure 2.11. Absolute shear wave velocity maps at the depths of 30-150 km. The unit for color bars are km/s. Black line indicates the location of the cross-section shown in Figure 2.12.

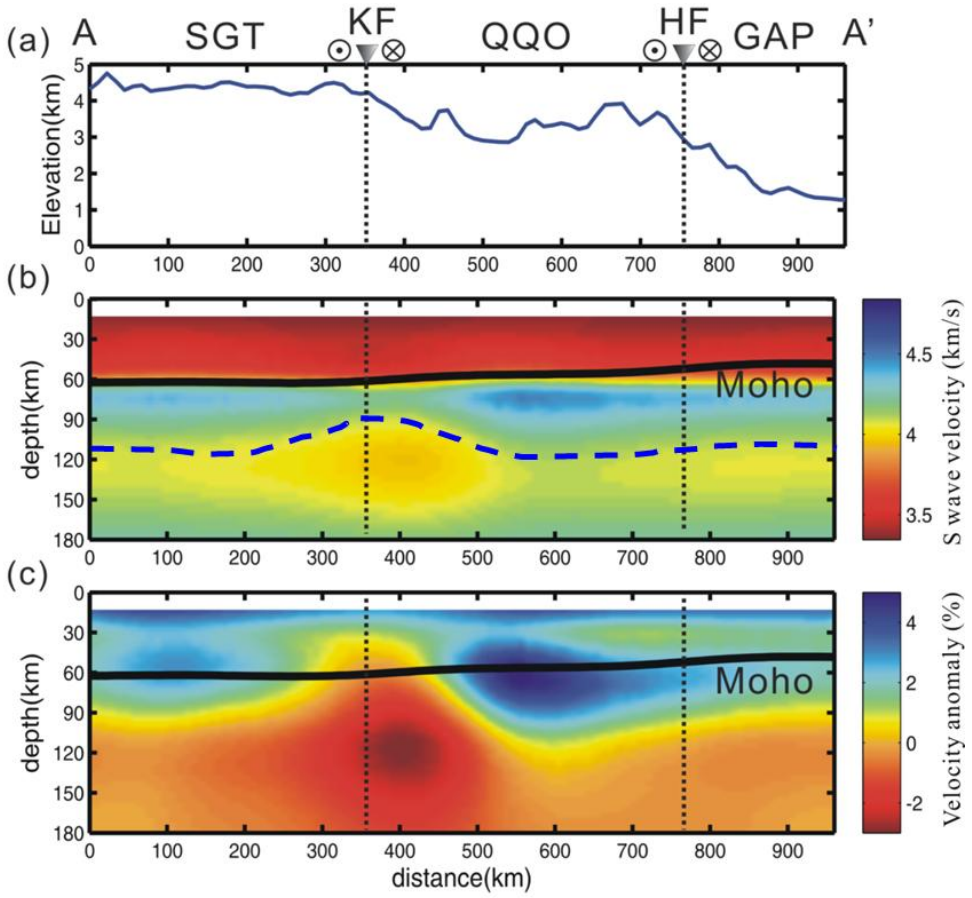

Figure 2.12. Cross-section of absolute shear wave velocity and velocity perturbation in the crust and upper mantle. The location of the cross-section is marked as a black line in Figure 2.11d. The length of cross-section is plotted in the same scale. SGT, Songpan-ganzi Terrane; QQO, Qilian-Qinling Orogen; GAP, Gobi-Ala Shan Platform; KF, Kunlun fault; HF, Haiyuan fault. (a) Topography variations along the cross-section. (b) Absolute shear wave velocity. The black line represents the Moho depth and the unit of color bar is km/s. The dash blue line represents the approximate lithosphere-asthenosphere boundary (LAB) depths. (c) Shear wave velocity perturbation. The velocity anomaly is relative to the average shear wave velocities at different depths (solid purple line) shown in Figure 2.8b. The unit of color bar is percentage.

Chapter 3. Radial Anisotropy in the Northeastern Tibetan Plateau from Surface Wave Tomography

Abstract

A three-dimensional radial anisotropic model of crust and upper mantle beneath the NE Tibetan plateau is constructed from measurements of Love wave dispersions and previously obtained Rayleigh wave dispersions in order to understand dynamic processes at the boundary of the plateau. First, the original two-plane-wave tomography (TPW) method was modified and applied to the Love wave data at 13 periods from 20 to 91 s recorded at the Northeast Tibet Seismic (NETS) array to obtain phase velocities. Then a 3-D V_{SH} model was computed from the Love wave phase velocities. The 3-D radial anisotropic model was developed using this V_{SH} model and the V_{SV} model from Rayleigh wave tomography. Similar to the V_{SV} model, a low V_{SH} anomaly appears at the Kunlun restraining bend in the crust and shallow upper mantle while a broad fast anomaly exists to the north of the Kunlun Mountain and extends across the Haiyuan fault. Negative radial anisotropy ($V_{SV}>V_{SH}$) is present in the shallow crust especially beneath high mountain belts, reflecting horizontal shortening and vertical extension. The lower crust is characterized with positive anisotropy ($V_{SH}>V_{SV}$) with large strength beneath the Qinling and Qilian orogens and relative weak values beneath the Kunlun restraining bend and its vicinity. The large positive anisotropy can be explained by horizontal alignment of anisotropic minerals such as mica at the formation of lower crust. The mantle lithosphere above 90 km is largely isotropic while weak positive anisotropy appears beneath 90 km, which

probably marks the lithosphere-asthenosphere boundary. The Kunlun restraining bend and its surrounding region are distinguished by a relatively negative radial anisotropy in the entire lithosphere, providing evidence for coherent lithosphere deformation in this area where local compression stress is high. Such coherent lithosphere deformation is not observed in the eastern portion of the Kunlun neither in the Qinling and Qilian orogens, suggesting that the magnitude of lithosphere shortening in most of the NE Tibet is not as strong as in the interiors of the plateau. These findings reflect complex deformation pattern in the NE Tibetan plateau.

3.1. Introduction

The northeastern (NE) Tibetan plateau is experiencing active mountain building and strike-slip faulting, is therefore an ideal place to study the growth of the plateau. This tectonically complex region is bounded with the mechanically strong Gobi-Alashan platform in the north, the Ordos block in the northeast, and the Sichuan Basin in southeast (Figure 3.1). The 1000 km-long left-lateral NW-SE trending Haiyuan fault defines the northern boundary of the plateau. Another major left-lateral fault, the Kunlun fault, crosses the region in the south [*Molnar and Tapponnier*, 1975; *Tapponnier and Molnar*, 1977; *Burchfiel et al.*, 1991]. The region between the Kunlun and Haiyuan faults is a wide transpressional zone [*Meyer et al.*, 1998] within which numerous smaller strike-slip faults and the Qilian, East Kunlun and West Qiling mountain ranges are present. Several models have been proposed to explain the deformation of the NE Tibetan plateau. Crustal flow was suggested to explain azimuthal anisotropy in the mid-lower crust in this region [e.g., *Li et al.*, 2011]. A

recent study suggests that a localized lithosphere drip exists beneath a restraining bend of the Kunlun fault [*Li et al.,* 2013]. However, a regional scale lithospheric delamination beneath the Songpan-Ganzi Terrane and West Qiling Orogen, instead of localized lithospheric drip, was suggested to be resulted from the east directed upper mantle flow [*Zhang et al.,* 2012]. Although a number of studies have been conducted in this region, how the deformation distributes as a function of depth remains debatable. Whether the lower crust and upper mantle are coupled or decoupled is at the center of debates.

Seismic anisotropy, which is resulted from the alignment of anisotropic minerals or lattice-preferred-orientation of olivine crystals, can allow us to investigate deformation in the lithosphere and mantle flow in the upper mantle. Seismic anisotropy in the NE Tibetan plateau has been obtained from Pn tomography [*Liang et al.,* 2004; *Pei et al.,* 2007], shear-wave splitting [*Li et al.,* 2011; *Chang et al.,* 2008] and Rayleigh wave tomography [*Zhang et al.,* 2011]. The Pn tomography results suggested an NW fast direction in the region near the restraining bend of the Kunlun fault and an E-W fast direction in the Qilian Orogen [*Liang et al.*, 2004; *Pei et al.*, 2007]. Recent shear wave splitting studies indicate fault-parallel and orogen-parallel fast direction in the vicinity of the Kunlun fault (Figure 3.1), suggesting the coherent deformation between the crust and lithospheric mantle [*Li et al.*, 2011; *Zhang et al.*, 2012]. However, azimuthal variations from Rayleigh wave phase and group velocities [*Yi et al.,* 2010] showed the presence of different anisotropic layers, indicating the existence of lower crustal flow and mechanical decoupling of the upper crust and upper mantle in NE Tibet. Additionally, *Li et al.* [2011] observed two anisotropic

layers from shear wave splitting in the wide transpressional zone between the Kunlun and Haiyuan faults (Figure 3.1). The fast direction for the upper layer in the N75-95°E range, consistent with surface movement direction, was interpreted to be related to mid-lower crustal flow [*Li et al.*, 2011]. The fast direction in the lower layer in the N105-125°E range could be associated with the current orogenesis, or asthenosphere flow. This observation is consistent with the azimuthal anisotropy from surface wave tomography, which also suggested the existence of asthenosphere flow in the West Qinling [*Zhang et al.*, 2010].

These measurements have provided some constraints on lithosphere deformation and mantle flow in NE Tibet. However, they are limited by the ambiguities between anisotropy and interface depth, and lateral resolution. For example, Pn anisotropy can provide information just below the Moho, but fail to constrain the deeper structure of the lithosphere. Anisotropy from shear wave splitting is a lack of vertical resolution; while those from Rayleigh wave tomography are limited by lateral resolution. Radial anisotropy associated with a transversely isotropic medium has not been studied in NE Tibet. It can be determined by discrepancy between Rayleigh and Love wave dispersion curves. In this study, we constructed a 3-D radial anisotropic model in NE Tibet using Rayleigh and Love wave phase velocities measured from the two-plane-wave (TPW) inversion method [*Forsyth and Li*, 2005] to investigate vertical distribution of lithosphere deformation.

3.2. **Data Analysis**

We analyzed Love wave data recorded by the Northeast Tibet Seismic (NETS) array that consisted of 36 broadband seismic stations and operated between July 2008 and July 2010 (Figure 3.1). Teleseismic events with magnitude ≥ 5.8, focal depth $\leq$ 100 km and epicentral distance between 25^{o} and 120^{o} are selected for surface wave analysis (Figure 3.2). Transverse component seismograms were filtered at 13 center frequencies (i.e., 11, 13, 15, 17, 20, 22, 25, 29, 33, 36, 40, 45 and 50 mHz) with a series of 10 mHz wide, zero-phase, 4th order Butterworth filters. Love wave waveforms are automatically windowed at all stations based on the calculated Love wave envelopes. Time window for a certain event was determined based on phase velocities at the shortest and longest periods predicted from the AK135 global model. Figure 3.3 is an example of windowed waveforms for Rayleigh wave on the vertical component and Love wave on the transverse component. After automatically windowing and filtering Love waves, we visually inspected individual waveform for its signal/noise ratio and consistence with that at nearby stations and removed the poor quality waveforms.

Love wave data generally have lower signal-noise ratios than Rayleigh waves. Therefore, fewer events and ray paths are expected for Love wave. Interference due to multipath and higher modes is much stronger at periods between 25 and 40 s than at other periods (Figure 3.4) and the useful data in this period range are significantly smaller than Rayleigh waves (Figure 3.5). Raypath number decreases from median periods to short periods and long periods (Figure 3.5 and 3.6). The ray path coverage illustrates relatively high ray path density in the east and south of the study area,

while the ray density to the west, northwest and southwest is relatively low (Figure 3.6).

Fourier analysis was applied to determine amplitude and phase of Love wave trains in different frequency bands after correcting instrument responses, filtering and windowing the records. Geometrical spreading and attenuation compensation were conducted as described by *Li et al*. [2003]. The attenuation coefficients used herein are from *Mitchell* [1995] for tectonically active regions. The amplitude and phase information from Fourier analysis are used for calculating the 1-D and 2-D Love phase velocities.

3.3. Method

We followed a two-step inversion procedure. First, one-dimensional (1-D) and two-dimensional (2-D) fundamental mode Love wave (20-91 s) phase velocities were measured using a two-plane-wave method that is similar to the method used for Rayleigh waves [*Forsyth and Li*, 2005; *Li et al.*, 2003]. The TPW method for Rayleigh wave has been extensively used in a variety of regions [e.g., *Li et al.*, 2003; *Weeraratne et al.*, 2003; *Forsyth and Li*, 2005; *Li et al.*, 2005; *Li and Detrick*, 2006; *Fu et al.*, 2010; *Chen and Li*, 2011; *Zhang et al*., 2011]. However, this method cannot be directly applied to Love waves. In this study, we modified the original algorithm and extended the TPW tomography method to Love waves to obtain 1-D and 2-D Love wave phase velocities. The two-plane-wave method for Love waves is described in details below.

3.3.1. Love Wave Tomography using the TPW Method

To represent the incoming wave with two plane waves, a local coordinate system for the TPW method is set up for each event with the origin at a reference station (Figure 3.7), where the two plane waves are in phase and their constructive interference generates the largest amplitude in the array. The x-coordinate is the distance along the great-circle path between the reference station and any point in the area. The y-coordinate of a point is defined as the distance along the perpendicular, small-circle path passing from that point to the great-circle path through the reference station (Figure 3.7b).

For a given frequency ω, the incoming wave field is considered as the interference of two plane waves represented by the following expressions in polar coordinates (r,ψ) centered on the reference station and oriented in the great-circle path [*Forsyth and Li*, 2005]. The transverse displacement is of the form

$$ {}_i^k U = {}_i A_1 \exp(-i\, {}_i^k \phi_1) + {}_i A_2 \exp(-i\, {}_i^k \phi_2) \tag{3.1} $$

where $$ {}_i^k \phi_1 = {}_i^0 \phi_1 + \overline{{}_i^k S}\omega \left\{ {}_i^k r \cos\left({}_i^k \psi - {}_i \vartheta_1 \right) - {}_i^k x \right\} + \omega({}_i^k \tau - {}_i^0 \tau) \tag{3.2} $$

and

$$ {}_i^k \phi_2 = {}_i^0 \phi_2 + \overline{{}_i^k S}\omega \left\{ {}_i^k r \cos\left({}_i^k \psi - {}_i \vartheta_2 \right) - {}_i^k x \right\} + \omega({}_i^k \tau - {}_i^0 \tau); \tag{3.3} $$

${}_i^k U$ is total displacement; ${}_i A_1$ and ${}_i A_2$ are the amplitude of the two plane waves, respectively; ${}_i^0 \phi_1$ and ${}_i^0 \phi_2$ are the phases of the two waves at the reference station; ${}_i^k \tau$ and ${}_i^0 \tau$ are the travel times along the ray path from the edge of the study area to the *k*-th and reference station; ${}_i \vartheta_1$ and ${}_i \vartheta_2$ are the angular deviations from the ray path of

the two waves; r and ψ are the distance and angle in the local polar coordinates (r, ψ), respectively. $\overline{{}_i^k S}$ is the average slowness for each ray path and is defined as

$$\overline{{}_i^k S} = [{}_i^k \tau / ({}_i^k x - {}_i x_{edge}) + {}_i^0 \tau / ({}_i^0 x - {}_i x_{edge})] / 2 \tag{3.4}$$

where τ is the integrated travel times along ray path:

$${}_i^k \tau = \int_{{}_i x_{edge}}^{{}_i^k x} {}_i S dx \tag{3.5}$$

S is the slowness at each grid point that can be written as:

$${}_i S = \frac{\sum_{j=1}^{N} \frac{{}_i w_j}{{}_i V_j}}{\sum_{j=1}^{N} {}_i w_j} \tag{3.6}$$

where N is the number of grid points, and ${}_j w_i$ is the weighted Gaussian function for the ith event at the jth grid node and can be expressed as:

$${}_i w_j = \exp[-\frac{(x - {}_i x_j)^2 + (y - {}_i y_j)^2}{L_w^2}] \tag{3.7}$$

where x and y are the location based on the coordinate system employed differently for each event, ${}_i x_j$ and ${}_i y_j$ are the location of the jth grid node in the coordinate system of the ith event. Lw represents characteristic length that controls the shape of Gaussian function and the smoothness of phase velocity map [*Li et al.,* 2003; *Li,* 2011].

In the Rayleigh wave inversion, only the vertical components are used and the amplitudes of the two plane waves can be added directly. Love wave particle motion that is on the transverse component and perpendicular to the great-circle ray path is slightly different between the reference station and other stations in the network

(Figure 3.7b). Therefore they have to be decomposed to two orthogonal components (X and Y components) for further analysis.

The amplitudes of X and Y component for Love wave at a station are approximately expressed as $A_x = A\,sin(d\phi)$ and $A_y = A\,cos(d\phi)$, where A is the amplitude of Love wave at the station and $d\phi$ is the difference in azimuth between the great-circle path to the reference station and to the interested station. Love wave amplitude for the two plane waves can be written as

$$A_{1x} = A_1 \sin\theta_1, \qquad A_{1y} = A_1 \cos\theta_1, \tag{3.8}$$

$$A_{2x} = A_2 \sin\theta_2, \qquad A_{2y} = A_2 \cos\theta_2, \tag{3.9}$$

where index 1 and 2 are for plane wave 1 and 2, respectively, A_1 or A_2 is the Love wave amplitude for each plane wave and θ_1 or θ_2 is the angle between the raypath of the plane wave and the x direction, the great-circle path to the reference station.

After decomposing Love wave particle motion in X and Y component, then the interference between the two plane waves can be calculated directly for each component. And the rest of the inversion is similar to that for Rayleigh waves [*Forsyth and Li*, 2005].

The study area was parameterized with 270 grid nodes with a spacing of 0.5 degree. we used 80 km as a characteristic length for all frequencies to smooth the phase velocity models in this study according to previous study [*Li et al.*, 2003]. Additionally, we assigned a priori error of 0.25 km/s at the inner nodes and 2.5 km/s at the edge nodes (the most outside two rows and columns), which helps to absorb anomalous phase and amplitude data that cannot be represented by the two plane waves to reduce artificial effects on phase velocities at the inside nodes. The

parameters of the two plane waves (i.e., amplitudes, phases, and propagation directions) are first estimated using a simulated annealing method (p. 444, Press et al., 1992) and subsequently solved simultaneously with phase velocities in a generalized linear inversion [*Tarantola and Valette*, 1982].

3.3.2. Shear Wave Velocity Inversion and Radial Anisotropy Calculation

We solve the inversion problem iteratively to obtain V_{SH} using a least-squares approach [*Tarantola and Valette*, 1982]. Letting $\mathbf{m_0}$ be a starting model, synthetic data are $\mathbf{d_0} = g(\mathbf{m_0})$. The solution to the general, nonlinear, least squares inversion is given by

$$\Delta m = (G^T C_{nn}^{-1} G + C_{mm}^{-1})^{-1}[G^T C_{nn}^{-1} \Delta d - C_{mm}^{-1}(m - m_0)] \tag{3.10}$$

where $\mathbf{m}$ is the current model (V_{SH}), $\Delta\mathbf{m}$ is the change to the current model, $\Delta\mathbf{d}$ is the difference between the predicted and observed data, $\mathbf{G}$ is the Fréchet derivative of the operator g, $\mathbf{C}_{nn}$ is the a *priori* data covariance matrix, and $\mathbf{C}_{mm}$ is the a *priori* model covariance matrix. Off-diagonal terms are introduced into $\mathbf{C}_{mm}$ to smooth the solution. $\mathbf{C}_{nn}$ is assumed to have only diagonal terms, which are standard errors from the inversions for Love wave phase velocities. The inversion also apply penalty for deviation from the initial model $\mathbf{m}_0$.

Model parameters that are not well constrained by the data will be close to the starting values. Love wave phase velocity Fréchet derivatives with respect to model parameters (i.e., V_{SH}) are calculated using the method of *Saito* [1988]. The partial derivatives would be updated after each iteration. The starting model is based on the AK135 model [*Kennett et al*., 1995]. We modified the crustal structure in the AK135

model to fit that in NE Tibet. The modified model consists of 3 layers in the crust with a total crustal thickness of 54 km for 1-D shear wave velocity inversion.

The shear velocity models constructed from Rayleigh waves and Love waves are referred as V_{SV} and V_{SH}, correspondingly. In this study, we inverted the Love wave phase velocity at the periods of 20~91 s into V_{SH} and then calculated radial anisotropy with previously obtained V_{SV} derived from Rayleigh wave phase velocity. The radial anisotropy is defined as the percentage difference between V_{SH} and V_{SV} in the medium: $\gamma = (V_{SH}-V_{SV})/V_S$. Vs is the isotropic or effective shear wave velocity and is computed from V_{SH} and V_{SV} via a Voigt average, $V_S = \sqrt{(2V_{SV}^2 + V_{SH}^2)/3}$ [*Babuška and Cara,* 1991].

We tested on how a priori error of model parameter V_{SH} would affect the fitting of phase velocity with the observations. Several values (0.05, 0.1, 0.15 and 0.2 km/s) for priori error of V_{SH} were tested and the velocity models and associated prediction of phase velocities are shown in Figure 3.8. All the models can fit the phase velocity data equally well. However, for the standard error of 0.15 and 0.2 km/s, velocities below 250 km that are not well constrained by the data are not convergent to the starting model, indicating the priori errors are too big. For the value of 0.05 km/s, V_{SH} is not much different from the starting model. A *priori* standard error of 0.1 km/s allows V_{SH} deviate from the initial model where the data have constraints and stay close to the initial model at great depths. The results below are obtained using a *priori* standard error of 0.1 km/s for both V_{SV} and V_{SH} 1-D and 3-D inversions. We first obtained the 1-D anisotropic model for the entire region and applied the inversion to each grid point repeatedly to generate the 3-D V_{SH} model in the NE

Tibetan Plateau. And then a 3-D radial anisotropy model is constructed from V_{SH} and previously obtained V_{SV} derived from Rayleigh wave phase velocity.

Surface waves at different periods are sensitive to the Earth's structure at different depths. Figure 3.9 shows the sensitivity kernels of Rayleigh and Love waves to V_{SV} and V_{SH} at various periods. At a given period, fundamental model Rayleigh wave phase velocity is primarily sensitive to V_{SV} at a broad depth range with a peak sensitivity at 1/3 of the wavelength (Figure 3.9a), while Love wave phase velocity is primarily sensitive to V_{SH} at relatively shallower depths (Figure 3.9b). In this study, the longest periods for Rayleigh wave and Love wave are 100 s and 91 s, respectively, both of which have reasonable sensitivity up to 130 km depth. Similarly, the model resolution matrixes for the V_{SV} and V_{SH} inversion (Figure 3.10) show the largest values are along the diagonal and the values decrease with increasing depth, indicating reduced vertical resolution at depth. Although the diagonal values are all less than 1 in the resolution matrixes, indicating that shear wave velocity in each layer cannot be independently resolved, the sum of adjacent peak values in the lower crust and shallow upper mantle can reach 1, suggesting the average velocity in these layers can be well determined. Despite reduced sharpness, the peaking values of the resolution matrixes can still be clearly recognized at 130 km for V_{SV} and V_{SH}, indicating reasonable resolution at this depth. We therefore interpret the top 130 km in the radial anisotropy model for crust and mantle structure beneath the NE Tibet.

3.4. Result

3.4.1. Tests on Phase Velocity Inversion using Amplitude in Both X and Y Components, and using Amplitude in Y Component

The amplitude of Love wave in Y component is 10-20 times larger than that in X component (Figure 3.11). Figure 3.11 shows the histogram of ratios of amplitudes in the Y component to those in the X component at the period of 40 s. The amplitudes in the X and Y components were calculated using equations (3.8) and (3.9), respectively. We compared the 2-D Love wave phase velocity maps using amplitude in the X and Y components, and using amplitude only in the Y component, in order to determine which one is more stable and can be used to determine a reliable 2-D phase velocity map. The predicted amplitude and phase in the X and Y components were obtained to fit the observed amplitude and phase in these two components. Figure 3.12 illustrates comparisons of predicted and observed Love wave amplitudes and phases in the X and Y components at the period of 40 s. Those amplitude variations in the Y components are well-resolved and the observed and predicted phases are well-fit. Weaker signals in the X components make it difficult to fit by the two plane waves, which are largely determined by the Y component data. While compared to largest amplitude in a event, the predicted amplitude in the X components can still well fit the observed ones (Figure 3.12a). Therefore, the overall small rms phase variations are expected in the phase velocity inversion.

Figure 3.13 shows the 2-D Love wave phase velocity maps at the periods from 20 to 91 s using amplitude in both X and Y components. Figure 3.14 shows the 2-D Love wave phase velocity maps at the periods from 20 to 91 s using amplitude only in

Y components. The corresponding standard error of phase velocity was estimated from model covariance matrix and its distribution across the study area is shown in Figure 3.13l and 3.14l, respectively. The Love wave phase velocities calculated using amplitude in both X and Y components are more consistent at each nearby periods. We quantified their differences by subtracting the Love wave phase velocities using amplitude only in Y component by those using amplitude in both X and Y components (Figure 3.15). As shown in Figure 3.15l, the 1-D phase velocity differences for these two are larger at the long periods (76 s and 91 s) than those at the short and median periods (20-67 s). The difference variation is small in the median periods (45 s) and increases from median periods to short and long periods (Figure 3.15a-3.15k). Therefore, the Love wave phase velocities using amplitude in both X and Y components will be described below and used to invert for V_{SH}.

3.4.2. 1-D and 2-D Love Wave Phase Velocity

Average Love wave phase velocities for the entire study region were obtained at the periods of 20, 22, 25, 27, 30, 34, 40, 45, 50, 59, 67, 77, and 91 s and vary from 3.54 km/s at 20 s to 4.32 km/s at 91 s (Figure 3.16a). In the inversion, phase velocity at all grid nodes is assumed to be the same and only one model parameter for phase velocity is solved along with the two-plane wave parameters. The standard error for each phase velocity is taken from a posteriori model covariance matrix calculated in the inversion. Average Love wave phase velocity is much larger than average Rayleigh wave phase velocity at the same period as expected (Figure 3.16a). While compared to the predicted Love wave phase velocities from the global AK135 model, these values are smaller. The differences between observed and predicted Love wave

phase velocities are larger than those between observed and predicted Rayleigh wave phase velocities, especially at median and long periods (45-91 s) (Figure 3.15a). Such different deviations between Rayleigh and Love wave from the predictions of the isotropic Ak135 model indicate the presence of anisotropy in the crust and upper mantle of NE Tibet.

Average Love wave phase velocities at different tectonic provinces are also calculated. We divided the study area into three sub-tectonic-provinces, the Songpan-Ganzi Terrane (SGT), the Qinling-Qilian Orogen (QQO), and the Gobi-Alashan Platform (GAP), which are separated by the Kunlun and Haiyuan faults (Figure 3.1). The inversion for the average phase velocity in each province is conducted by assuming uniform phase velocity at all the nodes within the province. Similar to Rayleigh wave phase velocities [*Li et al.*, 2013], Love wave phase velocities generally decrease from the GAP in the north to the SGT in the south (Figure 3.16b). The GAP is characterized with the highest velocities ranging from 3.80 km/s at 20 s to 4.59 km/s at 91 s while the SGT has the lowest velocities from 3.50 km/s at 20 s to 4.04 km/s at 91 s. Phase velocities in the QQO are comparable to the average phase velocities for the entire study region (Figure 3.16b). The large difference in phase velocities among the three sub-regions reveals strong lateral heterogeneity in the crust and upper mantle in the NE Tibetan Plateau.

2-D Love wave phase velocities were calculated at the periods from 20 s to 91 s using the 1-D average phase velocities as starting values. We computed the phase velocities at each grid node with grid spacing of ~0.5^{o} and then interpolated the phase velocities on finer grids with an interval of 0.1^{o} by 0.1^{o} for generating the maps. The

standard error of phase velocity was estimated from model covariance matrix and interpolated on a finer grid as well. The standard errors at different periods have similar trends with small errors near the center of the study region and increasing errors towards the edge as shown in Figure 3.13i that shows 2σ of phase velocity perturbations in percentage at 34 s.

Love waves and Rayleigh waves are sensitive to shear velocities in different ways even for an isotropic model. Generally, Love waves are more sensitive to shallower structures than Rayleigh waves at the same period. Thus the lateral variations of phase velocities could be different between Rayleigh and Love waves at the same period even for an isotropic media, which then reflect vertical variation of structure. Rayleigh wave and Love wave phase velocity maps share similar patterns at each period. The low velocity anomaly (~3%-7%) is imaged along the Kunlun fault in both Rayleigh wave and Love wave phase velocity maps (Figure 3.13a-3.13k, Figure 3.B). The anomaly is consistently imaged at all periods even though the inversion for phase velocity is applied to each period independently. Its magnitude is reduced at long periods due to smoothing from increasing wavelength, and its location closely matches with the strike of the Kunlun fault. The consistence of this anomaly on different phase velocity maps and between Rayleigh and Love waves clearly evidence that it must be from a true structure. Compared with Rayleigh wave phase velocity map, the shape and magnitude of these anomalies from Love wave vary slightly at different periods, reflecting vertical variations of shear velocity anomalies as well as radial anisotropy. The resolution tests for input models with ±3% Rayleigh wave (Figure 2.7) and Love wave (Figure 3.A) phase velocity perturbations show that the

anomaly pattern can be well recovered within and between the station arrays although the overall resolution decreases with increasing period and at the edge of the study area.

3.4.3. 1-D and 3-D Shear Wave Velocity

We inverted the Love wave phase velocities for V_{SH} velocity model and calculated radial anisotropy from V_{SH} and previously obtained V_{SV} model from Rayleigh wave phase velocities. The average 1-D shear wave velocity model (V_{SV} and V_{SH}) and radial anisotropy were computed from the average phase velocities for the entire study region. Then 3-D isotropic shear wave velocity and radial anisotropy models were developed by combining 1-D V_{SV} and V_{SH} models at all grid nodes.

The SH velocities (V_{SH}) in the average 1-D model range from 3.18 km/s in the shallow crust to 4.27 km/s at 130 km depth (Figure 3.8b). Compared to the previously obtained V_{SV} model, 1-D V_{SH} model is significantly higher in the lower crust and uppermost mantle (Figure 3.8b), reflecting strong radial anisotropy, while small differences exist in the middle crust and at the depths of 70~110 km between the V_{SV} and V_{SH} (Figure 3.8b). The absolute velocity of V_{SV} and V_{SH} and the velocity perturbation maps at 6 layers from the middle crust to 130 km are shown in Figure 3.17, 3.18, 3.20 and 3.21. 3-D view of the velocity perturbation maps are also shown in Figure 3.27. The major features of V_{SH} model (Figure 3.18) are generally consistent with our previous obtained Vsv model (Figure 3.17). In the middle crust, low velocities are present along the strike of the Kunlun fault and the strong high velocities are observed beneath the northern Qilian orogenic belt and part of the Gobi-Alashan Platform. In the lower crust, the magnitude of low velocity anomalies

increases, while the magnitude of the high velocities decreases. The low velocity anomalies extend to the uppermost mantle beneath the Kunlun fault. The clear difference between the V_{SH} and V_{SV} models is in the middle and lower crust, where the offset of the low velocity anomaly from east to west is shown in the V_{SV} model, but is not present in the V_{SH} model. The lateral variations in the V_{SV} and V_{SH} models are imaged similarly on the velocity anomaly maps (Figure 3.20~3.21).

We computed the isotropic or effective shear wave velocity from V_{SH} and V_{SV} using a Voigt average, $V_S = \sqrt{(2V_{SV}^2 + V_{SH}^2)/3}$ [*Babuška and Cara*, 1991]. The absolute Vs (Figure 3.19) and Vs anomaly maps (Figure 3.22) are similar with those of V_{SV}. Four cross-sections of absolute Vs and Vs perturbation are shown in Figure 3.23 and Figure 3.24. The locations of the four vertical profiles are shown in Figure 3.22c. The most striking feature in the absolute Vs cross-section is the low velocity anomaly beneath the restraining bend of the Kunlun fault at the depth of 90-130 km (Figure 3.23a, 3.23c), while no low velocity anomaly is imaged beneath the Haiyuan fault. Additionally, the low velocity along the strike of the Kunlun fault shifts from east in the middle and lower crust to west part beneath the restraining bend in the uppermost mantle (Figure 3.24c).

3.4.4. 3-D Radial Anisotropy

The radial anisotropy is computed from V_{SH} and V_{SV} in the medium as $\gamma = (V_{SH}-V_{SV})/V_S$. Radial anisotropy at different depths and along four vertical cross-sections is shown in Figures 3.25 and Figure 3.26. 3-D view of the velocity perturbation maps are also shown in Figure 3.28. On the first order, anisotropy varies strongly with depth, which can be seen more clearly on the cross sections (Figure

3.26). In the shallow crust, negative anisotropy ($V_{SV}>V_{SH}$) is present beneath most of the NE Tibetan Plateau with larger values associated with higher elevations such as the Kunlun and Qilian mountains. Anisotropy in the lower crust is dominated by positive values ($V_{SH}>V_{SV}$) and the anisotropy becomes stronger towards the eastern and northern edge of the plateau. The uppermost mantle is largely isotropic, which is underlined by uniformly positive anisotropy beneath 90 km depth.

Radial anisotropy also shows significant lateral variations in NE Tibet. In the middle crust, positive radial anisotropy ($V_{SH}>V_{SV}$) with amplitudes in excess of 6% exists beneath the southern Qilian orogenic belt, and negative radial anisotropy ($V_{SV}>V_{SH}$) down to -3% is imaged beneath the restraining bend of the Kunlun fault (Figure 3.25a, 3.26). Despite the lower crust is dominant with positive anisotropy, the anisotropy (~3%) beneath the Kunlun restraining bend and its vicinity is significantly smaller than that in the West Qinling and East Kunlun Orogenic belts (10%) (Figure 3.25b, 3.26a). In the lithosphere mantle (Moho-90 km), the most anisotropic region is beneath the Kunlun restraining bend with a value of -3%. At depths below 90 km, positive radial anisotropy is almost uniformly imaged beneath the entire NE Tibetan Plateau, which is probably associated with large-scale asthenosphere flow.

3.5. Discussions

3.5.1. A Comparison with Previous Studies on Radial Anisotropy

Several radial anisotropy studies have been carried out in the Tibetan plateau [*Shapiro et al.*, 2004; *Xie et al.*, 2013; *Chen et al*., 2009; *Huang et al.*, 2010; *Duret et al.*, 2010; *Guo et al.*, 2012]. Most of studies are at a plateau-wide scale and have poor

lateral resolution in NE Tibet [*Duret et al.*, 2010; *Shapiro et al.,* 2004; *Chen et al*., 2009; *Xie et al.,* 2013]. Their vertical resolution for radial anisotropy is also limited to shallow depths because of relative short periods (10-50 s) for Love wave phase velocities, which is a limitation from ambient noise data analysis. The lack of studies on radial anisotropy using teleseismic data is due to the lack of suitable methods for Love wave tomography, and the quality limitation of Love wave seismic data recorded at transverse components. In this study, we obtained Love wave phase velocities up to 90 s by extending the TPW method to Love waves from teleseismic events. The derived radial anisotropy model has reasonable resolution to 130 km.

Our radial anisotropy presents distinctive vertical variation of anisotropy with general negative values in the shallow crust especially beneath high mountain ranges, strong positive anisotropy in the lower crust, averaged isotropy in the mantle lithosphere to 90 km and weak positive anisotropy beneath it. This vertical variation of anisotropy correlates with typical continental lithosphere strength change. The weakest lower crust and the asthenosphere are characterized by positive radial anisotropy. *Xie et al.* [2013] also imaged $V_{SH}>V_{SV}$ in the middle and lower crust beneath NE Tibet while the study by *Chen et al.* [2009] showed negative radial anisotropy ($V_{SV}>V_{SH}$) beneath the Qilian and Qinling Orogenic belts in the middle crust. In addition to layered variation, our model also images strong lateral variation of anisotropy. One prominent feature is relatively negative anisotropy beneath the East Kunlun Mountains. Such small-scale anisotropic feature has not been reported from previous studies due to the large-scale nature and poor lateral resolution in those studies.

3.5.2. Mechanism of Radial Anisotropy

Seismic anisotropy can be considered as a proxy of aligned minerals resulted from either crystallographic or lattice preferred orientation (CPO, LPO) [e.g., *Montagner*, 1998], or shape preferred orientation (SPO) of material with distinct isotropic elastic properties [e.g., *Silver and Chan*, 1991]. Anisotropy due to the LPO of anisotropic minerals could be resulted from flow or tectonic stress in the crust and mantle. For example, *Barazangi and Ni* [1982] and *Godfrey et al.* [2000] suggested strong faulting causes observed seismic anisotropy. Anisotropy due to SPO could arise from different mechanisms such as dry or liquid-filled cracks [*Figueiredo et al.*, 2013] and sills or lenses of partial melt [*Takeuchi et al.*, 1968; *Kawakatsu et al.*, 2009]. Here we focus on the most likely cause (or causes) for crustal radial anisotropy and upper mantle radial anisotropy.

3.5.2.1. Crustal Radial Anisotropy

Negative radial anisotropy ($V_{SV}>V_{SH}$) is present in the upper crust especially beneath high mountain belts (Figure 3.25a, 3.27). Stress alignment micro-cracks were suggested to attribute to anisotropy of upper crust, where pressure is low enough to allow the cracks remain open [e.g., *Figueiredo et al.*, 2013]. The obvious correlation between negative radial anisotropy and high mountain belts reflect current horizontal shortening and vertical extension in response to the present-day compressional stresses [*Heidbach et al.*, 2010], which would induce the formation and alignment of vertical micro-cracks that produce $V_{SV}>V_{SH}$ anisotropy.

Generally, the mid-lower crust (15 km-Moho) is characterized with positive anisotropy ($V_{SH}>V_{SV}$) with large strength beneath the Qinling and Qilian orogens and relative weak values beneath the Kunlun restraining bend and its vicinity. The amplitude of anisotropy in the middle crust ranges from -2% to 6%, while that in the lower crust varies from 3% to 12%. It has been suggested that the formation of positive mid-lower crustal anisotropy beneath the Tibetan plateau can be resulted from the horizontal alignment of mica crystals [*Shapiro et al.,* 2004; *Huang et al.,* 2010]. A small amount of mica minerals can induce strong anisotropy in the middle to lower crust [*Stein and Wysession,* 2003]. Mid-lower crustal flow was suggested to align crustal minerals such as mica, amphibole [*Li et al.,* 2011; *Shapiro et al.,* 2004; *Huang et al.,* 2010]. If this is the case, the flow should be stronger beneath Qinling and Qilian orogens where positive anisotropy is stronger than beneath the Kunlun Mountains. It would be hard to understand why the crustal flow is more vigorous at the plateau's edge than in its interior. Moreover, strong crustal flow in NE Tibet is not supported by absolute shear wave velocity model, which doesn't image a low-velocity layer in middle or lower crust. Additionally, geological observations argued that the lower crustal flow is not necessary present to account for crust shortening in the NE Tibetan plateau [*Lease et al.,* 2012]. Therefore, the observation of positive anisotropy ($V_{SH}>V_{SV}$) more likely reflects past deformation at the formation of mid-lower crust instead of current crustal flow.

3.5.2.2. Upper Mantle Radial Anisotropy

Anisotropy in the mantle lithosphere at the depths of Moho-90 km varies from -2% to 2%, which is much weaker than in the lower crust and deeper upper mantle. Frozen fabrics in the mantle lithosphere could vary laterally and have been averaged out in the tomography. This weak anisotropy also indicates that mantle lithosphere in NE Tibet has not been largely deformed by current plateau-building process.

In contrast to largely isotropic mantle lithosphere above 90 km, the entire NE Tibet region is dominant by positive anisotropy ($V_{SH}>V_{SV}$) at the depths of 90-130 km, probably suggesting a transition from lithosphere to asthenosphere at around 90 km. The depths of LAB were estimated at 80-100 km in this region based on shear wave velocity changes with depth [*Li et al.,* 2013]. Since the boundary from lithosphere to asthenosphere is defined by the change of mechanical strength instead of composition, the LAB might be better determined using anisotropy variation than absolute velocity change. The positive radial anisotropy could be caused by LPO of olivine mineral due to large-scale asthenosphere flow associated with the absolute motion of Eurasia, as has been suggested by previous studies [*Li et al.,* 2011; Zhang et al., 2010].

3. 5.2.3. The Kunlun Restraining Bend

The Kunlun restraining bend, at which the Kunlun fault changes its strike from EW to ESE-WNW, is located in the southwest of the study area. The crust and upper mantle beneath the restraining bend and the nearby Kunlun Mountains show anomalous low velocity and negative radial anisotropy ($V_{SV}>V_{SH}$) in the entire lithosphere. The low velocity anomaly was interpreted to be due to anomalously high

temperature and associated partial melting resulted from localized asthenosphere upwelling after the delamination of a thick lithosphere root [*Li et al.,* 2013]. The thick lithosphere root inferred here was speculative because it was not observed in the shear wave model. The newly developed radial anisotropy model provides additional evidence for a thickened lithosphere beneath the restraining bend. This can be seen from the continuous $V_{SV}>V_{SH}$ anomalies beneath the restraining bend from the shallow crust to the mantle lithosphere except in the lower crust where the positive anisotropy value of 3% is still significantly smaller than in its surrounding regions. These anisotropy anomalies can be explained by vertical alignment of anisotropic minerals in the crust and mantle lithosphere due to large compressional stress, providing evidence for coherent lithosphere deformation that could have resulted in a thick lithosphere root. Such coherent lithosphere deformation is not observed in the eastern portion of the Kunlun neither in the Qinling and Qilian orogens, suggesting that the lithosphere shortening in most of the NE Tibet is not as strong as in the Kunlun restraining bend and the interiors of the plateau and the Kunlun restraining bend probably marks northeastern boundary of the highly-deformed plateau lithosphere.

3.6. Conclusion

We developed a 3-D radial anisotropy model with resolution up to ~130 km from V_{SV} and V_{SH} obtained from 2-D Rayleigh wave (20~100 s) and Love wave (20~91 s) dispersions curves. The anisotropic model reveals complex deformation in the NE Tibetan plateau. Negative radial anisotropy ($V_{SV}>V_{SH}$) is present in the

shallow crust especially beneath high mountain belts, which could be caused by aligned vertical cracks or anisotropic silicates, reflecting horizontal shortening in these areas. A positive radial anisotropy pattern ($V_{SV}>V_{SH}$) was observed in the middle and lower crust, probably due to the frozen horizontal alignment of mica crystals at the formation of lower crust. The mantle lithosphere above 90 km is largely isotropic while weak positive anisotropy appears beneath 90 km, which probably marks the lithosphere-asthenosphere boundary. Asthenosphere flow is the main source for the positive anisotropy at the depth of 90-130 km. The most pronounced lateral variation in NE Tibet is a low velocity anomaly and relative negative radial anisotropy in the entire lithosphere beneath the Kunlun restraining bend and its nearby mountains. The anisotropy anomaly suggests coherent lithosphere deformation in this area that could have resulted in a thick lithosphere root. The low velocity anomaly can be explained by high temperature and associated partial melting after the delamination of the thick root. Significant large positive anisotropy (up to 12%) was imaged in the lower crust beneath the eastern portion of the Kunlun Mountains and the Qilian and Qinling orogens, implying that shortening in the shallow crust is not passed to the lower crust. The Kunlun restraining bend likely marks a transition from coherent lithosphere deformation in the interiors of the plateau to shallow crustal deformation at its northeastern edge.

3.7. Appendix

Appendix 3.A Resolution test for Love wave phase velocity

We carried out resolution test to understand resolvability of Love wave phase velocities and their spatial resolution at different periods in the study area. A checkerboard velocity model with a cell size of $1.5^{o} \times 1.5^{o}$ was constructed and it contained alternating positive and negative perturbations of ±3% with an average velocity of 4 km/s (Figure 3.A). Synthetic incoming wave field for each event is assumed as the sum of two plane waves with known initial amplitude, phase and propagation direction. The choice of the two plane waves is arbitrary. One plane wave propagates at 4° off the great-circle path with an initial amplitude of 0.7 and the other travels at 10° with an amplitude of 0.3, which are typical observed directions and normalized amplitudes for the primary and secondary plane waves, respectively. The initial phase for both plane waves is set as zero. Then synthetic amplitude and phase of Love waves were computed from the checkerboard model using the same stations, events, and raypaths from the real data. Random noises of 10% of the maximum phase and amplitude values were added to the synthetic data. These synthetic data with noise were used to calculate 2-D Love wave phase velocity using the same inversion scheme as was applied to the real data. As shown in Figure 3.A, the pattern of the velocity anomalies within and close to the station array (inside the 2% error contour) can be well recovered at 25, 50 and 77 s (Figure 3.Aa, 3.Ab, 3.Ac). However, fading and smearing occur around the edge of the model where large errors were given at the edge nodes and crossing raypaths are not dense (Figure 3.Aa, 3.Ab, 3.Ac).

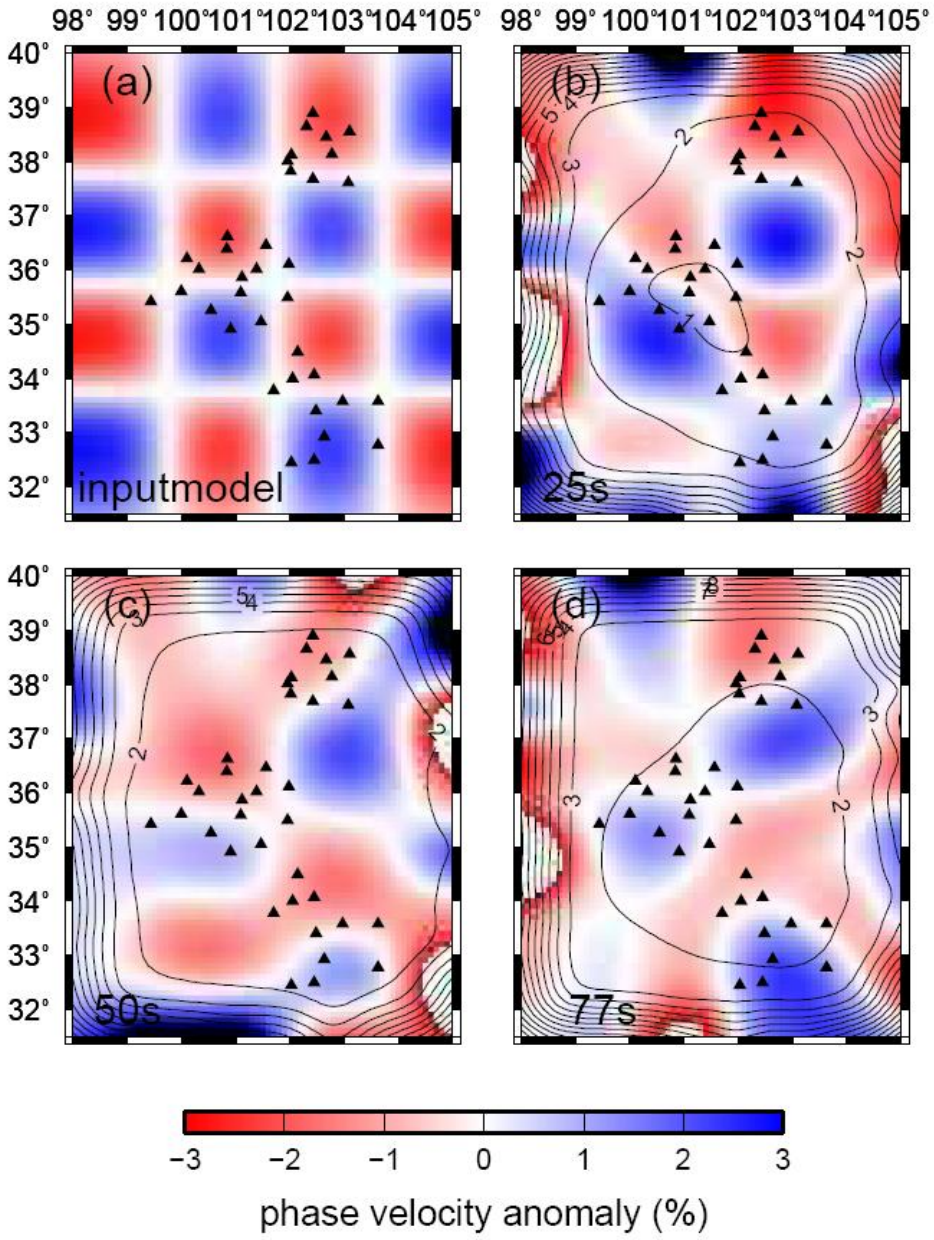

Figure 3.A. Input and recovered checkerboard models for resolution tests on Love wave phase velocities. (a) The input model with anomaly size of $1.5^{o} \times 1.5^{o}$. (b-d) Recovered models at periods of 25, 50 and 77 s. The black line denotes contour of 2σ on phase velocity perturbation at corresponding periods. Triangles denote the stations.

Appendix 3.B 2-D Rayleigh wave phase velocity map at 12 periods between20~100s.

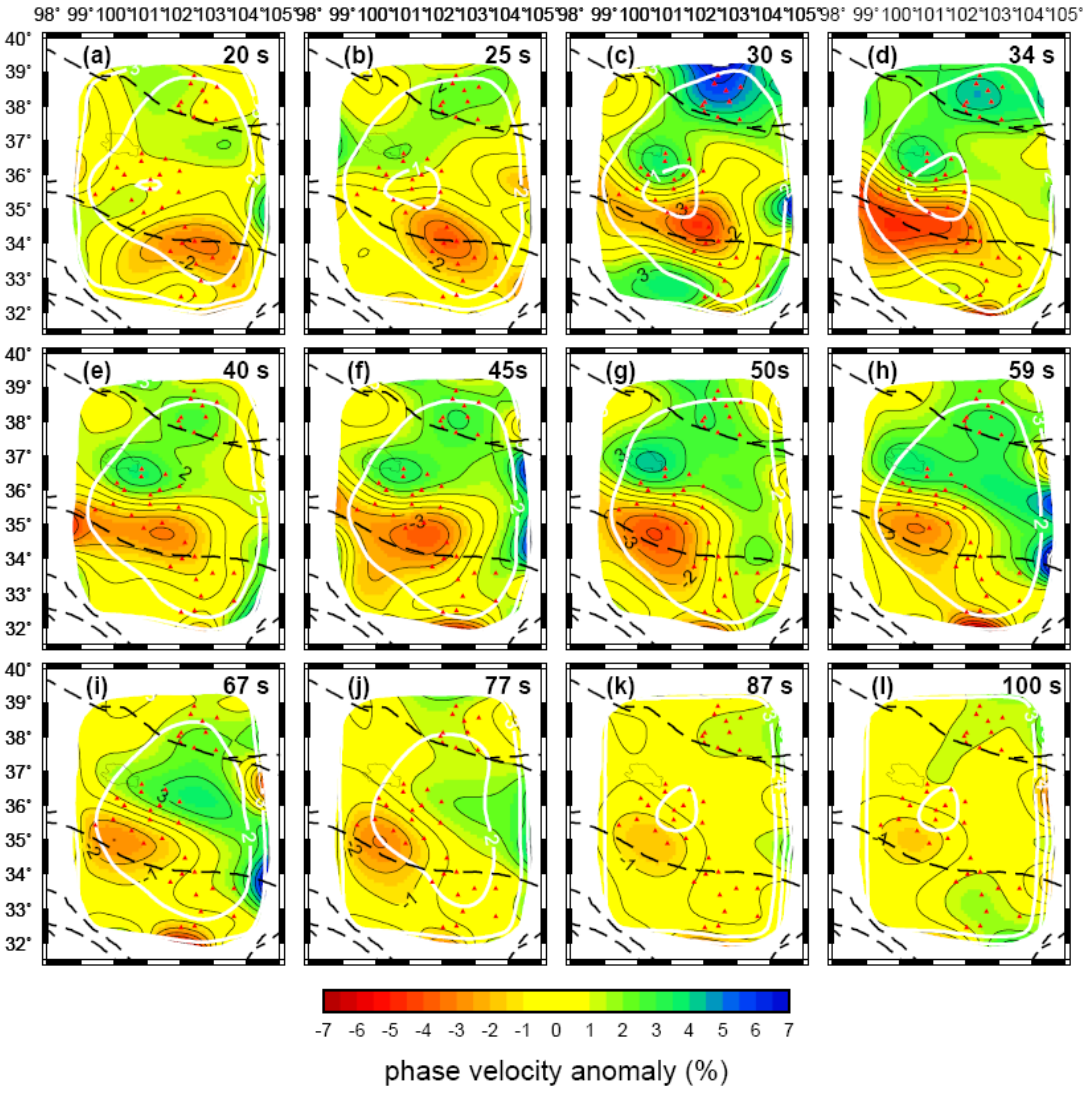

Figure 3.B. Maps of Rayleigh wave phase velocity perturbations. The white lines are the contour of 2σ of Rayleigh phase velocity perturbation at the corresponding periods.

Appendix 3.C Shear wave velocity forward modelling for low velocity anomaly centered at ~120 km depth beneath the Kunlun restraining bend

To examine the robustness of the low-velocity anomaly centered at ~120 km depth beneath the Kunlun restraining bend in the shear wave velocity (V_{SV} and V_{SH}) models, we conducted a series of experiments of forward modeling for V_{SV} and V_{SH} through models that locate the low-velocity anomaly at different depths (lower crust, uppermost mantle, and at the depth of 100-140 km) (Figure 3.C1, Figure 3.C2). At each test, we manually assigned a low-velocity anomaly at different depths and kept velocity values the same with global model AK135 at other depths and used it as an initial model. We carried out the forward modeling to obtain the phase velocities, which were then used for shear velocity inversion using the same errors from observed average phase velocities. Because of smoothing between adjacent layers and errors in phase velocity measurements, the recovered shear wave velocity models show a gradually varied low velocity zone that is slower and thicker than that in the input models. We carried out the experiments to test the low-velocity anomaly in both V_{SV} (Figure 3.C1) and V_{SH} (Figure 3.C2) models.

We first assigned the low-velocity anomaly in the lower crust (at the depths of 35 km-Moho), as shown in the Figure 3.C1a and Figure 3.C2a. In the V_{SV} and V_{SH} models, the velocity anomaly can be well recovered in the lower crust, but the velocity anomaly would also lower the velocities in the middle and uppermost mantle, especially in the uppermost mantle above 80 km.

We then assigned the low-velocity anomaly in the uppermost mantle (at the depths of Moho-90 km). In the V_{SV} and V_{SH} models, the velocities in the uppermost

mantle in the recovered model are larger than those in the initial model, while the velocities in the lower crust are lower than that in the initial model (Figure 3.C1b and Figure 3.C2b). The recovered velocity models are smoothed at depths, but the lower values in the uppermost mantle can still be observed.

Finally, the low-velocity anomaly was assigned at the depths of 90-140 km, consistent with the depth of observed low velocity anomaly. Both recovered V_{SV} and V_{SH} models are smoothed. In the V_{SV} model the low-velocity anomaly can be well recovered, while that in the V_{SH} model is close to the AK135 model, indicating poor sensitivity to great depths from Love waves.

The low velocity anomaly beneath the restraining bend of the Kunlun fault is observed at the depths of 80~140 km centered at ~120 km depth. In the experiments, the recovered velocities at these depths are higher than the input low velocities, reflecting that the observed low velocities are probably lower than as it shows. Additionally, the experiments also demonstrate that the low velocity anomaly at ~120 km cannot be an artifact from low velocity in the lower crust or uppermost mantle.

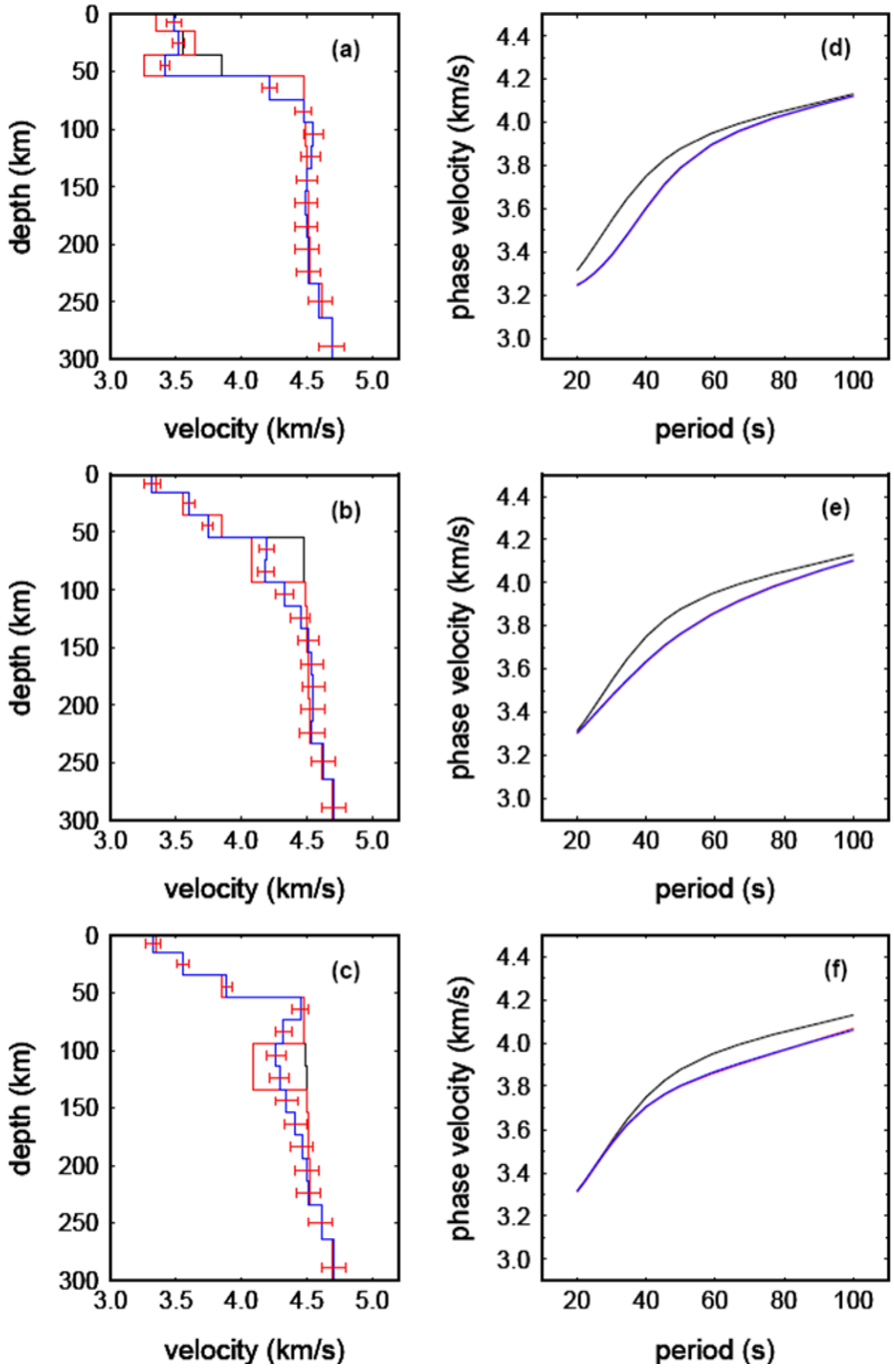
(a)
(b)
(c)
(d)
(e)
(f)
depth (km)
velocity (km/s)
phase velocity (km/s)
period (s)
0
50
100
150
200
250
300
3.0
3.5
4.0
4.5
5.0
20
40
60
80
100
4.4
4.2
4.0
3.8
3.6
3.4
3.2
3.0

Figure 3.C1. V_{SV} models with different low velocity anomaly at different depths (lower crust, uppermost mantle, and at the depths of 90-140 km) (Figure 3.C1a, 3.C1b, and 3.C1c) and their associated Rayleigh wave phase velocities (Figure 3.C1d, 3.C1e, and 3.C1f). Line styles for the velocity models are consistent with those for the phase velocities. The red solid lines in the Figure 3.C1a, 3.C1b, and 3.C1c indicate the initial shear wave velocity model with low velocity anomaly at different depths modified from the global model AK135 (black solid lines). The blue solid lines in Figure 3.C1a, 3.C1b, and 3.C1c represent the recovered V_{SV} model from corresponding input models. The error bar is for standard deviation for recovered V_{SV} model. The black solid lines in the Figure 3.C1d, 3.C1e, and 3.C1f represented the predicted Rayleigh wave phase velocities from the AK135 model. And the red and blue solid lines indicate the predicted Rayleigh wave phase velocities from input and recovered V_{SV} model, respectively.

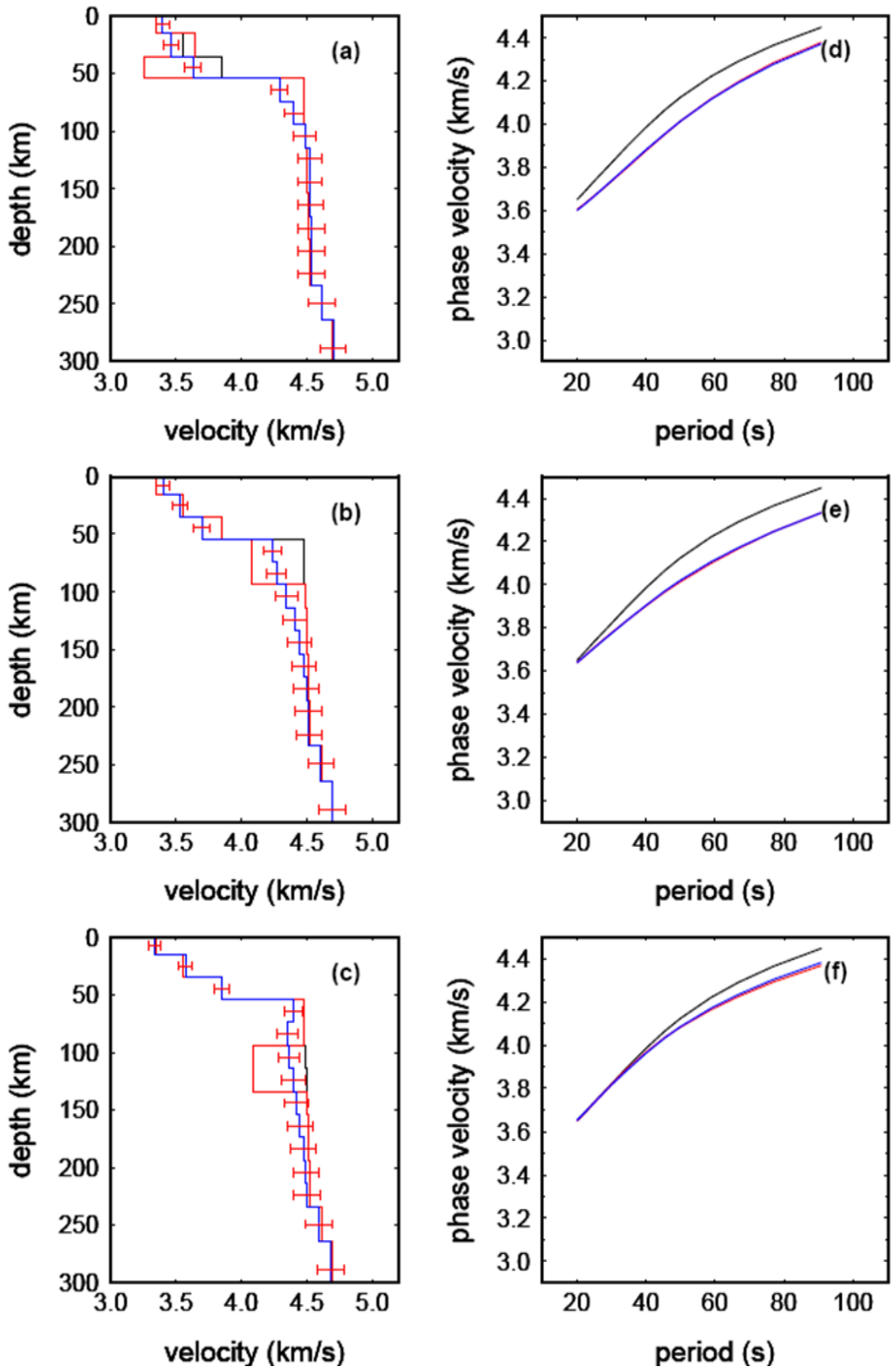

Figure 3.C2. V_{SH} models with different low velocity anomaly at different depths (lower crust, uppermost mantle, and at the depths of 90-140 km) (Figure 3.C1a, 3.C1b, and 3.C1c) and their associated Love wave phase velocities (Figure 3.C1d, 3.C1e, and 3.C1f). Line styles are the same with Figure 3.C1.

3.8. Acknowledgements

Seismic data used in this study were obtained from the Incorporated Research Institution for Seismology Data Management Center. We thank the participants in Northeast Tibet Seismic (NETS) network for collecting the data. All the figures in this paper were made with the Generic Mapping Tools [*Wessel and Smith*, 1998]. This study is supported by NSF grant EAR-0738879.

3.9. References

Babuška, V., Cara, M., (1991), Seismic anisotropy in the Earth. *Modern Approaches in Geophysics*, vol. 10. Kluwer Academic publishers, Dordrecht, The Netherlands

Barazangi, M., & Ni, J. (1982), Velocities and propagation characteristics of Pn and Sn beneath the Himalayan arc and Tibetan plateau: Possible evidence for under-thrusting of Indian continental lithosphere beneath Tibet. *Geology*, *10*(4), 179-185.

Burchfiel, B. C., Zhang, P., Wang, Y., Zhang, W., Song, F., Deng, Q., ... & Royden, L. (1991), Geology of the Haiyuan fault zone, Ningxia-Hui Autonomous Region, China, and its relation to the evolution of the northeastern margin of the Tibetan Plateau. *Tectonics*, *10*(6), 1091-1110.

Chang, L. J., Wang, C. Y., Ding, Z. F., Zhou, M. D., Yang, J. S., Xu, Z. Q., ... & Zheng, X. F. (2008), Seismic anisotropy of upper mantle in the northeastern margin of the Tibetan Plateau. *Chinese Journal of Geophysics*, *51*(2), 298-306.

Chen, C. W., & Li, A. (2012), Shear wave structure in the Grenville Province beneath the lower Great Lakes region from Rayleigh wave tomography. *Journal of Geophysical Research: Solid Earth (1978–2012)*, *117*(B1).

Chen, Y., Badal, J., & Zhang, Z. (2009), Radial anisotropy in the crust and upper mantle beneath the Qinghai-Tibet Plateau and surrounding regions. *Journal of Asian Earth Sciences*, *36*(4), 289-302.

de Figueiredo, J. J. S., Schleicher, J., Stewart, R. R., Dayur, N., Omoboya, B., Wiley, R., & William, A. (2013), Shear wave anisotropy from aligned inclusions: ultrasonic frequency dependence of velocity and attenuation. *Geophysical Journal International*, *193*(1), 475-488.

Duret, F., Shapiro, N. M., Cao, Z., Levin, V., Molnar, P., & Roecker, S. (2010), Surface wave dispersion across Tibet: Direct evidence for radial anisotropy in the crust. *Geophysical Research Letters*, *37*(16).

Forsyth, D. W., & Li, A. (2005), Array analysis of two-dimensional variations in surface wave phase velocity and azimuthal anisotropy in the presence of multipathing interference. *Geophysical Monograph Series*, *157*, 81-97.

Fu, Y. V., Li, A., & Chen, Y. J. (2010). Crustal and upper mantle structure of southeast Tibet from Rayleigh wave tomography. *Journal of Geophysical Research: Solid Earth (1978–2012)*, *115*(B12).

Godfrey, N. J., Christensen, N. I., & Okaya, D. A. (2000), Anisotropy of schists: Contribution of crustal anisotropy to active source seismic experiments and shear wave splitting observations. *Journal of Geophysical Research: Solid Earth (1978–2012)*, *105*(B12), 27991-28007.

Guo, Z., Gao, X., Wang, W., & Yao, Z. (2012), Upper-and mid-crustal radial anisotropy beneath the central Himalaya and southern Tibet from seismic ambient noise tomography. *Geophysical Journal International*, *189*(2), 1169-1182.

Heidbach, O., Tingay, M., Barth, A., Reinecker, J., Kurfeß, D., & Müller, B. (2010), Global crustal stress pattern based on the World Stress Map database release 2008. *Tectonophysics*, *482*(1), 3-15.

Huang, H., Yao, H., & van der Hilst, R. D. (2010), Radial anisotropy in the crust of SE Tibet and SW China from ambient noise interferometry. *Geophysical Research Letters*, *37*(21).

Kawakatsu, H., P. Kumar, Y. Takei, M. Shinohara, T. Kanazawa, E. Araki, and K. Suyehiro (2009), Seismic evidence for sharp lithosphere-asthenosphere boundaries of oceanic plates, *Science*, 324(5926), 499–502, doi:10.1126/science.1169499.

Kennett B.L.N., E.R. Engdahl and R. Buland (1995), Constraints on seismic velocities in the earth from travel times, *Geophys. J. Int*, 122(1), 108-124, doi:10.1111/j.1365-246X.1995.tb03540.x.

Lease, R. O., Burbank, D. W., Zhang, H., Liu, J., & Yuan, D. (2012), Cenozoic shortening budget for the northeastern edge of the Tibetan Plateau: Is lower crustal flow necessary? *Tectonics*, *31*(3).

Li, A. (2011), Shear wave model of southern Africa from regional Rayleigh wave tomography with 2-D sensitivity kernels. *Geophysical Journal International*, *185*(2), 832-844.

Li, A., & Detrick, R. S. (2006), Seismic structure of Iceland from Rayleigh wave inversions and geodynamic implications. *Earth and Planetary Science Letters*, *241*(3), 901-912.

Li, A., Forsyth, D. W., & Fischer, K. M. (2005), Rayleigh wave constraints on shear-wave structure and azimuthal anisotropy beneath the Colorado Rocky Mountains. *The Rocky Mountain Region: An Evolving Lithosphere Tectonics, Geochemistry, and Geophysics*, 385-401.

Li, A., Forsyth, D.W., Fischer, K.M. (2003), Shear velocity structure and azimuthal anisotropy beneath eastern North America from Rayleigh wave inversion. *J. Geophys. Res.*, 108 (B8), 2362. doi:10.1029/2002JB002259.

Li, L., Li, A., Shen, Y., Sandvol, E. A., Shi, D., Li, H., & Li, X. (2013), Shear wave structure in the northeastern Tibetan Plateau from Rayleigh wave tomography. *Journal of Geophysical Research: Solid Earth*, *118*(8), 4170-4183.

Li, Y., Q. Wu, F. Zhang, Q. Feng, and R. Zhang (2011), Seismic anisotropy of the northeastern Tibetan Plateau from shear wave splitting analysis, *Earth Planet. Sci. Lett.*, 304, 147–157, doi:10.1016/j.epsl.2011.01.026.

Liang, C., Song, X., & Huang, J. (2004), Tomographic inversion of Pn travel times in China. *Journal of Geophysical Research*, *109*(B11), B11304.

Meyer, B., Tapponnier, P., Bourjot, L., Metivier, F., Gaudemer, Y., Peltzer, G., ... & Zhitai, C. (1998), Crustal thickening in Gansu-Qinghai, lithospheric mantle subduction, and oblique, strike-slip controlled growth of the Tibet plateau. *Geophysical Journal International*, *135*(1), 1-47.

Mitchell, B. J. (1995), Anelastic structure and evolution of the continental crust and upper mantle from seismic surface wave attenuation, *Rev. Geophys.*, 33(4), 441–462, doi:10.1029/95RG02074.

Molnar, P., and Tapponnier, P. (1975), Cenozoic tectonics of Asia: effects of a continental collision. *Science*, 189, 419–426.

Montagner, J. P. (1998), Where can seismic anisotropy be detected in the Earth's mantle? In boundary layers…. In *Geodynamics of Lithosphere & Earth's Mantle* (pp. 223-256). Birkhäuser Basel.

Pei, S.P., Zhao, J.M., Sun, Y.S., Xu, Z.H.,Wang, S.Y., Liu, H.B., Rowe, C.A., Toksoz, M.N., Gao, X. (2007), Upper mantle seismic velocities and anisotropy in China determined through Pn and Sn tomography, *J. Geophys. Res.*, 112, B05312. doi:10.1029/2006JB004409.

Saito, M. (1988), DISPER80: A subroutine package for the calculation of seismic normal-mode solutions. In D. Doornbos, *Seismological Algorithms: Computational Methods and Computer Programs* (pp. 293-319). New York: Elsevier.

Shapiro, N. M., Ritzwoller, M. H., Molnar, P., & Levin, V. (2004), Thinning and flow of Tibetan crust constrained by seismic anisotropy. *Science*, *305*(5681), 233-236.

Silver, P. G., & Chan, W. W. (1991), Shear wave splitting and subcontinental mantle deformation. *Journal of Geophysical Research: Solid Earth (1978–2012)*,*96*(B10), 16429-16454.

Stein, S., & Wysession, M. (2009). *An Introduction to Seismology, Earthquakes, and Earth Structure*. Wiley. com.

Takeuchi, H., Y. Hamano, and Y. Hasegawa (1968), Rayleigh- and Lovewave discrepancy and the existence of magma pockets in the upper mantle, *J. Geophys. Res.,* 73(10), 3349–3350, doi:10.1029/JB073i010p03349.

Tapponnier, P., & Molnar, P. (1977), Active faulting and tectonics in China. *Journal of Geophysical Research, 82*(20), 2905-2930.

Tarantola, A., and Valette, B. (1982), Generalized nonlinear inverse problem solved using the least squares criterion. *Rev. Geophys. Space Phys.*, 20 (2), 219-232.

Weeraratne, D. S., Forsyth, D. W., Fischer, K. M., & Nyblade, A. A. (2003), Evidence for an upper mantle plume beneath the Tanzanian craton from Rayleigh wave tomography. *Journal of Geophysical Research, 108*(B9), 2427.

Xie, J., M. H. Ritzwoller, W. Shen, Y. Yang, Y. Zheng, and L. Zhou (2013), Crustal radial anisotropy across Eastern Tibet and the Western Yangtze Craton, *J. Geophys. Res. Solid Earth*, 118, 4226–4252, doi:10.1002/jgrb.50296.

Yi, G.X., Yao, H.J., Zhu, J.S., van der Hilst, R.D., (2010), Lithospheric deformation of continental China from Rayleigh wave azimuthal anisotropy. *Chin. J. Geophys.* 53 (2), 256–268.

Zhang, H., Teng, J., Tian, X., Zhang, Z., Gao, R., & Liu, J. (2012), Lithospheric thickness and upper-mantle deformation beneath the NE Tibetan Plateau inferred from S receiver functions and SKS splitting measurements. *Geophysical Journal International*, *191*(3), 1285-1294.

Zhang, Q., E. Sandvol, J. Ni, Y. Yang, and Y. J. Chen (2011), Rayleigh wave tomography of the northeastern margin of the Tibetan Plateau, *Earth Planet. Sci. Lett.*, 304, 103–112, doi:10.1016/j.epsl.2011.01.021.

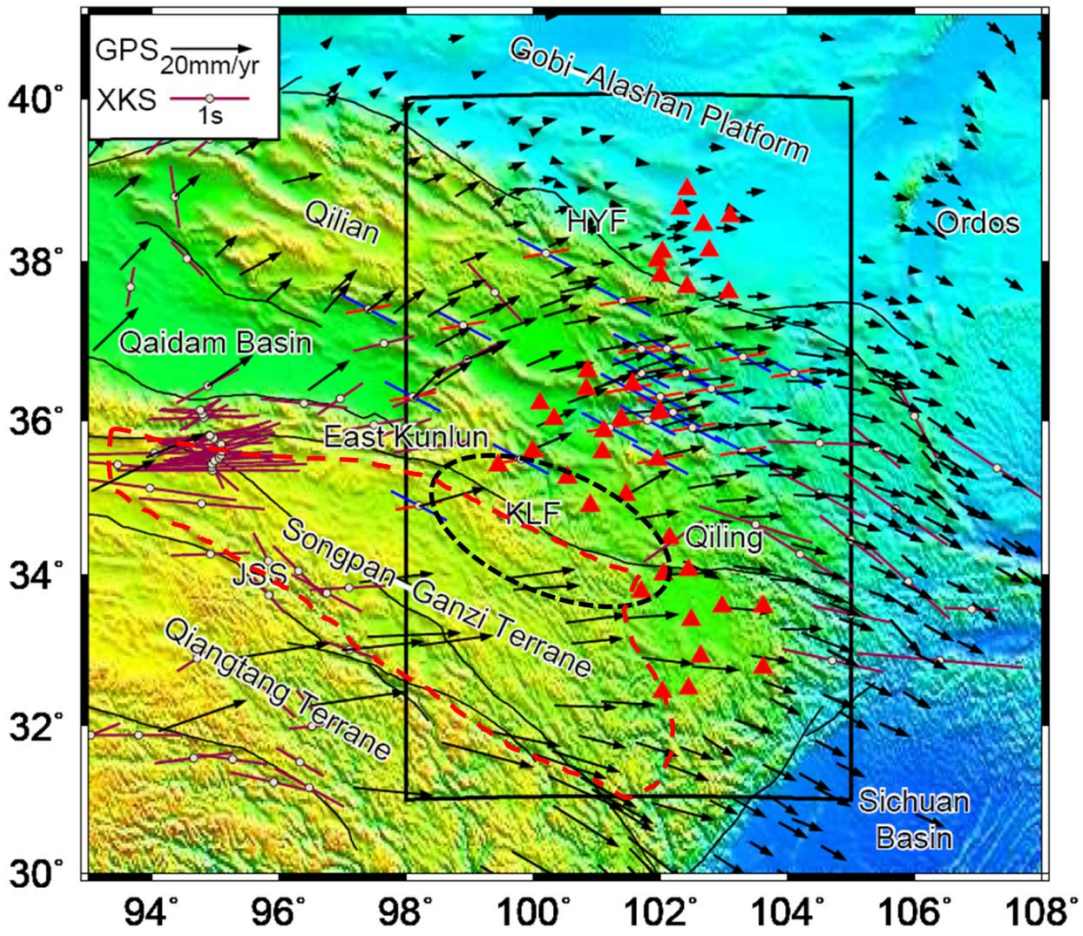

Figure 3.1. Tectonic map superimposed on topography together with previous shear wave splitting results and GPS-vectors in the northeastern Tibetan plateau. The black box indicates our study area. The black solid lines indicate the faults. The black arrows are GPS-vectors relative to Eurasia [*Gan et al.,* 2007]. The bars with different colors represent averaged splitting measurements from previous shear wave splitting studies. The purple bars indicate one-layer anisotropic model [*Guilbert et al.,* 1996; *Herquel et al.,* 1999; *Huang et al.,* 2000; *Liu et al.,* 2008; *McNamara et al.,* 1994; *Li et al.,* 2010]. The two-layer anisotropic models are represented by red and blue bars (red bars, upper layer; blue bars, lower layer) [*Li et al.,* 2010]. The enclosed black

dash line marks the restraining bend at the eastern Kunlun fault. The enclosed red dash line approximately represents the distribution of Songpan-Ganzi flysch [*Yin and Harrison*, 2000]. KLF, Kunlun fault; HYF, Haiyuan fault.

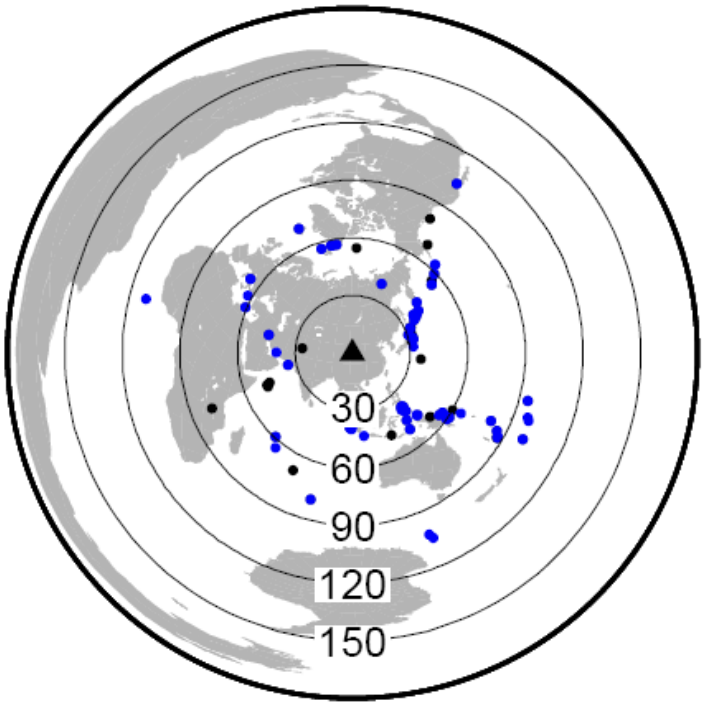

Figure 3.2. Distribution of teleseismic events used for Rayleigh wave tomography (solid dots) and Love wave tomography (blue dots). Triangle denotes the center of the NETS array. Epicentral distance from the center of the seismic array is marked by large concentric circles with numbers.

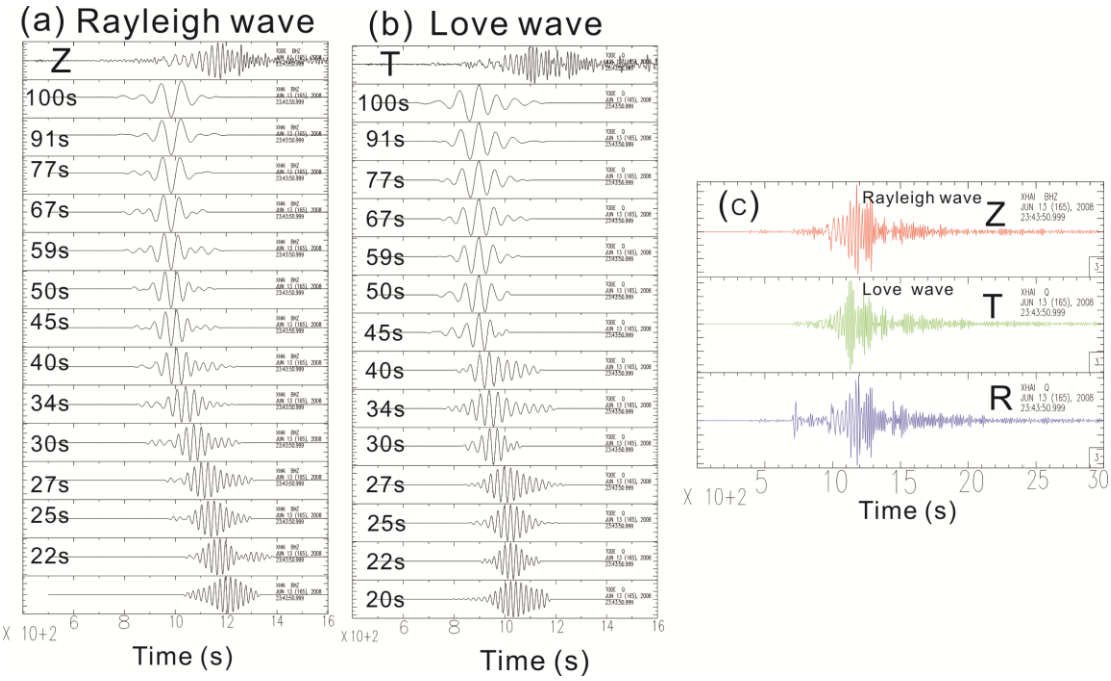

Figure 3.3. Example of good quality Rayleigh wave and Love wave seismograms. (a) Rayleigh wave waveforms and windowed waveforms at different periods. The waveform on the top is a broadband Rayleigh wave train, and other waveforms are filtered with a 10 mHz width filter centered at frequencies from 7 to 50 mHz. The amplitudes of waveforms are scaled to fit the frame. (b) Same as Figure 3.3a, but for Love wave waveforms. (c) Corresponding seismograms at three components; Z, vertical component; T, Transverse component; R, Radial components.

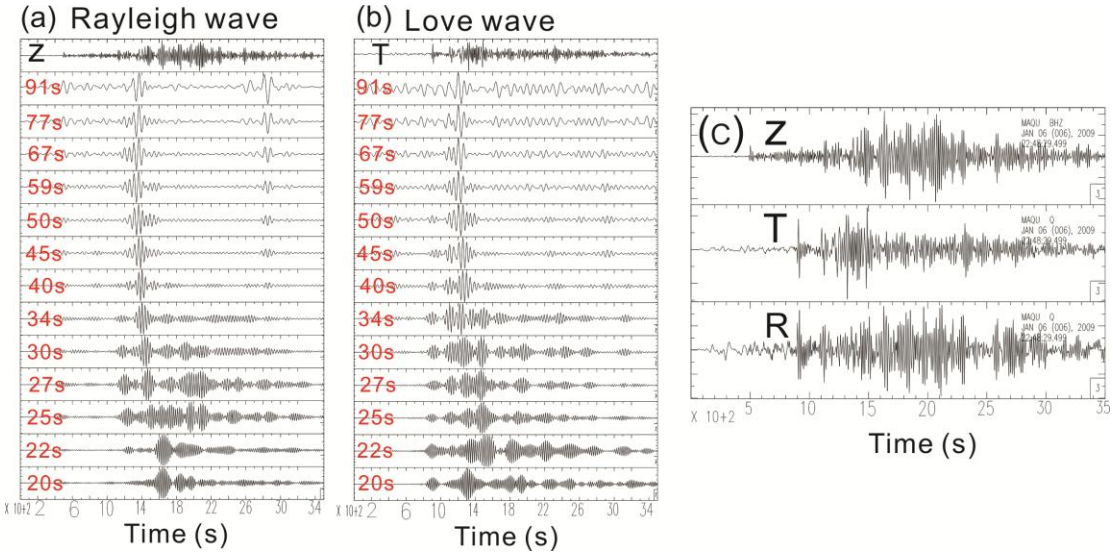

Figure 3.4. Example of interference observed in the Rayleigh wave and Love wave seismograms. Interference due to multipath and higher modes is much stronger at periods between 25 and 40 s than at other periods. The amplitudes of waveforms are scaled to fit the frame.

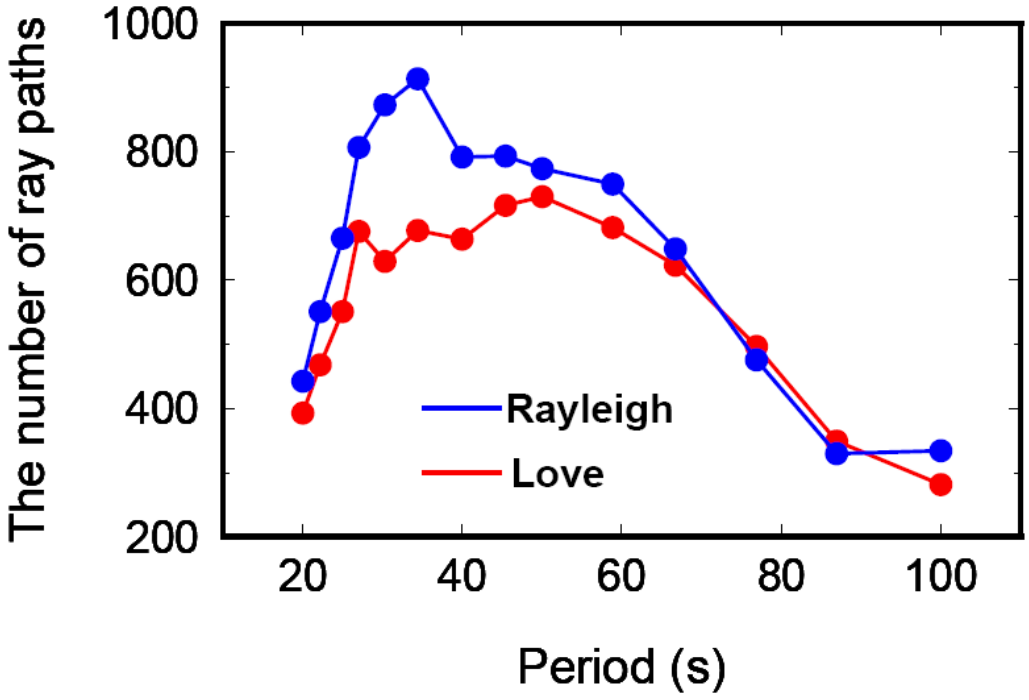

Figure 3.5. Rayleigh wave and Love wave ray path number versus periods.

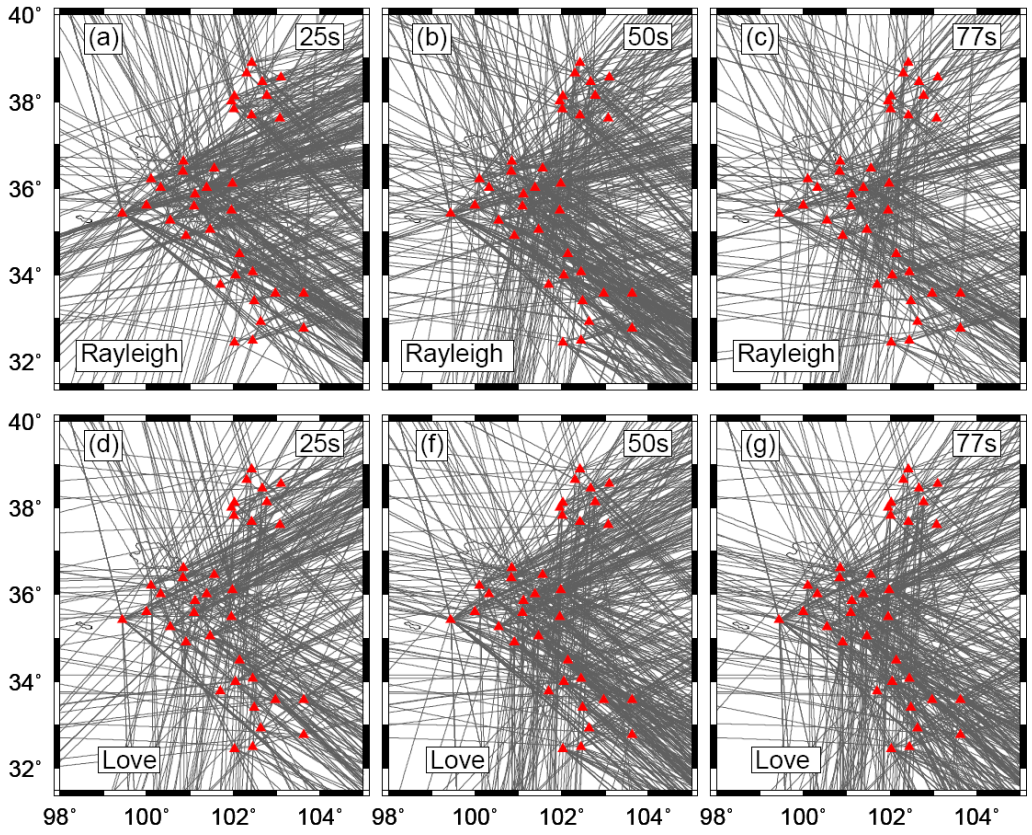

Figure 3.6. Great-circle ray paths at a period 25 s, 50 s and 77 s for Rayleigh wave and Love wave. Red triangles represent seismic stations.

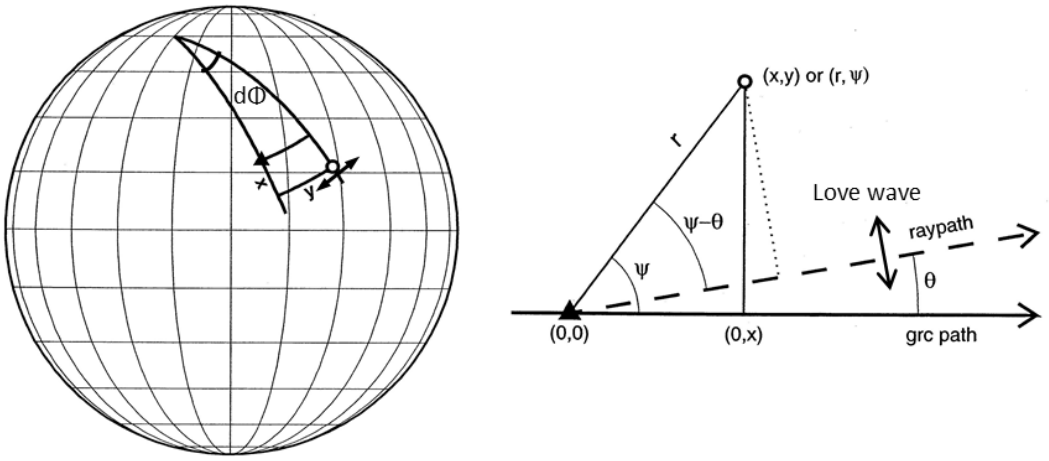

Figure 3.7. Coordinate system for the TPW method for Love wave (modified from *Forsyth and Li* [2005]). (a) Two great-circle paths from the epicenter to the stations in the array for Love wave. X-coordinate is distance along great-circle path relative to distance to a reference station (triangle). Y coordinate of any other point (circle) is distance along the perpendicular, small circle passing through that point to the x-axis; (b) local Cartesian system with (0,0) at the reference station for Rayleigh wave. The long dashed line indicates raypath for one plane wave that deviates from the great-circle path by angle θ. Double arrow indicates Love wave particle.

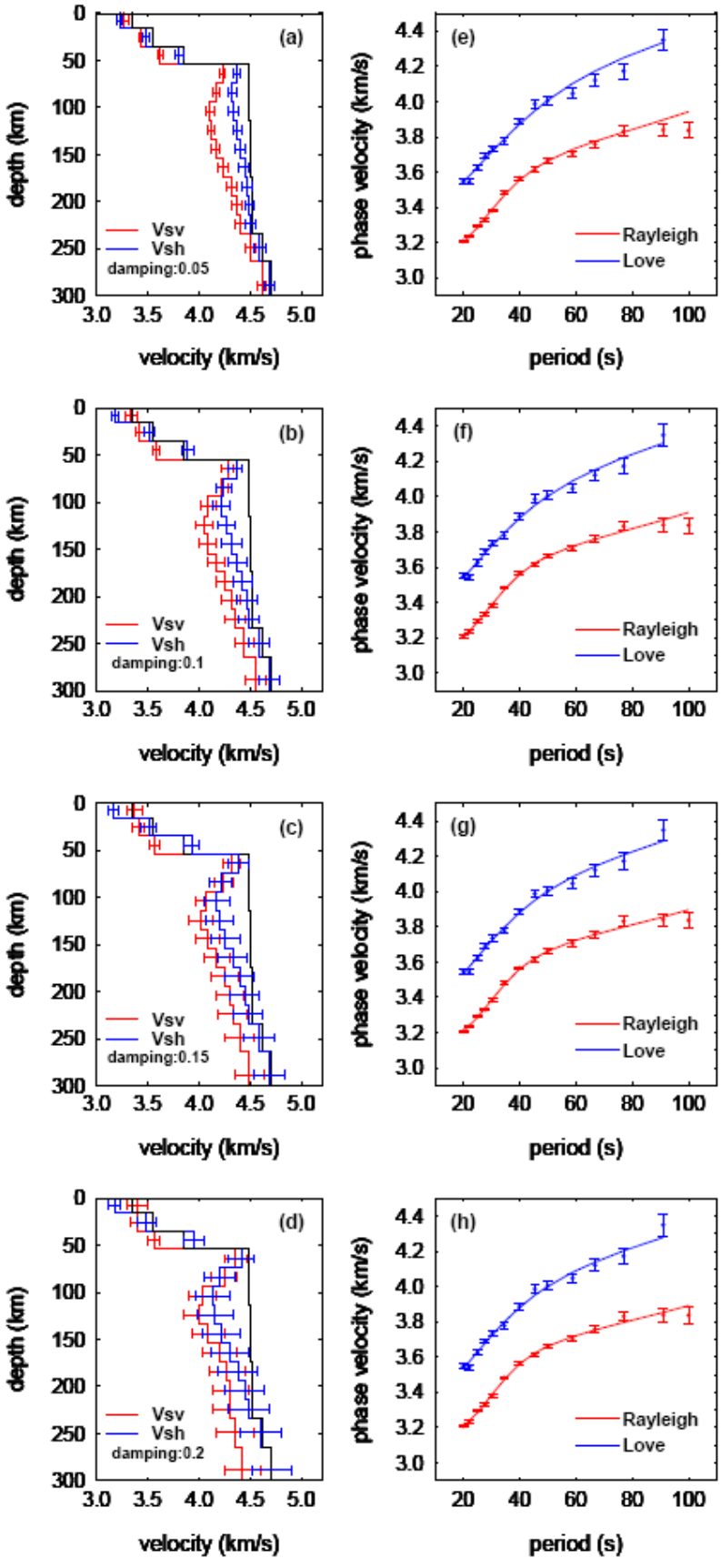
(a)
(b)
(c)
(d)
(e)
(f)
(g)
(h)
depth (km)
velocity (km/s)
phase velocity (km/s)
period (s)
Vsv
Vsh
damping:0.05
damping:0.1
damping:0.15
damping:0.2
Rayleigh
Love

Figure 3.8. 1-D V_{SV} and V_{SH} and corresponding Rayleigh wave and Love wave velocities using different damping of V_{SV} and V_{SH} for inversion. Black lines in the Figure 3.8a, 3.8b and 3.8c indicate the global model AK135 as starting models and the error bar is for standard deviation for shear velocity model. Blue lines and Red lines in the Figure 3.8d, 3.8e and 3.8f represent the predicated Love wave and Rayleigh wave phase velocity, respectively. The points indicate the observed phase velocities and the error bar is for standard deviation for observed phase velocity.

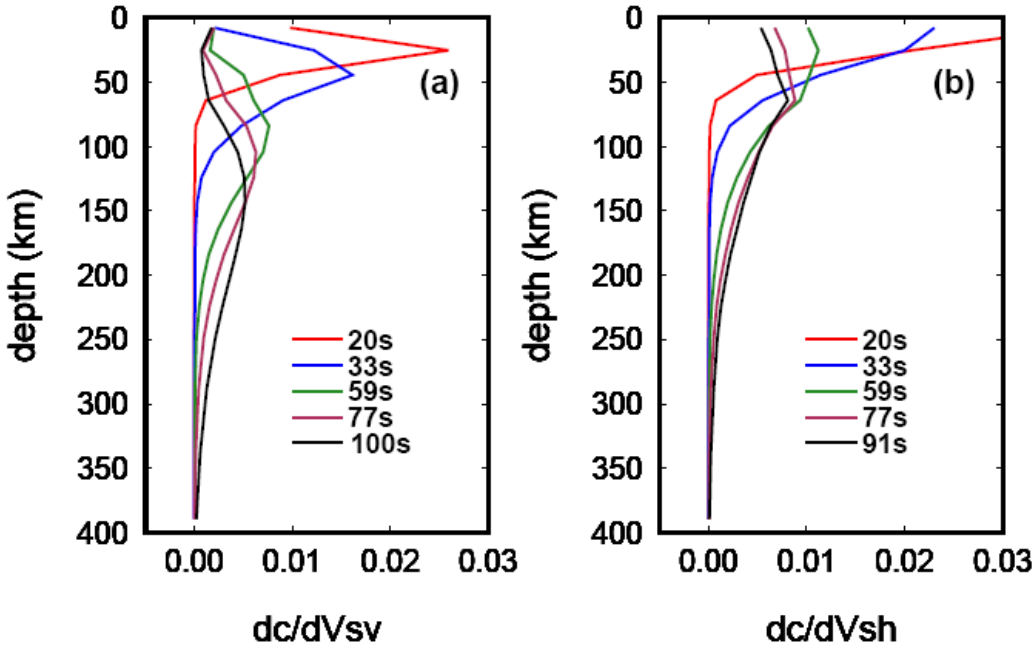

Figure 3.9 (a) Sensitivity kernels of Rayleigh wave and Love wave with respect to V_{SV} (a) and V_{SH} (b) based on the shear velocity model AK135 [*Kennett et al.*, 1995].

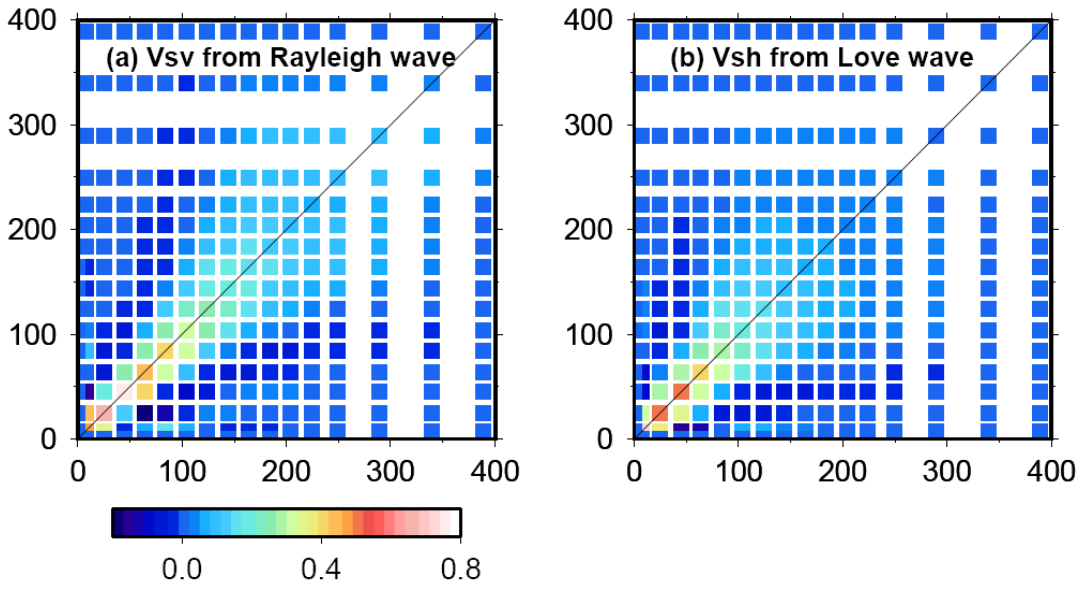

Figure 3.10 Model resolution matrix, the unit for x and y axis is km. The resolution matrix is calculated from the inversion for the reference model.

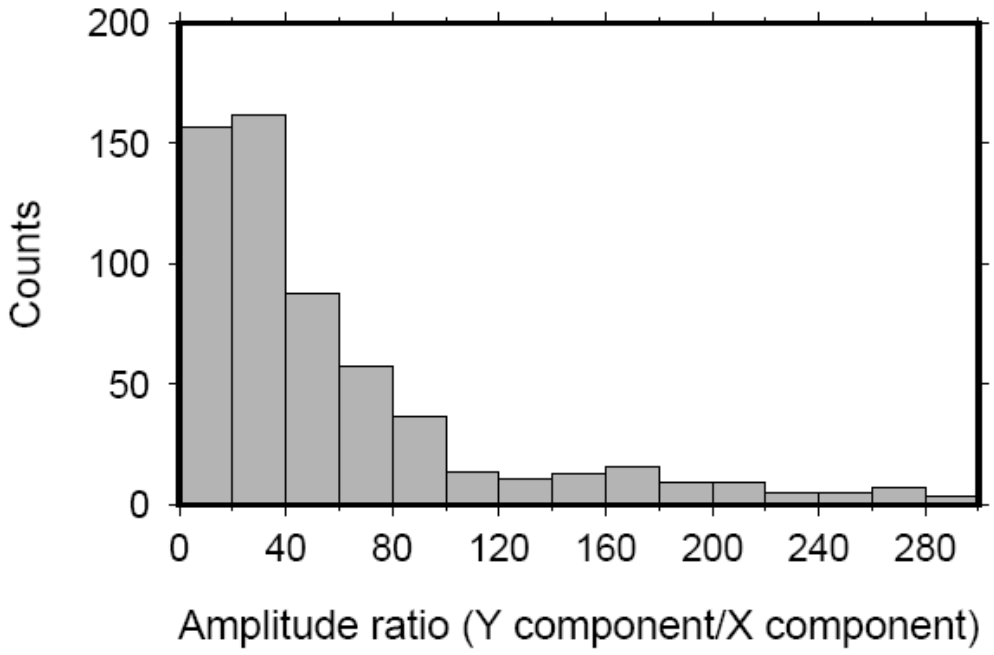

Figure 3.11. Histogram of ratios of Love wave waveform amplitudes in Y components to-those in X components at the period of 40 s. The amplitude of Love wave in the Y component is 10-20 times larger than that in the X component.

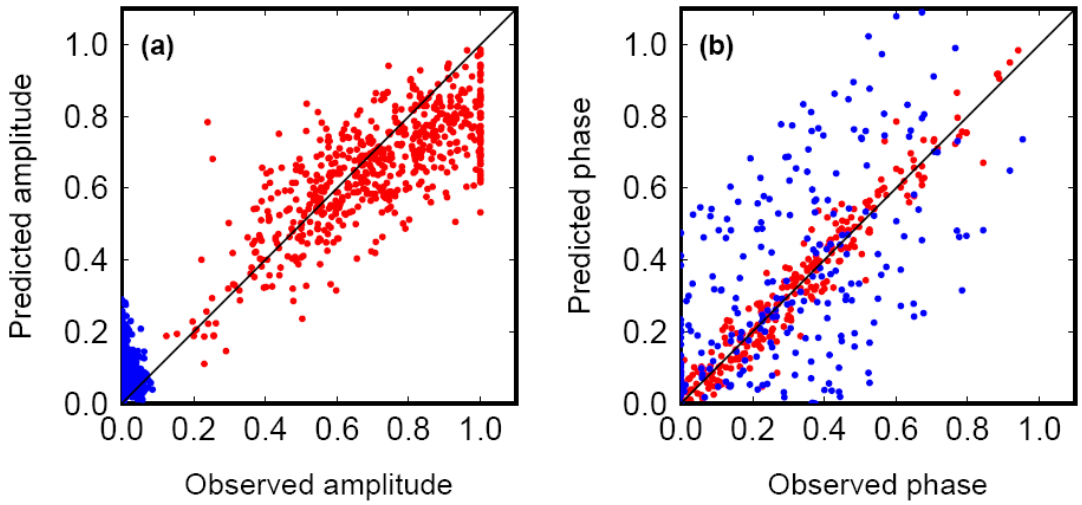

Figure 3.12. Comparison of predicted and observed Love wave amplitudes and phases in X and Y components at the period of 40 s. The red dots are for Y component and the blue dots are for X component.

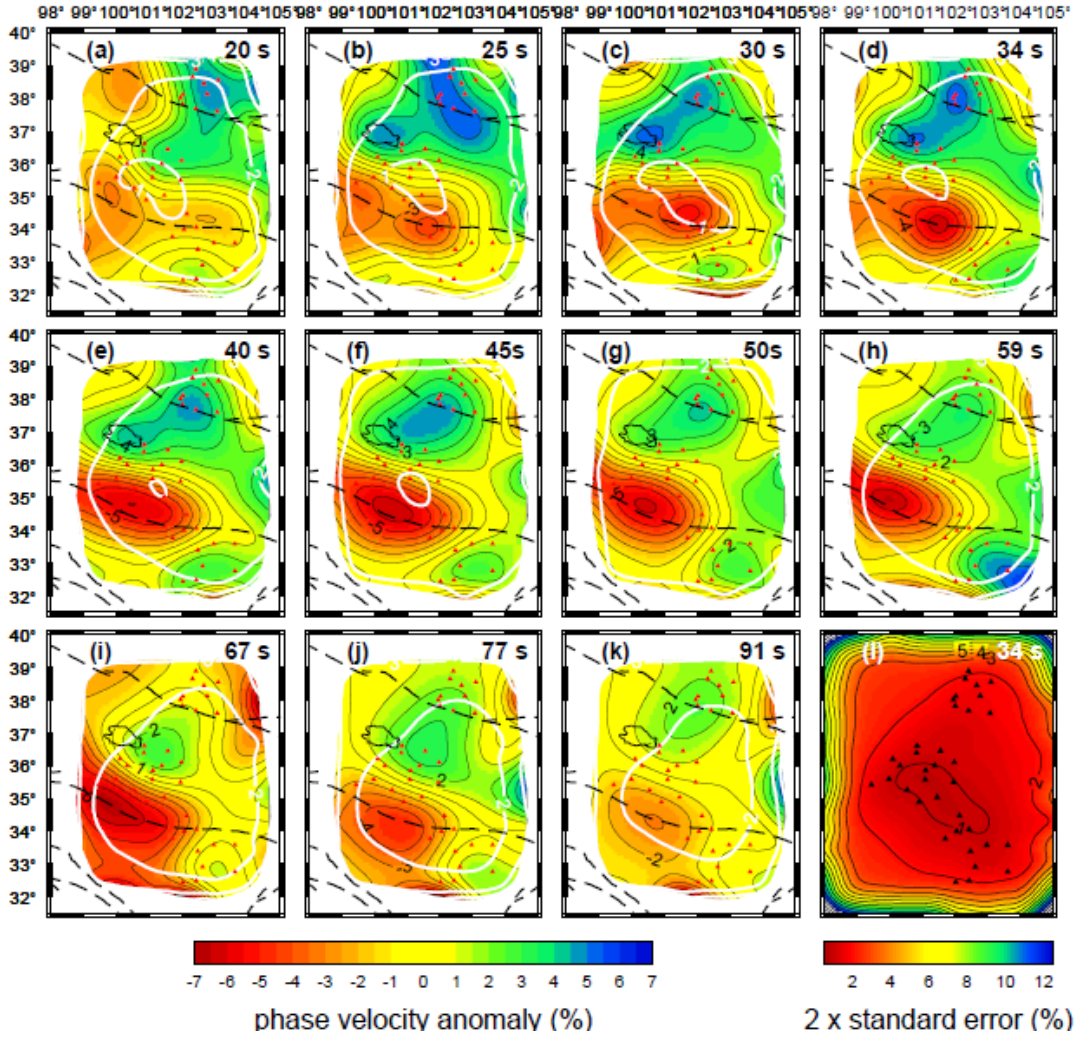

Figure 3.13. Maps of Love wave phase velocity perturbations using amplitude in X and Y components, and their standard errors. (a)-(k) Lateral variations of Love wave phase velocities at 11 periods between 20 and 91 s. The perturbations are calculated with respect to the average values (red solid line) in Figure 3.16a. The white lines are the contour of 2σ of phase velocity perturbation at the corresponding periods. (l) Distribution of 2σ of Love wave phase velocity perturbation at 34 s.

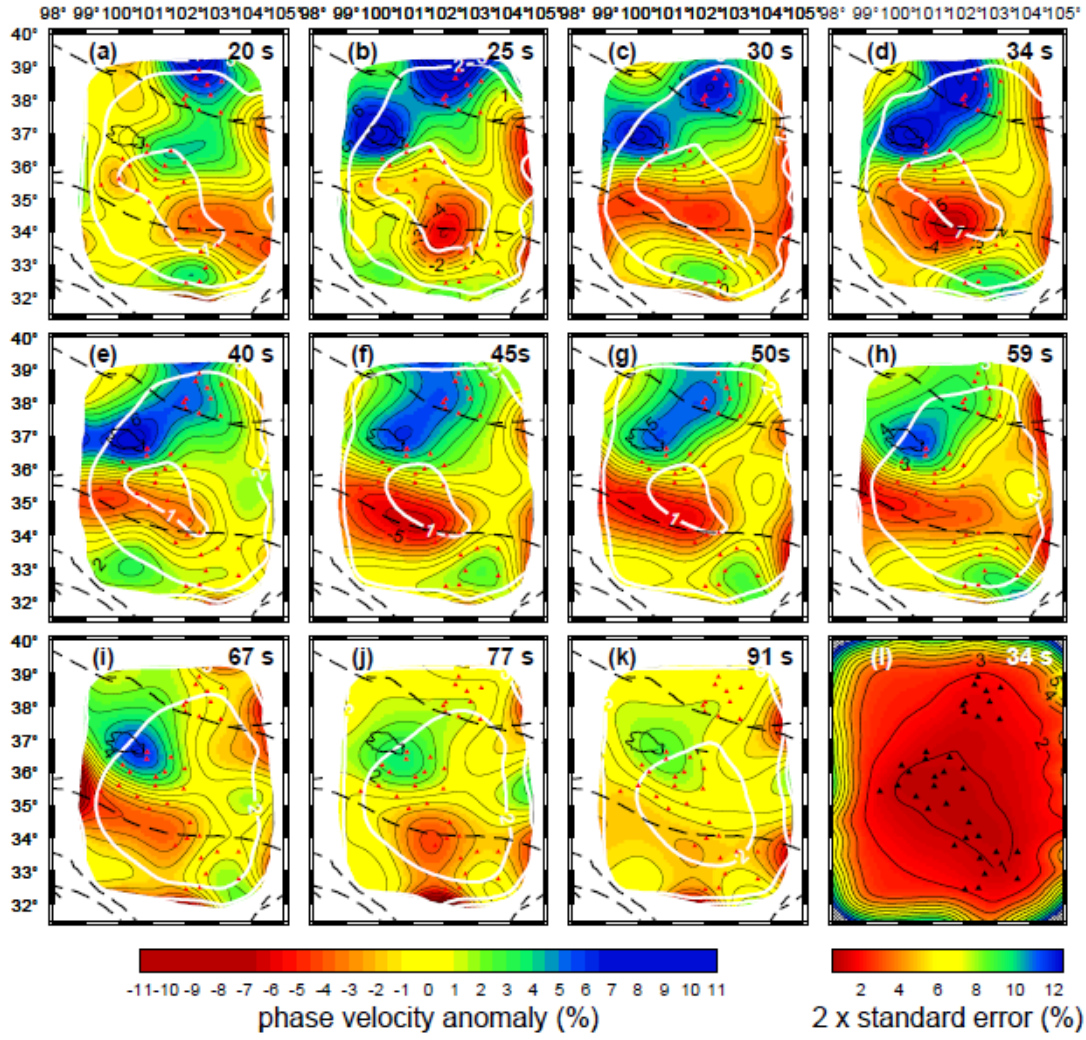

Figure 3.14. Same as Figure 3.13, but using amplitude only in Y components.

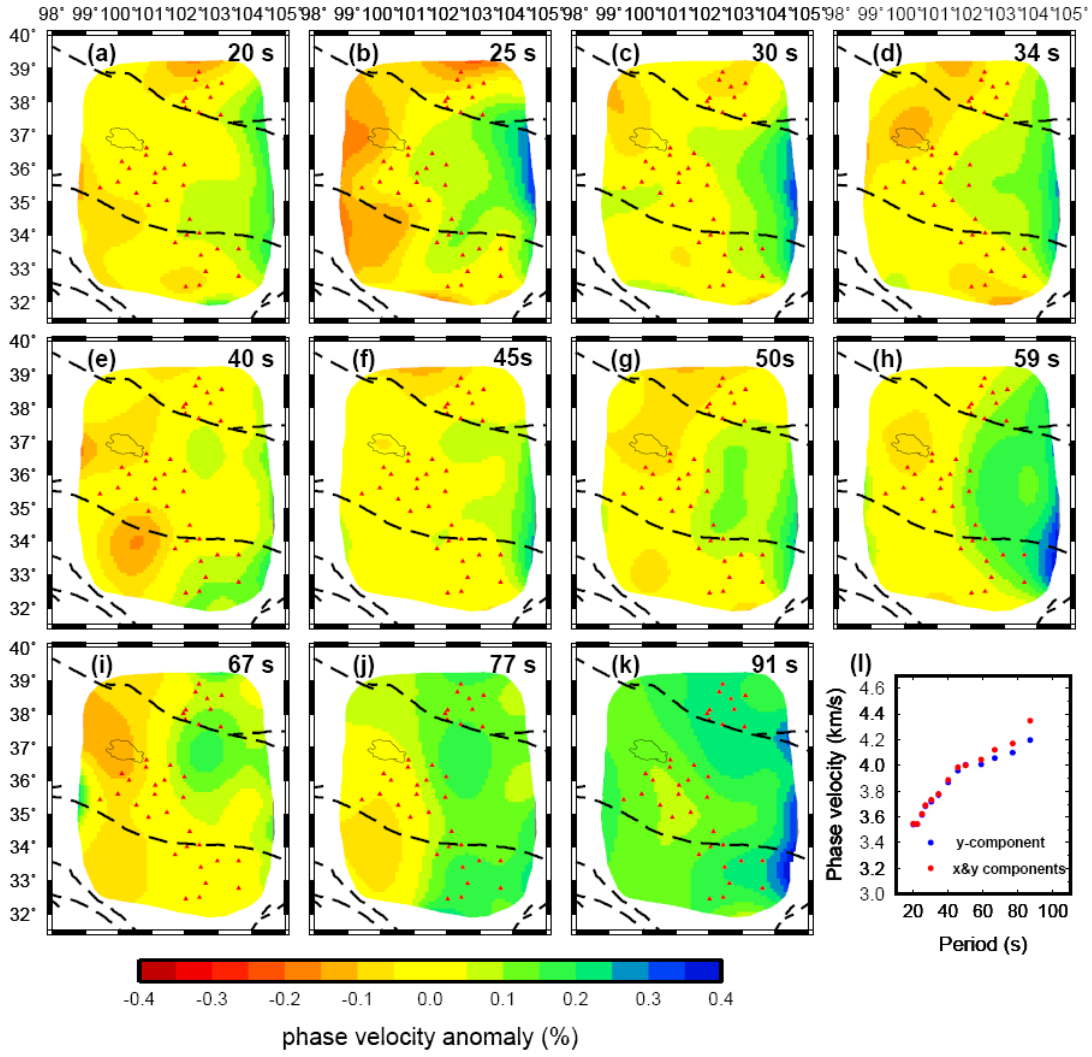

Figure 3.15. Maps of Love wave phase velocity differences using amplitude in both X and Y components, and only in Y component. (a)-(k) Lateral variations of Love wave phase velocity differences at 11 periods between 20 and 91 s. (l) The difference of 1-D average Love wave phase velocity using amplitude in both X and Y components, and only in Y component.

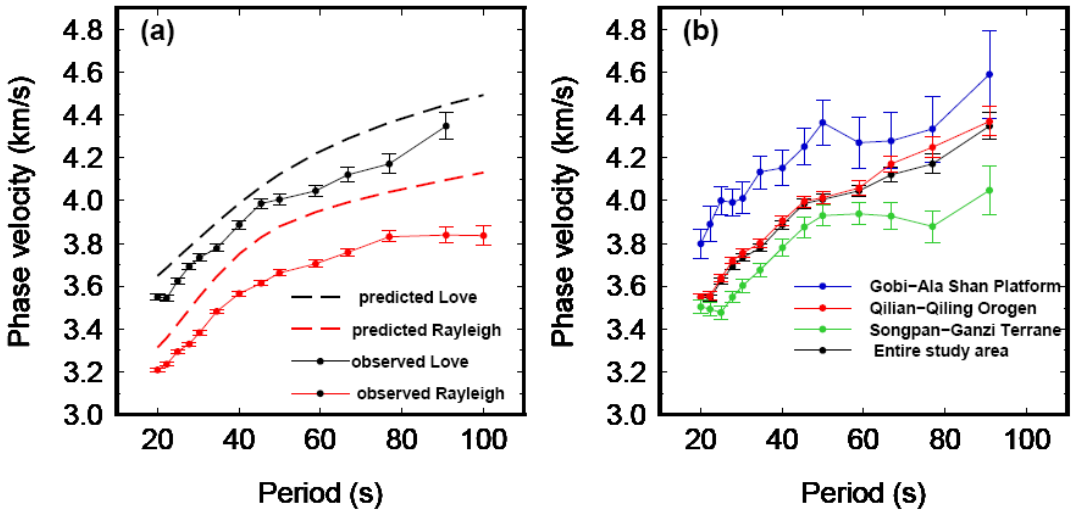

Figure 3.16. (a) Average Rayleigh wave and Love wave phase velocities in the northeastern Tibet. The dashed red line and black line represent the predicted Rayleigh wave and Love wave phase velocity from AK135 model. (b) 1-D average Love wave phase velocity for the three sub-regions (the Gobi-Ala Shan Platform in red, the Qilian-Qinling Orogen in blue, and the Songpan-Ganzi Terrane in green) of the study area.

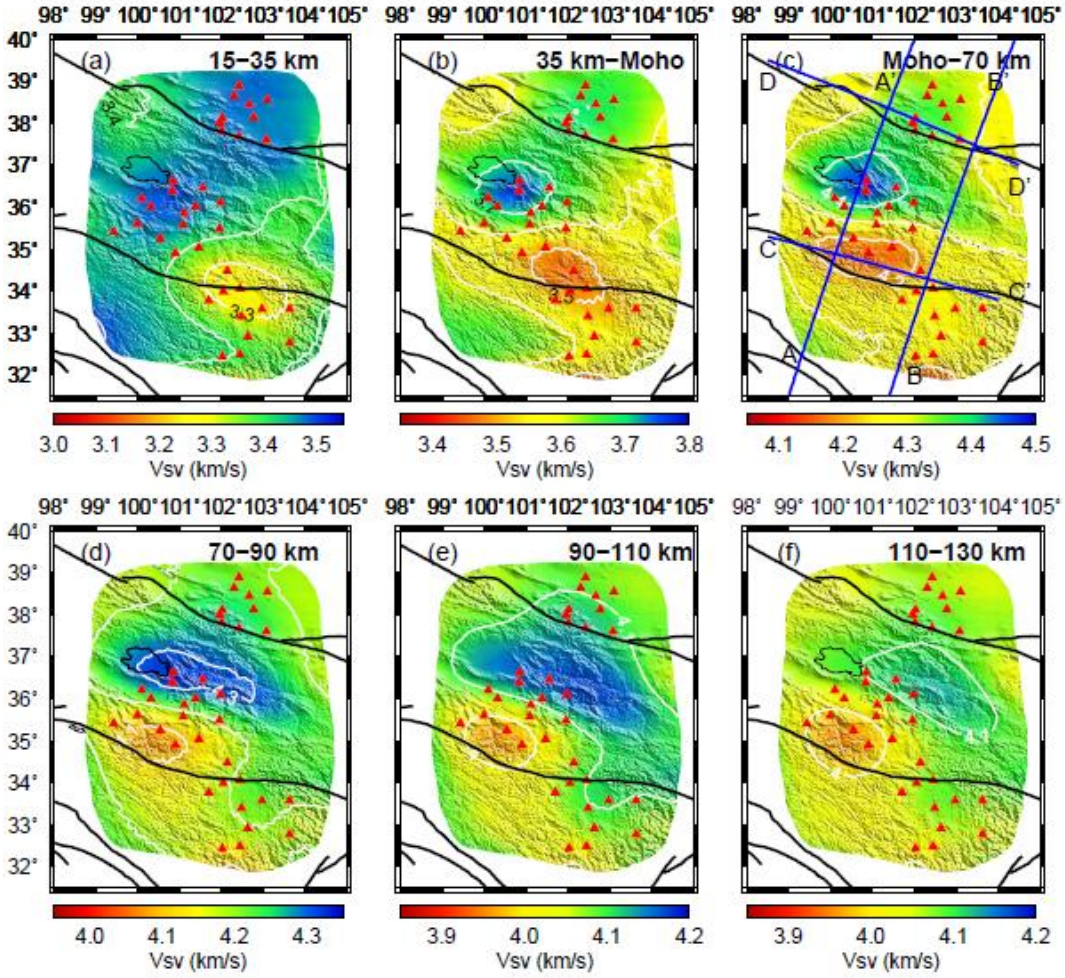

Figure 3.17. Absolute V_{SV} maps at the depths of 15-130 km. Blue lines in Figure 3.17c indicate the location of the cross-sections shown in Figure 3.23~3.25.

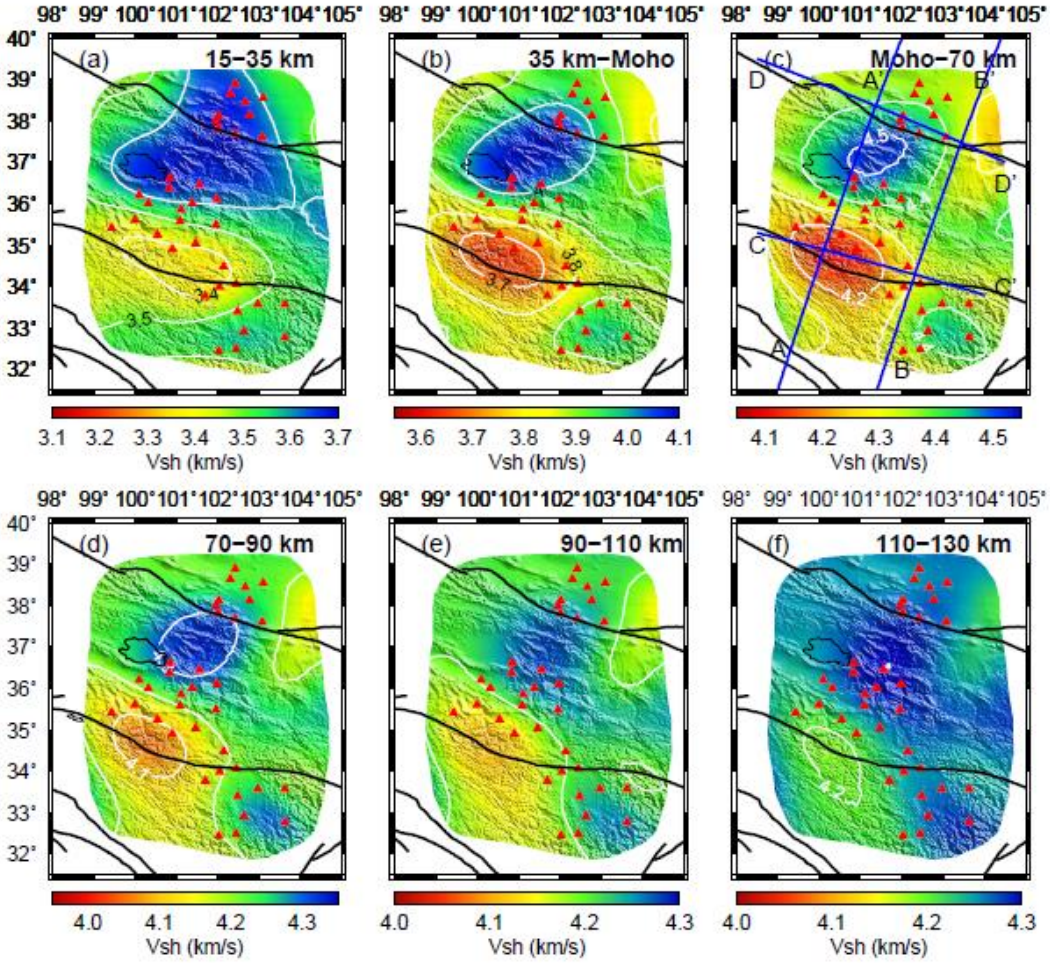

Figure 3.18. Same as Figure 3.17, but for V_{SH} map.

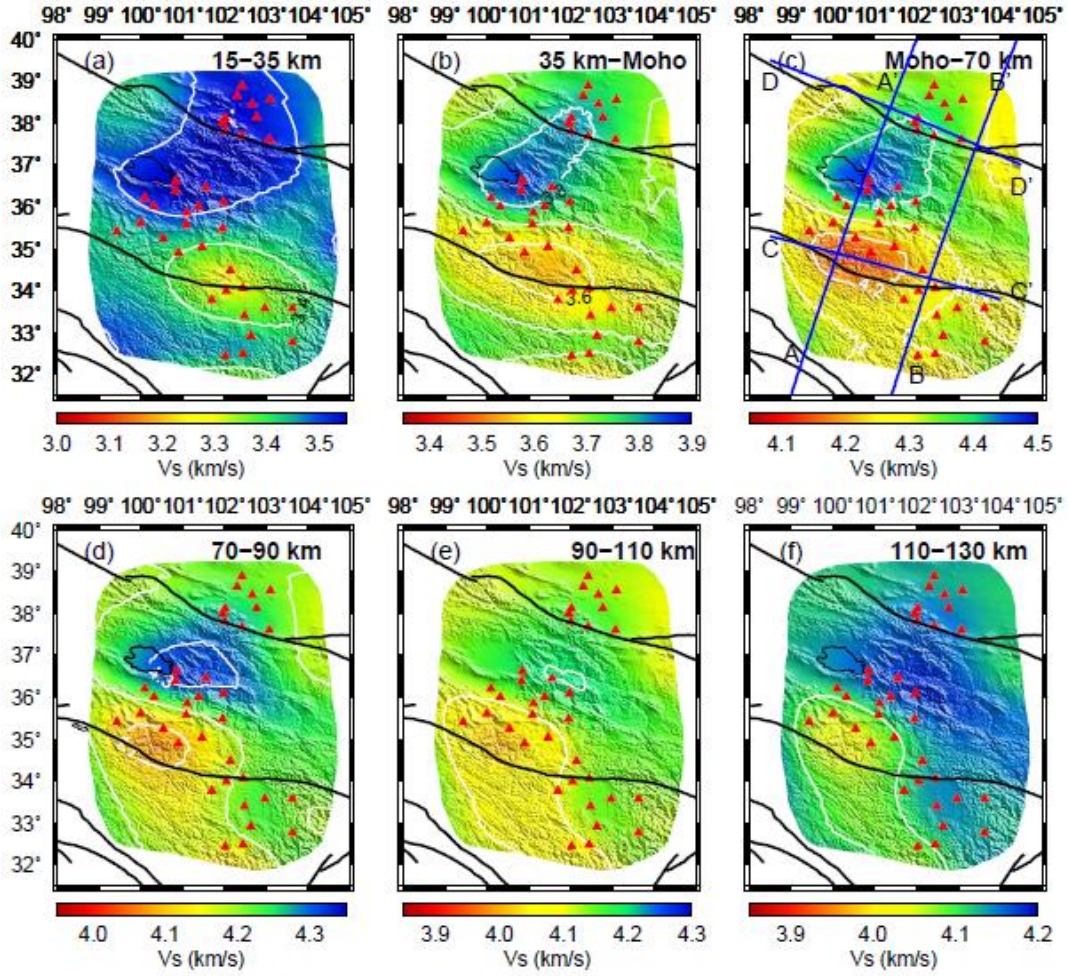

Figure 3.19. Same as Figure 3.17, but for isotropy shear wave velocity (V_S) map. Vs is calculated via a Voigt average, $V_S = \sqrt{(2V_{SV}^2 + V_{SH}^2)/3}$ [*Babuška and Cara*, 1991].

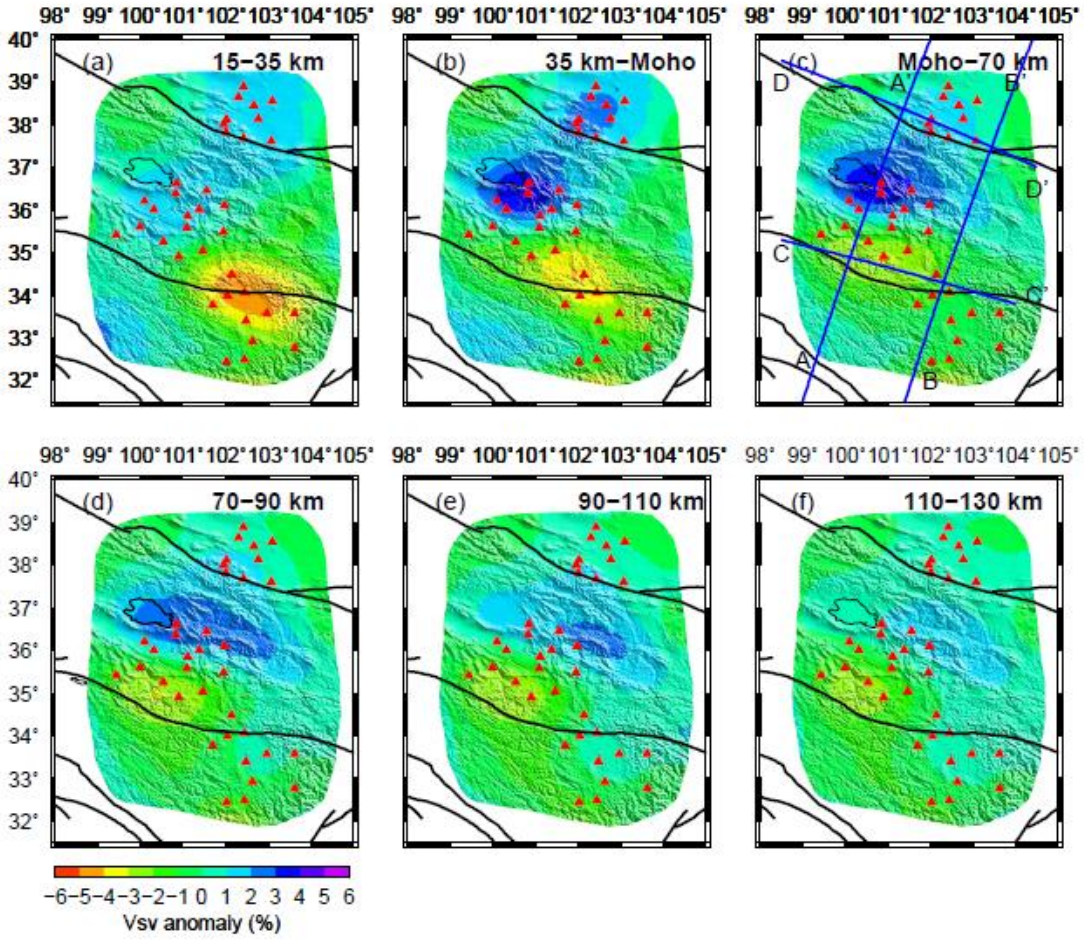

Figure 3.20. V_{SV} anomaly maps at the depths of 15-130 km. The perturbations are calculated with respect to the average values at all the grid nodes.

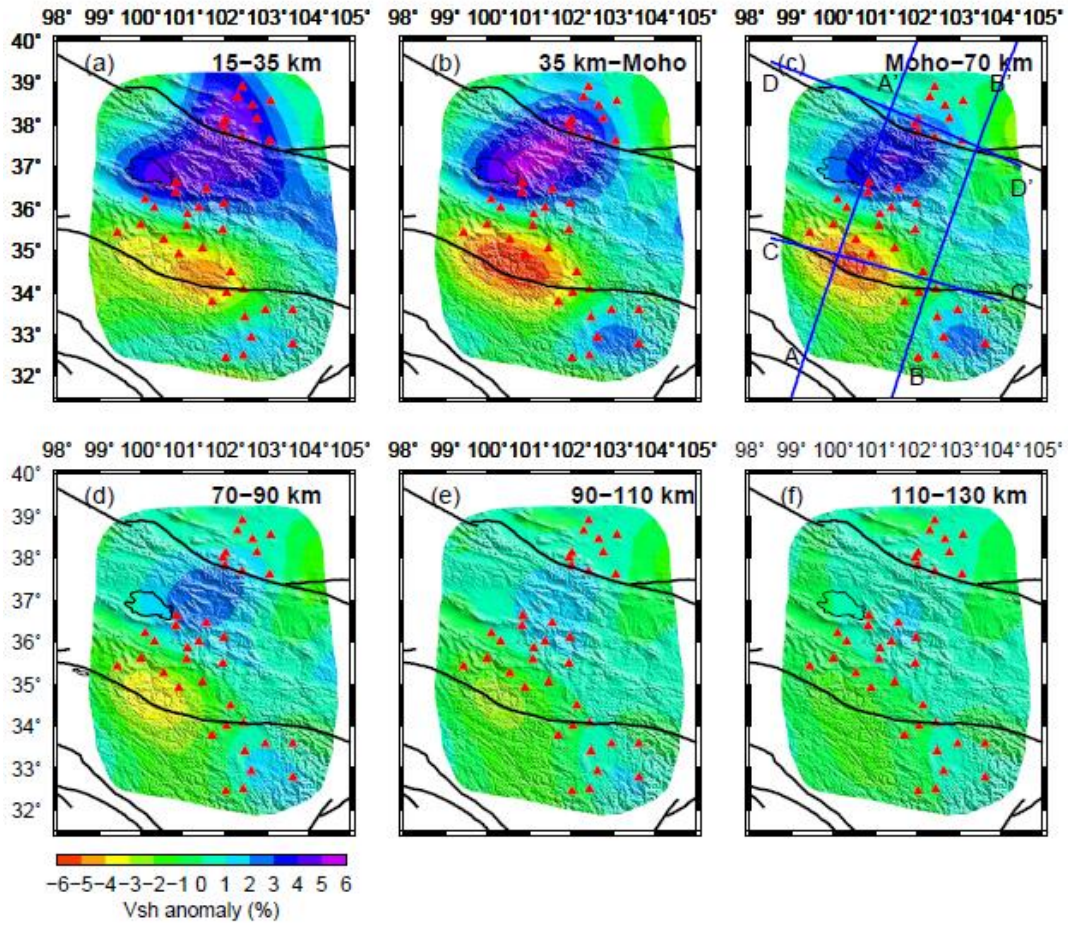

Figure 3.21. Same as Figure 3.20, but for V_{SH} anomaly maps.

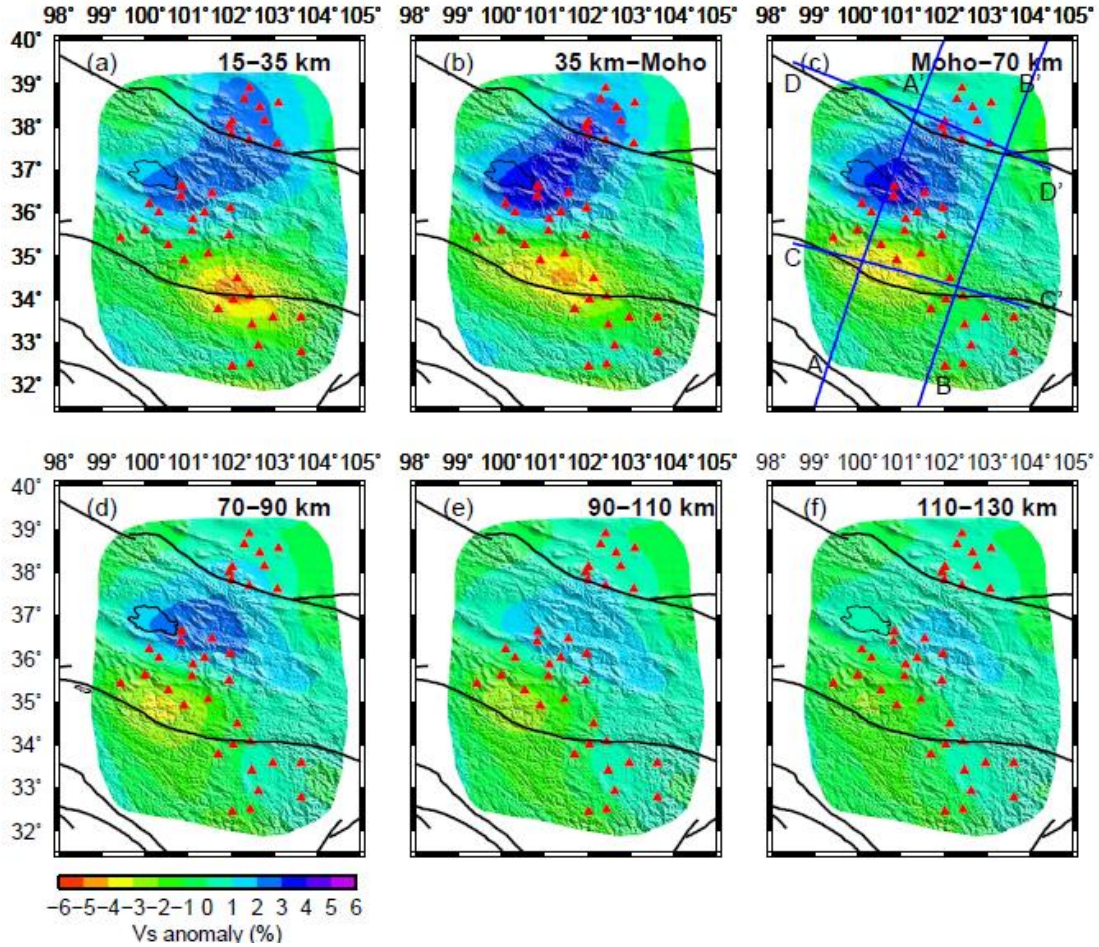

Figure 3.22. Same as Figure 3.20, but for isotropic shear wave velocity (V_S) anomaly maps.

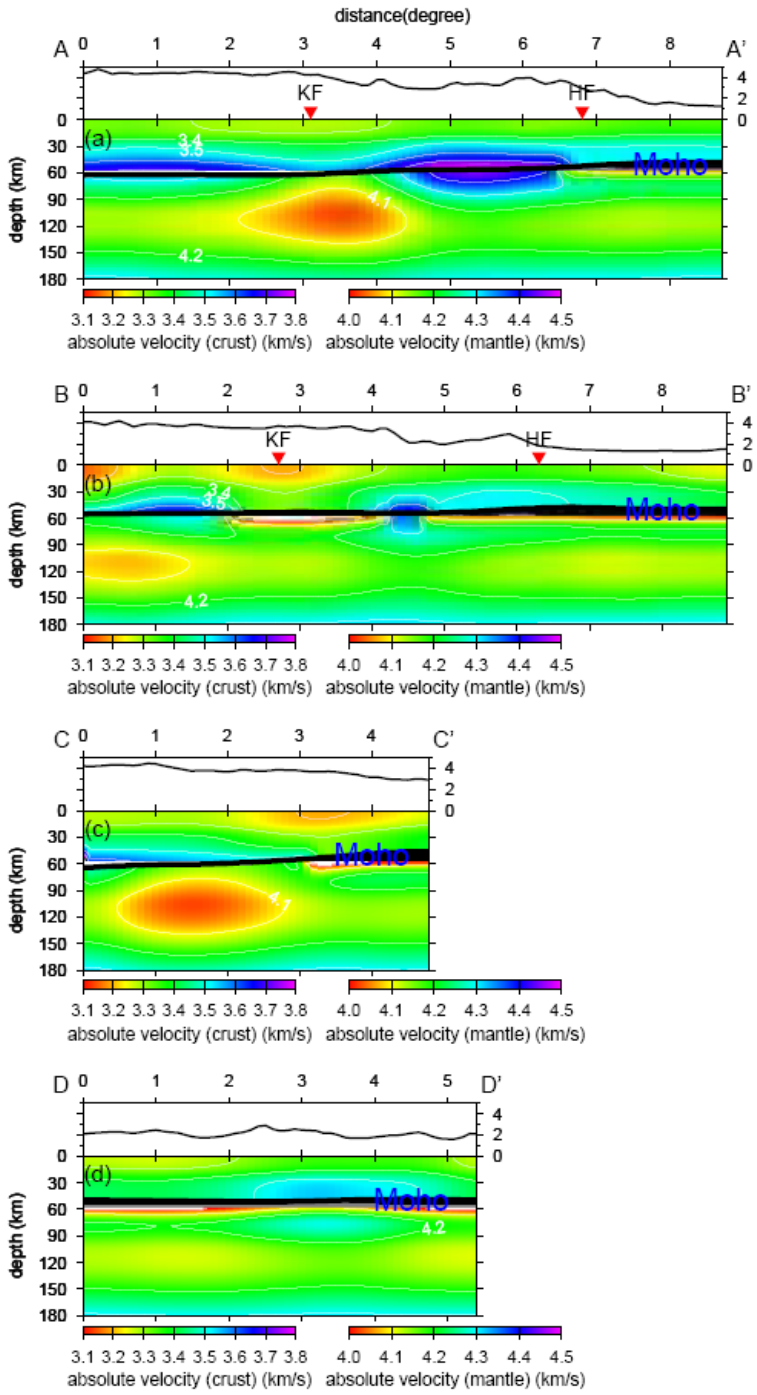

Figure 3.23. Cross-section of absolute V_S from V_{SH} and V_{SV}. Topography is depicted above each profile (black line) with a unit of km. The red triangles mark the location of major faults along each profile. KF, Kunlun fault; HF, Haiyuan fault. The locations of four cross-sections are shown in the Figure 3.19c.

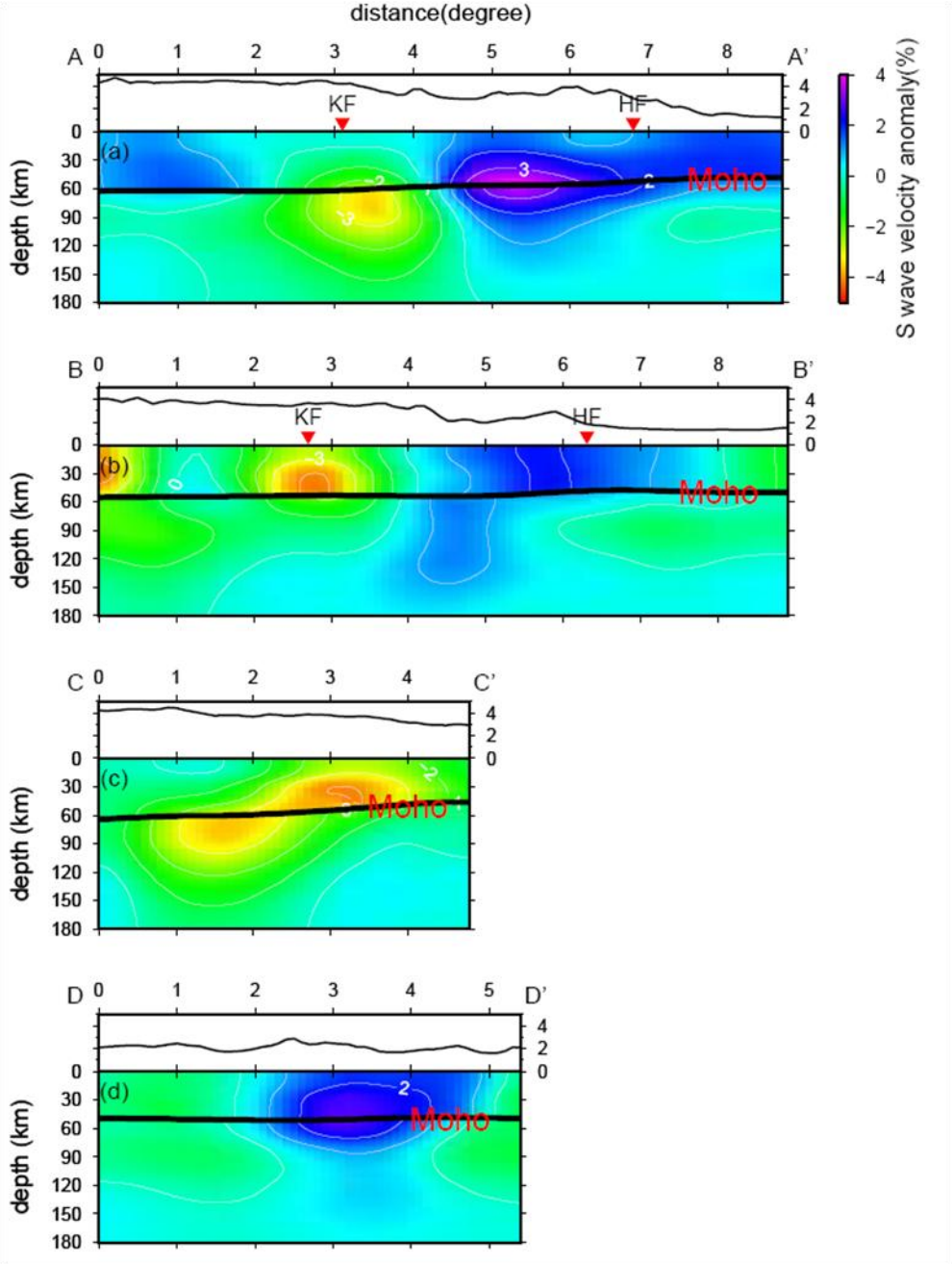

Figure 3.24. Cross-section of Vs perturbations. The perturbation is calculated with respect to the average values at the different layers and at all the grid nodes. Topography is depicted above each profile (black line) with a unit of km.

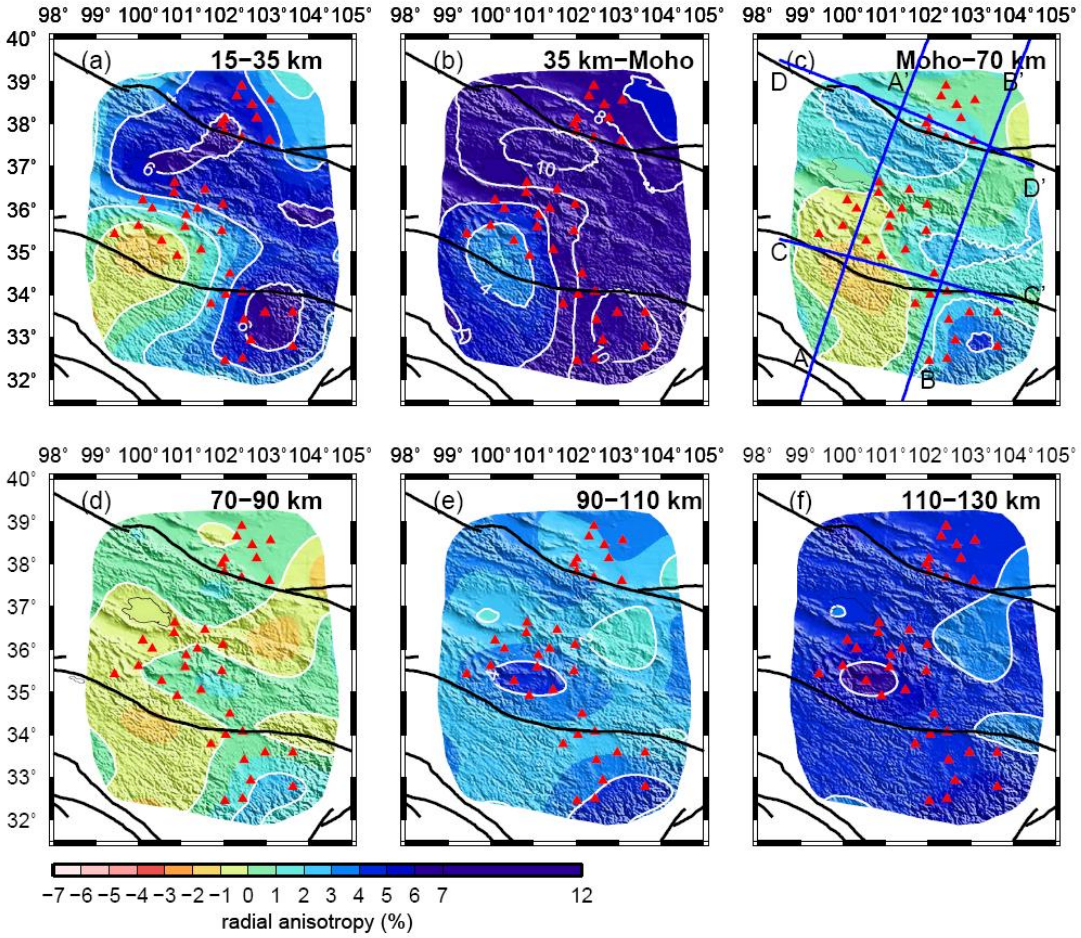

Figure 3.25. Radial anisotropy maps at the depths of 15-130 km. The radial anisotropy is defined as the percentage difference between V_{SH} and V_{SV} in the medium: $\gamma = (V_{SH}-V_{SV})/V_S$. *Vs* is the isotropic or effective shear wave velocity and is computed from V_{SH} and V_{SV} via a Voigt average, $V_S = \sqrt{(2V_{SV}^2 + V_{SH}^2)/3}$ [*Babuška and Cara*, 1991].

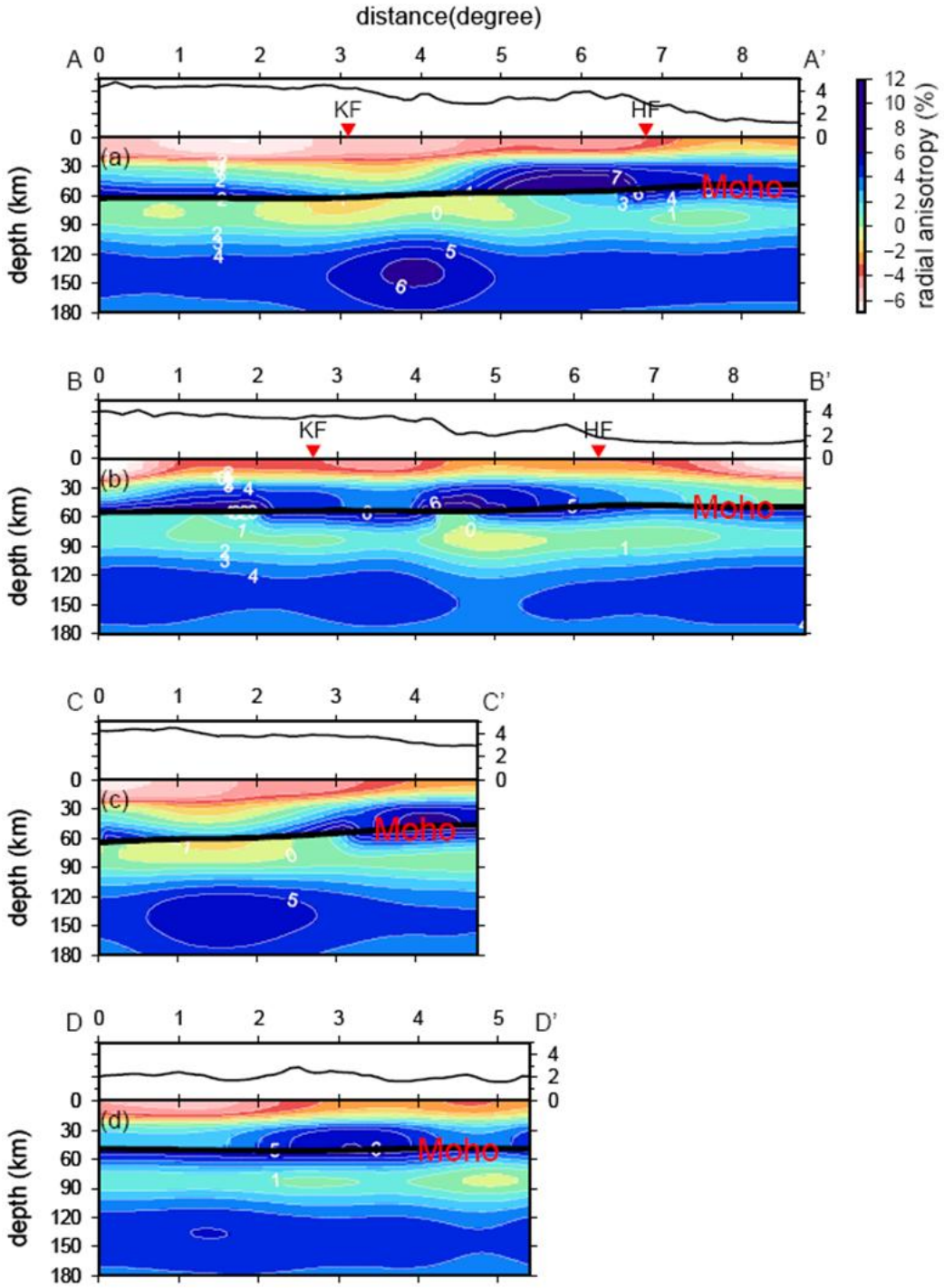

Figure 3.26. Cross-section of radial anisotropy from V_{SH} and V_{SV}. Topography is depicted above each profile (black line) with a unit of km.

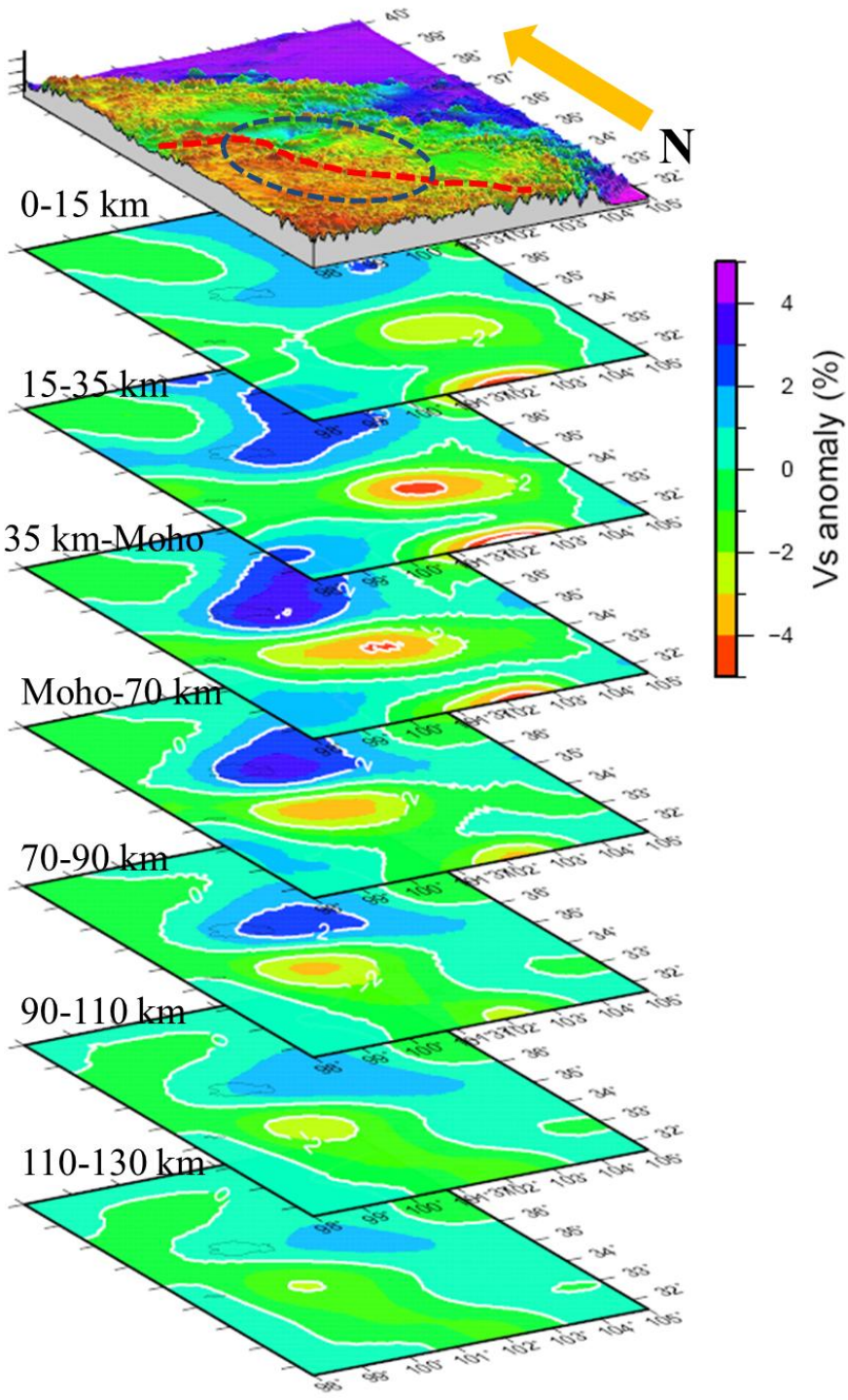

Figure 3.27. 3-D view of the isotropic shear wave velocity (Vs) perturbation model with topography map. The red dashed line represents the Kunlun fault and the blue dashed line indicates the location of the Kunlun restraining bend.

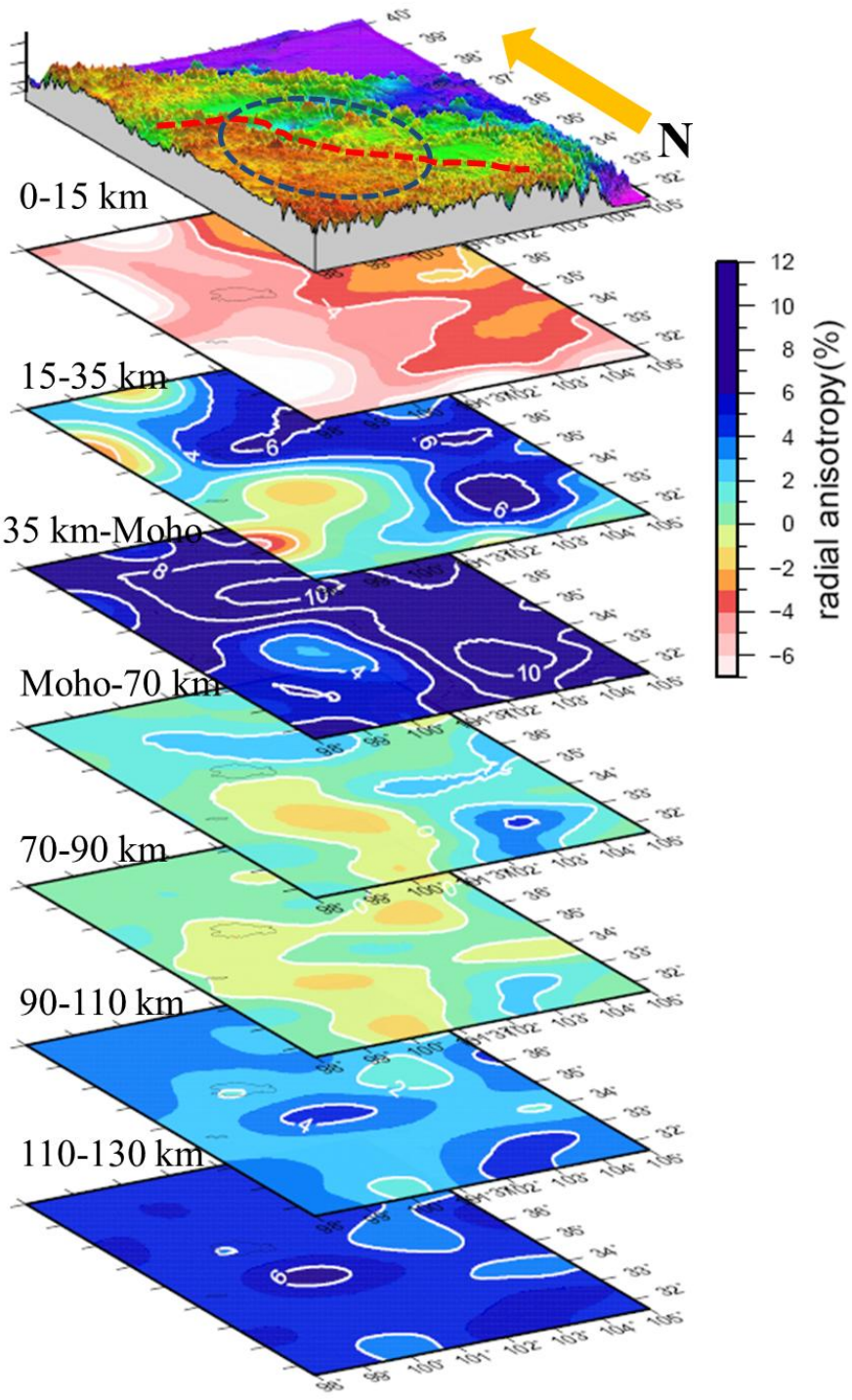

Figure 3.28. 3-D view of the radial anisotropy model. The red dashed line represents the Kunlun fault and the blue dashed line indicates the location of the Kunlun restraining bend.

Chapter 4. Conclusions

4.1. Conclusions

To distinguish different geological models responsible for the growth of the northeastern Tibetan Plateau with interactions of several mountain ranges (the East Kunlun, West Qiling, and Qilian orogenic belts) and two major strike-slip faults (the Kunlun fault and Haiyuan fault), I have constructed 3-D shear wave velocity and radial anisotropy models from 2-D fundamental model Rayleigh wave velocities at 14 periods from 20 to 100 s and Love wave velocities at 13 periods from 20 to 91 s. Both 3-D shear wave velocity (Vs) and radial anisotropy models reflect strong heterogeneity in the NE Tibetan Plateau.

In the first study, a 3-D SV velocity model of the lower crust and upper mantle in the NE Tibetan plateau was constructed using the two-plane-wave (TPW) methods [*Forsyth et al*., 1998; *Forsyth and Li*, 2005]. An isolated slow anomaly centered at ~120 km depth is imaged beneath a restraining bend of the Kunlun strike-slip fault. Additionally, the lithosphere-asthenosphere boundary (LAB) is inferred to be anomalously shallow (80-100 km) beneath the restraining bend from the shear wave velocity model. The correlation between this striking slow anomaly and shallow LAB beneath the restraining bend can be explained by a localized lithosphere dripping. This pronounced slow anomaly is probably caused by anomalously-high temperature and associated partial melting resulted from localized asthenosphere upwelling after the delamination of a thick lithosphere root beneath the restraining bend. This model would help to explain the active deformation of East Kunlun and West Qiling regions.

In the second study, I extended the two-plane-wave (TPW) inversion method for Love waves. The TPW inversion method has been extensively utilized in various studies [e.g., *Forsyth et al.*, 1998; *Li*, 2011; *Zhang et al.*, 2011]. Unfortunately, the TPW method is currently only suitable for Rayleigh waves. This limits the studies of radial anisotropy from discrepancy between Rayleigh and Love wave tomography. Extending the TPW inversion method for Love wave phase velocities is therefore greatly needed to fill the gap in seismic data processing so that high-resolution 3-D radial anisotropy models can be developed in many places where regional seismic networks are available. 1-D and 2-D Love wave phase velocities were obtained and then inverted into 1-D and 3-D V_{SH} models in the NE Tibetan plateau. Then a 3-D radial anisotropy model was constructed from V_{SH} and previously obtained Vsv. A correlation between negative anisotropy ($V_{SV}>V_{SH}$) and high mountain belts in the shallow crust reflects horizontal shortening and vertical extension in the orogenic regions. The positive anisotropy with amplitude of up to 10% ($V_{SH}>V_{SV}$) in the lower crust is probably resulted from the horizontal alignment of mica crystals due to the past deformation at the formation of lower crust. The mantle lithosphere above 90 km is largely isotropic while weak positive anisotropy appears beneath 90 km, which probably marks the lithosphere-asthenosphere boundary. Asthenosphere flow is the main source for the positive anisotropy at the depth of 90-130 km. Additionally, a low velocity anomaly and negative radial anisotropy ($V_{SV}>V_{SH}$) are consistently observed in the lithosphere beneath the restraining bend of the Kunlun fault. These geophysical observations suggest the existence of coherent lithosphere deformation in this area that could have resulted in a thick lithosphere root. These findings reflect complex

deformation pattern in the NE Tibetan plateau which is controlled by the interaction among localized compression, strike-slip faulting, asthenosphere flow and horizontal shortening in the crust.

4.2. References

Forsyth, D. W., and A. Li (2005), Array-analysis of two-dimensional variations in surface wave phase velocity and azimuthal anisotropy in the presence of multipathing interference, in Seismic Earth: Array Analysis of Broadband Seismograms, *Geophys Monogr. Ser.*, vol. 187, edited by A. Levander and G. Nolet, pp. 81–97, AGU,

Forsyth, D.W., Webb, S., Dorman, L., and Shen, Y. (1998), Phase velocities of Rayleigh waves in the MELT experiment on the East Pacific Rise. *Science* 280, 1235–1238.

Li, A. (2011), Shear wave model of southern Africa from regional Rayleigh wave tomography with 2-D sensitivity kernels. *Geophys. J. Int.*, 185, 832-844.

Zhang, Q., E. Sandvol, J. Ni, Y. Yang, and Y. J. Chen (2011), Rayleigh wave tomography of the northeastern margin of the Tibetan Plateau , *Earth Planet. Sci. Lett.*, 304, 103–112, doi:10.1016/j.epsl.2011.01.021.